Dark Cosmology Centre

Observational probes of dark matter halos

Ole Høst

Supervisor: Steen H. Hansen

Dark Cosmology Centre, Niels Bohr Institute

Faculty of Science, University of Copenhagen

Observational probes of dark matter halos

Ole Høst

August 26, 2009

Dark Cosmology Centre
Niels Bohr Institute
The Graduate School of Science
Faculty of Science
University of Copenhagen
Denmark

ABSTRACT

Dark matter constitutes six times more of the mass in the Universe than ordinary baryonic matter. The halos formed by dark matter are fundamental to the formation of structure, yet the properties of these halos are not well understood theoretically or observationally.

In the first part of this thesis, I review the evidence for the existence of dark matter and its role in cosmology and astrophysics, and I discuss the particle nature of dark matter and how that nature can be identified. Then, I summarize the predicted properties of collisionless dark matter halos from fundamental theory and from numerical simulations of the formation of structure. In particular, I focus on the possibility of an anisotropic velocity dispersion tensor where the typical velocity in one direction can be different from that in another direction. This anisotropy demonstrates the fundamental difference between collisionless dark matter systems and collisional gases.

In the second part of the thesis, I investigate how the properties of halos can be constrained observationally, and what these constraints imply about dark matter. First, I analyze how accurately the velocity anisotropy parameter can be measured in a dark matter detector which is sensitive to the direction of the measured dark matter particles. The anisotropy parameter turns out to be measurable, but I find that a very large number of events are necessary to reject isotropy at high statistical significance. Second, using x-ray observations of a sample of galaxy clusters, I carry out a first measurement of the radially-varying velocity anisotropy profile of dark matter. The measured profile is found to be non-zero and radially increasing, which is in good agreement with the predictions of numerical simulations. The measurement implies that dark matter is in fact effectively collisionless in clusters and it sets an upper limit on the dark matter self-scattering cross section. Finally, I again use a sample of clusters observed in x-ray to constrain the mass distribution of dark matter in the halos of the clusters. I compare the measured mass profiles with a number of parametrized mass models in a detailed statistical analysis. I find moderate evidence that the observed mass profiles are not strictly universal but require a shape parameter to be fitted to each halo.

Mørkt stof udgør seks gange så meget af massen i universet som almindeligt, baryoniskt stof. Haloer dannet af mørkt stof spiller en grundlæggende rolle i dannelsen af struktur, men alligevel er den teoretiske og observationelle forståelse af haloernes egenskaber mangelfuld.

I denne afhandlings første del gennemgår jeg beviserne for eksistensen af mørkt stof, og jeg diskuterer mørkt stofs egenskaber som partikel, samt hvorledes denne partikel kan identifceres. Derefter beskriver jeg egenskaberne ved en kollisionsløs halo af mørkt stof, som forudsagt teoretisk og udfra numeriske simuleringer. Jeg fokuserer på hastighedsfordelingens dispersionstensor, som kan være ellipsoidisk, således at middelhastigheden i én retning er forskellig fra middelhastigheden i en anden retning. Denne anisotropi er et eksempel på den grundlæggendel forskel mellem kollisionsløst mørkt stof og vekselvirkende gas.

I afhandlingens anden del undersøger jeg, hvorledes haloers egenskaber kan bestemmes gennem ob-

servationer, samt hvad disse egenskaber betyder for mørkt stof. Først undersøger jeg, hvor nøjagtigt anisotropiparameteren kan måles i en partikeldetektor, som kan bestemme retningen af de målte mørkt stof partikler. Det viser sig, at der kræves et meget stort antal vekselvirkninger af mørkt stof i detektoren for at afvise med statistisk signifikans, at hastighedsfordelingen er isotrop. Derefter anvender jeg observationer af galaksehobe i røntgenspektret til, for første gang nogensinde, at måle anisotropiparameteren og dennes radiale variation i hobenes haloer. Den målte profil er forskellig fra nul og vokser med radius i god overensstemmelse med forudsigelser baseret på numeriske simuleringer. Målingen betyder, at mørkt stof i galaksehobe må opføre sig som kollisionsløse partikler, og at der kan sættes en øvre grænse for tværsnittet af det mørke stofs egenvekselvirkning. Til sidst bruger jeg igen røntgenobservationer af galaksehobe til at undersøge massefordelingen i hobene. Jeg sammenligner de målte fordelinger med forskellige parametriserede masseprofiler på grundlag af en detaljeret statistisk analyse. Jeg påviser, at der er moderat evidens for, at masseprofilen ikke er strengt universel, men derimod kræver, at en formbestemmende parameter tilpasses hver hobs halo.

CONTENTS

1. INTRODUCTION & OBJECTIVES

Dark matter is one of the main unsolved mysteries in modern physics and cosmology. The notion that the majority of matter in the Universe is of a so far unknown nature humbles our perception of the physical world. The investigation of dark matter, its particle nature, and its role in the Universe encompasses efforts from the fields of cosmology, astrophysics, high energy physics, experimental nuclear physics, and so on. So far the nature of dark matter is unknown, but a large and diverse experimental effort gives hope that this situation may be about to change. Identifying dark matter will be a major breakthrough in high energy physics, as a signpost for physics beyond the standard model, and in cosmology, as the dominant form of matter.

Historically, dark matter was first suggested as unobserved missing matter in galaxy clusters. Today we know that dark matter halos play a crucial role in the formation of structure in the Universe. The purpose of this thesis is to constrain the properties of dark matter halos observationally. This includes the distribution of mass in the halos and the dynamics of the dark matter particles. Out of several possible observational probes, I focus on two: x-rays from the intracluster medium of galaxy clusters, which traces the distribution of mass in the dark matter halo, and 'dark matter telescopes' in the form of direction-sensitive dark matter detectors, that may be able to detect Galactic dark matter particles.

The present thesis takes the form of a synopsis, which means that the main body of the thesis presents a review of the dark matter field and a summary of the research in relation to that context. By necessity, this review is concise and, in some cases, quite selective in the topics covered, and the bibliography is perhaps exemplifying rather than exhaustive. In section 2, the modern picture of cosmology is summarized, including a brief discussion of structure formation with dark matter, and the evidence for dark matter in astrophysics is introduced. Section 3 covers the particle nature of dark matter, how dark matter can appear in particle physics theories beyond the standard model, and the various possibilities for identifying dark matter. In section 4, dark matter halos are discussed, with an emphasis on how they can be studied in observations. Finally, section 5 is a summary and comment on the papers.

The actual accounts of the research, i.e. the scientific papers on which the thesis is based, are included in manuscript as appendices. The papers are

- Paper I: Host & Hansen (2007), published in Journal of Cosmology and Astro-particle Physics, Issue 06, pp. 016 (2007).

- Paper II: Host et al. (2009), published in The Astrophysical Journal Volume 690, Issue 1, pp. 358-366 (2009).

- Paper III: Host & Hansen (2009), submitted to The Astrophysical Journal, preprint available from arXiv:0907.1097.

The appended manuscripts are identical to the published or submitted versions, except that the references have been merged into a single bibliography for the whole thesis and are updated where necessary.

Acknowledgments

2. COSMOLOGY

The present cosmological paradigm is built on the theory of general relativity, the assumptions of homogeneity and isotropy of the Universe, and the idea that the Universe originated in a Big Bang. The observational foundations of this model are the Cosmic Microwave Background (CMB) and the anisotropies in that, the agreement between predictions and measurements of the light element abundances, galaxy redshift surveys that map structure in the Universe, and the evidence for accelerated expansion, as first determined by the dimming of distant supernovae. Together these pieces form a picture of an initially smooth, expanding Universe in which small deviations from smoothness become gravitationally unstable and collapse to form galaxies and galaxy clusters. In this section, I summarize the present picture of cosmology. The topics are essentially textbook material (Kolb & Turner, 1990; Dodelson, 2003; Ryden, 2003).

2.1 The evolution of the Universe

Modern physics is the study of matter and how matter interacts. There are four types of interactions, or forces, namely the strong and weak nuclear forces, the electromagnetic force, and gravity. The first two are short-range in nature and they can only be observed on the scales of nuclei and smaller. Electromagnetism also affects matter on the nuclear scales, and it is the dominant force on meso-scopic scales. In principle it is a long-range force, but since equal charges repel each other so that large accumulations of charge are not found, electromagnetism does not play a direct role on cosmological scales. The remaining force, gravity, is far weaker and therefore unobservable on nuclear scales, but since there is no negative gravitational charge, gravity is the governing force on cosmological scales.

Einstein's theory of general relativity describes gravity as a curvature of four-dimensional space-time where matter curves space-time and objects in free fall travel along geodesics. The local structure of space-time, and hence of gravity, is encoded in the metric $g_{\mu\nu}$ which is sourced by the energy-momentum tensor $T_{\mu\nu}$, as a generalization of how the Newtonian potential is sourced by the mass density.

On sufficiently large scales the Universe appears spatially homogeneous and isotropic, in the sense that no particular volume of space stands out from any other. Assuming homogeneity and isotropy, the invariant line element $\mathrm{d}s^2 = g_{\mu\nu}\mathrm{d}x^\mu\mathrm{d}x^\nu$ is given by the Friedmann-Lemaître-Robertson-Walker metric,

$$\mathrm{d}s^2 = -\mathrm{d}t^2 + a(t)^2 \left[\frac{\mathrm{d}r^2}{1 - kr^2} + r^2\mathrm{d}\Omega^2 \right]. \quad (2.1)$$

The scale factor $a(t)$ describes the size of the Universe and is conventionally set to $a_0 = 1$ at present, while $k = 1, 0, -1$ corresponds to positive, zero, and negative curvature, respectively. The expansion rate $H = \dot{a}/a$ is dictated by the energy content and is given by the Friedmann equation,

$$H^2 = \frac{8\pi G}{3} \left(\rho - \frac{\rho_c - \rho_0}{a^2} \right), \quad (2.2)$$

where $\rho_0 \approx 10^{-26}\,\mathrm{kg\,m^{-3}}$ is the present mean energy density, and $\rho_c = 3H^2/8\pi G$ is a 'critical density' which is defined by a flat geometry, $k = 0$. If the mean energy density is smaller than the critical density the Universe has negative curvature, and if it is greater the curvature is positive. The energy densities of the various components of the Universe—matter, radiation, etc.—are often given in units of the critical density, $\Omega_i = \rho_i/\rho_c$. The present expansion rate, the Hubble constant, is given as $H_0 = 100h\,\mathrm{km\,s^{-1}\,Mpc^{-1}}$. The Hubble space telescope used distant Cepheids to measure $h \approx 0.7$ (Freedman et al., 2001).

The energy densities of the different components evolve according to the pressure, $P = w\rho$. For a constant equation of state w the result is a power-

law dependence

$$\rho \propto a^{-3(1+w)}. \qquad (2.3)$$

Non-relativistic matter, including both baryons and cold dark matter, is essentially pressure-less ($w = 0$) and its energy density simply scales as the inverse of volume, $\rho_m \propto a^{-3}$. Radiation ($w = 1/3$) picks up an extra factor due to the redshifting of its wavelength, i.e. $\rho_r \propto a^{-4}$, and the energy density associated with curvature, the second term in eq. (2.2), behaves as $\rho_k \propto a^{-2}$. Conversely, the dominant contribution to the energy density determines the expansion rate through the Friedmann equation and the Euler equation which yield the acceleration

$$\frac{\ddot{a}}{a} = -\frac{4\pi G}{3}(\rho + 3P). \qquad (2.4)$$

In the early hot Universe, numerous high-energy photons dominate the energy budget, but radiation gives way to a phase of matter domination beginning around the time the CMB is formed. Observations of the dimming of type Ia supernovae, believed to be 'standard candles', show that the expansion of the Universe begins to accelerate (Riess et al., 1998; Perlmutter et al., 1999) at quite low redshift, $z < 1$. Acceleration cannot be caused by ordinary matter but requires a component with negative pressure, $w < -1/3$, as evident from eq. (2.4). The simplest phenomenological possibility to explain this is a cosmological constant Λ, termed dark energy, which has $w = -1$ and which appears as a constant term in the Einstein equations. This has led the ΛCDM cosmological model, consisting of dark energy and cold dark matter, to become the standard cosmological model, despite the fact that there is no understanding of what may constitute the dark energy.

Within the ΛCDM model, the measurements of the CMB anisotropies by the WMAP satellite as well as a number of ground-based or balloon-borne telescopes, together with the measured expansion rate h, constrain the total amount of pressure-less matter to be $\Omega_m \approx 0.3$ (Spergel et al., 2007; Komatsu et al., 2009). The amount of curvature is also severely constrained, and the Universe appears to be very close to a flat geometry. The supernovae observations, as well as independent constraints from the gas fraction of galaxy clusters
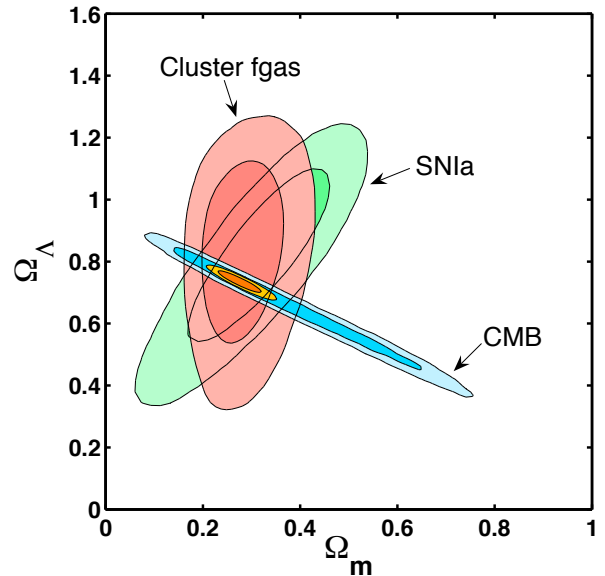
Fig. 2.1: Observational constraints on the energy content of the Universe. The CMB-only contours are based on a uniform prior $0.2 < h < 2$, the HST prior narrows these contours considerably. No priors on h or Ω_b are used for the joint contour. Figure from Allen et al. (2008).

(Allen et al., 2008), require a non-zero Ω_Λ, but a degeneracy in the $\Omega_\Lambda - \Omega_m$ plane means that a fairly wide range in Ω_Λ can be accomodated. This degeneracy is broken by a joint analysis of the supernova data and the CMB data. The missing energy required by the CMB to achieve the critical energy density is provided by the cosmological constant, $\Omega_\Lambda = 1 - \Omega_m \approx 0.7$. Figure 2.1 summarizes the constraints on the contributions from matter and the cosmological constant to the energy budget in the present Universe.

2.2   Growth of perturbations

If the Universe contains only perfectly smooth fluids there cannot be any gravitational clustering. The seeds of the present day galaxies are seen in the CMB temperature field as tiny fluctuations at a level of 10^{-5} relative to the mean temperature. The statistical distribution of these fluctuations can be compared with theoretical model predictions. For

Fig. 2.2: Measured power spectrum of the CMB temperature anisotropies. The additional small scale data points are from the balloon-based Boomerang telescope and the ground telescopes ACBAR and CBI. Figure from Nolta et al. (2009).
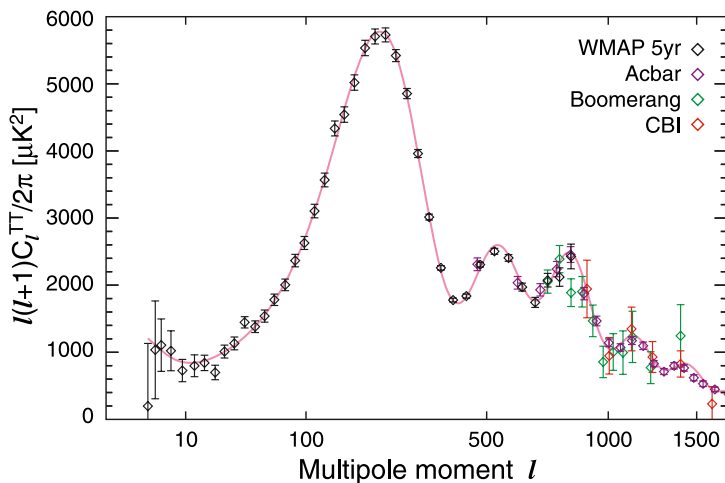
this, the observed temperature field on the sky is expanded in spherical harmonics and the correlation function of this expansion is

$$\left\langle \frac{\delta T}{T}(x) \frac{\delta T}{T}(x') \right\rangle = \sum_{l=1}^{\infty} \frac{2l+1}{4\pi} C_l P_l(x \cdot x'), \quad (2.5)$$

where x and x' are unit vectors on the sphere and the P_l's are Legendre polynomials. The power spectrum given by the C_l's contains all information about the angular distribution of the temperature anisotropies. The observational constraints on the power spectrum from the five-year survey of WMAP as well as a few other CMB experiments are shown in Figure 2.2.

What is the physics behind the power spectrum? The CMB fluctuations are seeded by a very early period of exponential growth, inflation, during which the scale factor a increases by an enormous factor e^N, with $N > 60$. This stretches random quantum fluctuations in the density field to the classical regime and yields a nearly scale-invariant spectrum of fluctuations, corresponding to a horizontal line in figure 2.2. When inflation ends, the Universe is reheated by decay of the inflaton field which produces a very hot relativistic fluid in which all particle species are coupled to each other, and which is supported against gravitational instability by radiation pressure. The radi-

ation domination causes the Universe to expand as $a \propto t^{1/2}$. Expansion lowers the temperature, and at some point the weak scattering rate of dark matter drops below the Hubble rate. This causes to dark matter decouple from the other particle species. Now lacking pressure support, the density perturbations in the dark matter fluid become unstable and grow. When the temperature reaches the eV-scale at $z \sim 1100$, electrons and nuclei recombine to form neutral atoms and the baryons fall into the gravitational wells already formed by dark matter. This collapse leads to a series of acoustic oscillations of the baryonic fluid. Recombination also causes the Universe to become transparent to photons which triggers the formation of the so-called last scattering surface, which is where the CMB photons last scattered. The first peak in the CMB power spectrum corresponds to the density perturbation scale that has just fallen into the potential well and reached maximum compression when the last scattering surface is formed. The other peaks are overtones of this wave corresponding to first decompression, second compression, etc. Therefore these acoustic peaks carry information about the sound speed at the time of recombination, which itself depends on the baryonic density. The sound speed can be measured from the ratio of the 1st and the 3rd peak heights, i.e. the peaks corresponding

to full compression, and the result corresponds to $\Omega_b h^2 \approx 0.02$.[1] The position of the first peak in l-space is given by the size of the horizon, since this determines which perturbation scale reaches first compression at the last scattering surface. At some redshift before decoupling, the energy density of matter and radiation are equal ($\rho_r = \rho_m$) and after that matter is dominant and the Universe expand as $a \propto t^{2/3}$. Therefore the matter density determines how much the Universe has expanded and fixes the horizon size at decoupling, which is reflected in the position of the first peak in the CMB power spectrum. The total amount of matter also affects the peak heights of all peaks and these two effects together determine $\Omega_m h^2 \approx 0.15$. Note that the measurements of Ω_b and Ω_m already indicate the need for non-baryonic dark matter. Finally, the position of the first peak as well as the low-l integrated Sachs-Wolfe effect provide a strong upper limit on the amount of curvature, while the total Ω is close to unity with the HST prior on $h \approx 0.7$ is taken into account. Dark energy is only very weakly constrained directly, but indirectly fulfills the need for the component energy densities to add up to $\Omega 0 \simeq 1$. The connection between the physics of the microwave background, the observables, and the cosmological parameters is discussed in detail in Hu et al. (1997, 2001).

The growth of baryonic structure in the Universe follows the decoupling of radiation and matter, and is largely caused by the evolution of the dark matter fluid. The early phase is characterized by small fluctuations in all components, $\delta = \delta\rho/\rho \ll 1$, which can be treated as linear perturbations to the smooth cosmological evolution. Still, solving the linear evolution is somewhat complicated since a number of physical processes play a part. Generically, the evolution of the density pertubation δ of any component (dark matter, baryons, radiation) obeys a second-order differential equation where the transition between oscillatory and growing/decaying solutions is dictated by the difference between pressure and gravity. However, the perturbations to the gravitational potential are sourced by the δ's of *all* components so the system is coupled. At early times, for example, radiation acts as a damping term for the potential and so it indi-

---

[1] The degeneracy with h^2 is due to the critical density $\rho_c \propto h^2$.
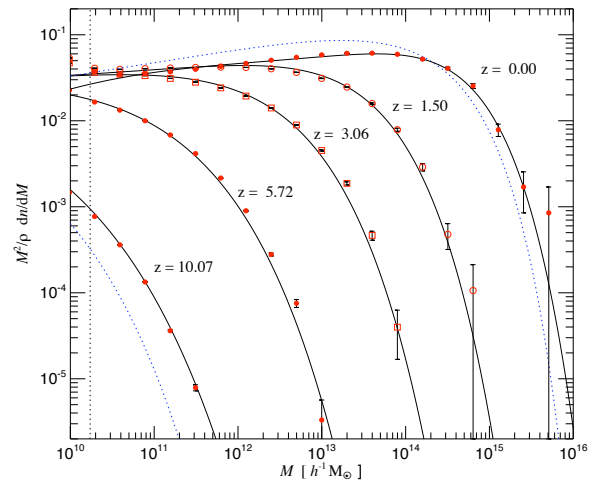
Fig. 2.3: Halo mass function at various redshifts as found in the Millennium simulation (Springel et al., 2005). The light-blue dotted lines are Press-Schecter models at $z = 10.07$ and $z = 0$.

rectly affects the evolution of dark matter perturbations. There is also a damping term connected to the expansion of the Universe, the size of which depends on whether the Universe is radiation- or matter-dominated. Before radiation-matter equality, dark matter pertubations only grow logarithmically whereas after, $\delta_{\rm DM} \propto a$. Another complication is that perturbations on small scales have longer time to collapse than perturbations on large scales, which need to enter the causal horizon first.

When δ becomes order of unity the linear treatment breaks down and higher order terms must be included. As usual, in the linear regime each Fourier mode evolves independently, but in the non-linear regime different modes become coupled. Hence, the growth of perturbations can only be followed analytically at relatively early times (depending on the scale of interest). For late times it is still possible to follow the statistical properties of the fluctuations, e.g. the spatial correlation function of density peaks, but otherwise a numerical treatment in the form of N-body simulations is necessary (section 4.2).

When a perturbation mode reaches the non-linear regime it collapses on a much shorter time-scale than the linear evolution. In cold dark mat-

ter models, the first perturbations to collapse are the smallest-scale ones which leads to the concept of hierarchical structure formation (the 'bottom-up' scenario): small-scale objects merge and form larger halos through a continuous assembly process, which involves both accretion and violent mergers. Stars and galaxies form from collapsing gas clouds within the dark matter halos in a highly complex, non-linear process which is very dependent on the environment. Feedback processes and turbulence as well as merger history play important roles in the efficiency of star formation. These processes are studied in numerical simulations but are still not quantitatively well understood.

The large-scale formation of structure is reasonably well understood in terms of the halo mass function, i.e. the number of halos in a given mass interval. Of course, this distribution is connected to the initial conditions for the formation of structure observed in the CMB. The link between the two is a prescription for halo formation, either in the form of numerical simulations (section 4.2) or an analytical approximation. The most popular analytical approach is the extended Press-Schecter formalism (Press & Schechter, 1974; Sheth & Tormen, 1999; Zentner, 2007). This relates the perturbations in the linear regime to the number of collapsed halos of a given mass through a 'magical' formula,

$$\frac{\mathrm{d}n(M,z)}{\mathrm{d}M} = -\sqrt{\frac{2}{\pi}} \frac{\rho_m \delta_c}{3M^2 \sigma} \frac{\mathrm{d}\ln\sigma}{\mathrm{d}\ln R} e^{-\delta_c^2/2\sigma^2}. \quad (2.6)$$

The density fluctuations are approximated as a smoothed Gaussian field, and if a spherical overdensity on the scale R is greater than a critical value δ_c, that scale collapses. The variance of the smoothed field is $\sigma(R, z)$ which is only weakly mass-dependent. Hence the total mass dependence of the halo mass function is dominated by the M^{-2} factor. The halo mass function has been found to be in agreement with observations of the UV luminosity function at high redshift (Bouwens et al., 2008). Figure 2.3 shows the halo mass function at various redshifts as found in a cosmological numerical simulation, as well as the Press-Schecter prediction. The $1/M^2$-dependence corresponds to a horizontal line in the figure.

While properties of the halo distribution are reasonably well understood, there is no theory that is able to predict the formation or structure of individual haloes. Instead, numerical simulations have

become a very important tool. I return to this subject in section 4.

2.3 Evidence for dark matter

There are several reasons for postulating the existence of dark matter. As discussed above, the CMB anisotropies indicate that the baryons comprise less than one-sixth of the total matter density of the Universe. Independent and complementary evidence for dark matter comes from astrophysics where dark matter is introduced as 'missing mass'. Here I summarize this evidence, but the methodology is discussed in more detail in section 4.3.

The most important type of analysis for establishing astrophysical dark matter is kinematical analyses of stars in galaxies and galaxies in galaxy clusters. The line-of-sight velocity of an object can be measured spectroscopically through the Doppler shift of emission and absorption lines, both in stellar spectra and in the 21 cm spin-flip radio emission of neutral hydrogen.

An important method to probe the gravitational potential of galaxies is the measurement of rotation curves of spiral galaxies, pioneered by Rubin and Ford in the 1970's. The velocity of a star in a circular orbit is $v_c^2 = GM(r)/r$, where $M(r)$ is the mass interior to the orbital radius. Typically, there is a steep rise of the circular velocity within the central bulge, but then it becomes roughly constant with radius. Figure 2.4 shows an example of such a measurement. The light distribution in the disk is approximately exponential with a scale length in the range of kpc, and most of the luminous matter is contained within a few scale lengths. If mass follows the distribution of light, the rotation curve should become simply Keplerian $v_c^2 \propto r^{-1}$ in the outer parts of the spiral, but the observations instead imply a mass profile $M(r) \propto r$. This cannot be explained by the stellar or diffuse contributions from either the disk, the bulge, or the stellar halo, and one is forced to introduce an extra dark halo.

Historically, the first indication of missing mass was found in galaxy clusters. Zwicky (1933) applied the virial theorem to the redshift distribution of galaxies in the Coma cluster and found that the inferred mass was much greater than the luminosity of the cluster could account for. He concluded that a dominant amount of the matter in Coma was
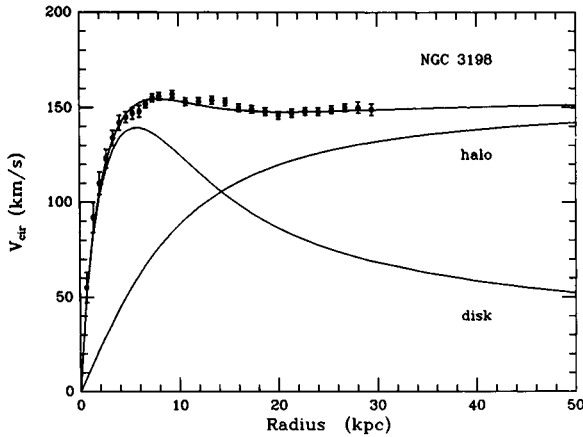
Fig. 2.4: The rotation curve of NGC3198, and a fit-
ted two-component model consisting of an
exponential stellar disk and a dark matter
halo (van Albada et al., 1985).

'dunkles Materie', dark matter. The virial theorem
in its most simple form relates the kinetic energy of
a stable system of self-gravitating particles to the
potential energy of the system as $2K = -U$. The
total kinetic energy of the galaxies can be estimated
from their line-of-sight velocities. Additional evi-
dence for the large mass of galaxy clusters comes
from x-ray observations. The intracluster medium
(ICM), an ionized plasma which reaches temper-
atures up to 10^8K, produces x-rays through ther-
mal bremsstrahlung. Given that clusters are stable,
the thermal pressure of the ICM must support the
ICM against collapse in the gravitational field of
the cluster. The pressure can be determined from
the x-ray observations and, generally, the result-
ing mass estimate is found to be much larger than
the contribution from the ICM itself or the contri-
bution from the individual galaxies. Thus, x-ray
observations show that 80–90% of the matter in
galaxy clusters is dark and distributed throughout
the clusters. Another probe of the matter in galaxy
clusters is gravitational lensing. A galaxy cluster
can act as a gravitational lens which distorts the
light of background galaxies or quasars. The de-
flection angle of a light ray is propotional to the
mass of the lens and the inverse impact parameter,
$\theta \propto M(r)/r$. Observations of background galaxies
can be used to determine the mass distribution of

the lensing cluster. Again, the measured total mass
is much greater than that provided by the luminous
component.

A relatively recent observation of a merging clus-
ter system, known as the Bullet Cluster, provides
extremely convincing evidence for the presence of
dark matter (Markevitch et al., 2004). A small clus-
ter has 'shot' through a larger one on a trajectory
perpendicular to the line of sight. The x-ray emit-
ting ICM is highly disturbed, and the bullet shows
a clear bow shock from which the relative speed
of the impact can be determined. But lensing ob-
servations show that the majority of the matter is
found in two clumps on either side of the ICM. This
shows that the collisional gas has been slowed down
by the merger and separated from the gravitating
mass in the form of collisionless dark matter.

Non-baryonic dark matter

The astrophysical motivation for dark matter is to
solve the problem of missing mass, and the ob-
servations do not say much about the nature of
dark matter, except that it cannot interact with
light. But cosmological observations clearly show
that dark matter must be non-baryonic, through
two pieces of evidence. The first is from the im-
print of baryonic acoustic oscillations on the CMB
in the potential formed by dark matter, already dis-
cussed. The second is the formation of elements in
the early, hot universe as described by Big Bang
Nucleosynthesis (see Iocco et al. (2009) for a re-
view), which relates the amount of baryons to the
abundance of light elements. Nucleosynthesis takes
place when the Universe has cooled to a tempera-
ture below the nuclear binding energy scale of MeV.
Above this temperature the reaction $n + p \leftrightarrows D + \gamma$
is in equilibrium, so as soon as a deuterium nu-
cleus is formed it is split again by a high energy
photon. But below this temperature there are rel-
atively few photons with an energy greater than
the deuterium binding energy of 2.2 MeV and the
reaction proceeds only in one direction. Since the
number density of photons is much greater than
that of baryons, $n_\gamma / n_b \sim 10^{10}$, the production only
starts at ~ 0.1 MeV, and deuterium can then fuse
into ^{3}He and ^{4}He. However, the low rate of nu-
clear interactions at this temperature, as well as
the absence of a stable isotope with five nucleons,
means that only trace amounts of heavier elements

are produced. The amount of deuterium which is not processed into helium is strongly dependent on the amount of baryons since that determines the number of protons available to fuse with. Therefore, the primordial deuterium abundance is a particularly good tracer of the baryon density. It can be measured in quasar spectra where intergalactic hydrogen clouds distributed along the line-of-sight absorb at the Ly-α transition. This deuterium is believed not to have been enriched by astrophysical processes. The measured deuterium abundance implies that the amount of baryons is $\Omega_b \simeq 0.04$, in good agreement with the CMB measurement. This underlines the non-baryonic nature of dark matter.

There are, of course, non-baryonic particles in the standard model. However, the charged leptons cannot constitute the dark matter as they do not clump together and they would in any case easily be observed. The other possibility, neutrinos, are abundant in the form of a cosmic neutrino background, formed similarly to the CMB through freeze-out in the early Universe. However, standard model neutrinos are ruled out as the dominant form of dark matter because they would need a mass of about 11 eV to contribute the necessary energy density, in conflict with laboratory bounds. Neutrinos can still contribute a fraction of the dark matter, but this amount turns out to be severely constrained since neutrinos are relativistic in the early universe. This means that they do not clump together below a free-streaming scale, roughly cH^{-1}, which suppresses structure formation below that scale. This suppression is not seen in the measured galaxy power spectrum which suggests that $\Omega_\nu < 0.02$ (e.g. Hannestad et al., 2008), and that can be used to put a strong upper limit on the neutrino mass. The suppression of small-scale power is generic to any type of dark matter that is relativistic at decoupling, socalled hot dark matter. Hot dark matter is ruled out by the measured power spectrum but warm dark matter, which is slightly relativistic at decoupling, can still be accommodated. In any case, the dark matter must be a new type of particle from beyond the standard model of particle physics.

3. PARTICLE NATURE OF DARK MATTER

The puzzle of dark matter can only be solved by physics beyond the standard model and therefore dark matter has attracted a lot of attention from the high energy physics community. In this chapter, I briefly review some of the better motivated dark matter particle candidates that have been put forward, and I discuss the experimental efforts that may contribute to the identification of dark matter. This section is based on some of the several good reviews and lecture notes on the subject (Smith & Lewin, 1990; Jungman et al., 1996; Bertone et al., 2005; Hooper, 2009; Bergstrom, 2009; D'Amico et al., 2009).

3.1 Theoretical candidates

There are certain requirements of any good theoretical candidate for dark matter. Firstly, there should be a production mechanism that accounts for the abundance of dark matter and makes sure that the dark matter is cold, i.e. non-relativistic. Secondly, the particle should not be in conflict with present experimental or observational constraints.

The second requirement implies that the dark matter particle cannot have an electromagnetic coupling, at least not with a charge of order unity as the charged standard model particles. Nor can it have strong interactions since it would then couple to quarks and form nuclei. However, weak interactions can be accommodated without violating any constraints, and they are in fact welcome for a viable production mechanism. Weak interactions turn out to be very attractive since dark matter can then be produced in the early Universe by freeze-out from thermal equilibrium, in much the same way as neutrinos. The relic abundance $\Omega_{dm}h^2$ is independent of the mass of the DM particle, but it does depend on the thermally-averaged cross-section. It turns out that for weak scale interactions of a particle with mass $\sim 100\,\mathrm{GeV}$, $\langle \sigma v \rangle \approx 3 \times 10^{-26}\,\mathrm{cm^3 s^{-1}}$, the abundance is of order unity. Hence, a thermal relic in the form of a WIMP, a weakly interacting massive particle, is an attractive candidate for dark matter.

A very popular class of theories in which a WIMP can be found are supersymmetrical extensions of the standard model (SUSY). SUSY is introduced in an attempt to explain some of the many loose ends of the standard model, including the mass hierarchy and the breaking of the electroweak symmetry. It is a new symmetry between bosons and fermions so that every standard model particle gets a new SUSY partner and the particle spectrum is doubled. There is an enormous amount of freedom in this framework with more than 100 possible new parameters—couplings, mixing angles, etc.—and typically the phenomenology of some limited subset of this parameter space is studied. In some cases SUSY is global symmetry but it can also be promoted to a local symmetry, in which case an effective theory of gravitation mediated through gravitons appears. A common ingredient is a new conserved charge called R-parity which is positive for standard-model particles but negative for SUSY partners and hence breaks SUSY. If SUSY were a perfect symmetry, the superpartners would have the same masses as their standard model counterparts, and they would already have been produced in collider experiments. But if SUSY is broken, the new particles acquire higher masses, typically on the TeV-scale. The conservation of R-parity also means that the number of SUSY-particles is conserved, and therefore the lightest supersymmetric particle (LSP) is stable. This LSP is a good WIMP-type dark matter candidate which is electrically neutral but has weak scale interactions and a mass of $\mathcal{O}(100\,\mathrm{GeV})$. The LSP is a linear combination of the superpartners of the gauge bosons, the bino, the wino, and the higgsino, but the exact nature of the LSP, its mass, and its couplings depend on the particular SUSY model. Whether SUSY is realized in nature can be tested at the Tevatron or the Large Hadron Collider which may reach the required energy to produce SUSY par-

ticles. Most likely, colliders cannot show that the neutralino constitutes the dark matter directly and so other experimental efforts are still required.

Another DM candidate is found in Kaluza-Klein (KK) theories of universal extra dimensions. In the simplest case there is a single extra spatial dimension which is compact, meaning that it has a circle U(1) geometry with a size R. This geometry naturally leads to standing waves along the extra dimension with energy $E_n = n/R$ where n is the excitation. Such waves can be associated with standard model particle fields where the standard model particle is the ground state and the excitations are additional new particles with mass $m_n = E_n + m_{SM}$. This sequence is referred to as a KK tower. Momentum conservation in the extra dimension means that the lightest $n = 1$ state is stable. The KK states associated with all standard model bosons, except the W and the gluons, as well as the KK neutrinos, have no electric charge and do not interact strongly, and they are therefore WIMPs (Cheng et al., 2002). In particular, if the characteristic size is $R \sim \text{TeV}^{-1}$ one finds an almost degenerate spectrum of KK-states of the various standard model fields so that the WIMP is a mixture of several states with $\sim$TeV mass. Typically, the KK WIMP can pair annihilate into standard model particles and it can therefore be produced as a thermal relic in a similar fashion to SUSY dark matter.

A different candidate arises from the experimental evidence that neutrinos oscillate between flavors which implies that the neutrino masses are non-zero, and that the weak eigenstates $\nu_{e,\mu,\tau}$ are superpositions of three mass eigenstates $\nu_{1,2,3}$. There are two types of mass terms that can generate a neutrino mass, a Dirac term similar to the mass terms for the other standard model particles, or a Majorana term which is allowed for neutrinos since they carry no charge. Both types of mass term couple the left-handed weak SU(2)-doublets to right-handed singlets, which are in effect a new type of right-handed neutrino that must be added to the standard model. Experimental bounds on the effective mass of the ν_e and on the square-mass differences $\Delta m_{ij}^2 = m_i^2 - m_j^2$ mean that the active neutrinos have masses less than $2\,\text{eV}$ and that at least two masses are non-zero (Gonzalez-Garcia & Maltoni, 2008). The smallness of the neutrino mass scale, six orders of magnitude below the charged lepton masses, is difficult to explain theoretically but an

attractive solution has been proposed in the form of the see-saw mechanism involving Majorana neutrinos. In this scenario, a heavy right-handed neutrino mixes with the massless left-handed neutrino to form an active mass eigenstate with a small, but non-zero, mass and a sterile mass eigenstate with a mass similar to the right-handed neutrino's. Often, this heavy mass scale is taken as the scale of Grand Unified Theories (GUTs), $\sim 10^{16}\,\text{GeV}$, in which case the mixing is large, but it could also be as low as the keV-scale if the mixing is small. This latter case is referred to as a sterile neutrino which is a dark matter candidate (Dodelson & Widrow, 1994; Kusenko, 2009). Unlike active neutrinos and WIMPs, the sterile neutrinos are not produced by thermal freeze-out in the early Universe, but other production mechanisms have been proposed which could yield cold or warm keV-mass sterile neutrino dark matter with the correct abundance. The sterile neutrino models are attractive in the sense that they can explain dark matter, as well as leptogenesis and neutrino oscillations, at the expense of adding only a few right-handed singlets to the standard model particles.

The last example of a theoretically motivated dark matter candidate is the axion which arises in the context of the strong CP-problem. Experimentally, the strong interaction is not found to violate the conservation of charge conjugation–parity (CP), despite terms in the QCD Lagrangian that should do so unless a CP-violating phase is fine-tuned to be $\ll 1$. Peccei & Quinn (1977) proposed a dynamical mechanism in which the phase is promoted to a field associated with a global U(1) symmetry. This symmetry is spontaneously broken at an energy level f_a and the broken symmetry drives the phase towards zero. The axion appears as a result of this symmetry breaking with a mass $m_a \approx 10^{16}\,\text{eV}^2/f_a$. However, the scale f_a is not predicted by the Peccei-Quinn model. Experimental searches limit the mass of the axion to be less than meV, i.e. 14 orders of magnitude smaller than the typical scale of WIMPs. Even so, axions are still cold dark matter because they are produced in a peculiar fashion with essentially no kinetic energy. It turns out that the experimentally allowed mass range yields cosmological abundances Ω_a of order one. The axion couples to the photon through a loop diagram, and this forms the basis for experimental searches using microwave cavities or the ro-

tation of linearly polarized light. This coupling also implies that the axion can decay, but with a lifetime much longer than the age of the Universe. Hence, the axion is a well motivated and experimentally accessible cold dark matter candidate, even if it can appear somewhat overshadowed by WIMPs in the literature.

3.2 Indirect detection

Indirect detection refers to the observation of decay or annihilation products of dark matter in an astrophysical context. Depending on the nature of the dark matter particle, the observed particles can be any of the stable standard model particles. A difficult problem is to distinguish the dark matter signal from astrophysical backgrounds, and to achieve this discrimination both the flux, energy, and origin of the signal should ideally be determined.

For annihilations, the signal rate is proportional to the square of the dark matter number density. Hence, the centres of dark matter halos are the prime sources for observing annihilation products of WIMPs. The types of annihilation products are very model-dependent and the possibilities include high energy gamma rays and cosmic rays, where especially positrons and anti-protons are promising. In the past year or two the physics that can affect an annihilation signal from the Galactic halo has been intensely studied. This is partly due to a number of new cosmic ray observatories and partly to improvements in numerical simulations of the formation of dark matter structures, which allow the mass distribution in both the Galactic halo and in substructures to be explored (Kuhlen et al., 2008; Diemand et al., 2008; Springel et al., 2008b).

The smoking gun of indirect annihilation signals is a line in the gamma ray spectrum from the Galaxy or from the density peaks associated with Galactic substructure. The direct annihilation $\chi\chi \rightarrow \gamma\gamma$ proceeds through some type of loop diagram, and the line would straight-forwardly yield the mass of the annihilating WIMP, $E_\gamma = M_\chi$. This signal would be relatively easily to distinguish from astrophysical backgrounds both through the narrow width of the line (since the dark matter is non-relativistic) and through the directionality of the signal. However, this is not necessarily a very likely signal to observe since it must be sup-
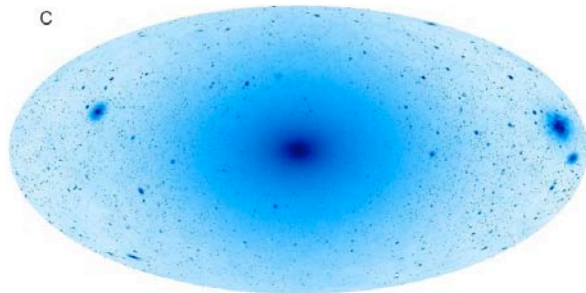

Fig. 3.1: Surface brightness signal from annihilating dark matter in the main Galactic halo and associated substructures, as predicted by the Via Lactea II simulation. Figure from Kuhlen et al. (2009).

pressed at the one-loop level. SUSY neutralinos, for example, have a very low cross section for the annihilation. A stronger gamma ray signal can be produced by decays of annihilation products, especially π^0's, but this signal has a broad spectrum and which makes it more difficult to identify in the presence of backgrounds. The FERMI satellite observatory (Morselli et al., 2002), launched in June 2008, is in an excellent position to detect a gamma ray signal from dark matter annihilation. This is a survey instrument which will produce full sky maps with high angular and spectral resolution. Figure 3.1 shows a prediction of the annihilation signal from the Galactic halo and its substructure, based on a cosmological numerical simulation. A complementary method is gamma ray observations with Air Cherenkov Telescopes such as H.E.S.S. (Aharonian et al., 2008, 2009a), MAGIC (Lombardi et al., 2009), and VERITAS (Wood et al., 2008). They identify gamma rays through the Cherenkov light of super-luminal muons produced by the gamma ray's interaction in the upper atmosphere. These telescopes have the advantage that they can be pointed to a target, e.g. the dense dark matter halo of a dwarf spheroidal galaxy, and integrate for longer exposures. On the other hand they are only sensitive to energies above $\sim 100\,\text{GeV}$, while FERMI probes the range $0.1 - 300\,\text{GeV}$.

The PAMELA satellite experiment (Adriani et al., 2009a,b) searching for cosmic ray antimatter recently reported two intriguing results: an excess of positrons relative to electrons at energies

above $10\,\mathrm{GeV}$ on one hand, and an anti-proton–to–proton ratio in agreement with expectations on the other. Both e^+ and $\bar{p}$ can carry a dark matter annihilation signal which can be distinguished from backgrounds as a spectral feature. Astrophysical sources in general produce copious amounts of electrons and protons and only few positrons and anti-protons, but the positron–to–electron ratio (or $\bar{p}/p$) can be boosted by dark matter annihilations which yield equal amounts of both. At the same time the ATIC balloon experiment reported a rise in the total flux of electrons and positrons above $300\,\mathrm{GeV}$, peaking at 600 GeV, and with a rather sharp cut-off in the spectrum which is very suggestive of annihilation of a WIMP with mass equal to the cut-off energy (Chang et al., 2008). These observations caused a flurry of different interpretations, but the general consensus now seems to be that the results are caused either by nearby astrophysical sources or by annihilating dark matter. The first type of explanation involves positron production in nearby pulsars (Profumo, 2008), in supernova remnants, or in the magnetic stellar wind of very massive stars that explode as supernovae (Biermann et al., 2009). The dark matter explanation requires annihilation preferentially into leptons to avoid boosting the number of anti-protons (Cirelli et al., 2009b). More recently the FERMI observatory, which is also sensitive to electrons and positrons, rejected the large feature seen by ATIC but still reported a slight excess in the same energy range with much better statistics (Abdo et al., 2009; Bergström et al., 2009). This was corroborated by H.E.S.S. which also identified a high-energy cutoff (Aharonian et al., 2009b). Figure 3.2 summarizes the measurements of the $e^+ + e^-$ flux. However, there is some uncertainty about both propagation of high energy cosmic rays through the galaxy as well as the background modeling (Grasso et al., 2009). More experimental results from both FERMI and PAMELA are expected very soon, but it is unclear if these will be sufficient to distinguish between the pulsar and the dark matter interpretations. Quite generically, the dark matter interpretation requires the annihilation to be boosted relative to the signal expected from WIMPs in a smooth halo with the annihilation cross-section required for freeze-out in the early Universe. This can perhaps be achieved by the Sommerfeld effect, which is a low-velocity boost to the annihilation
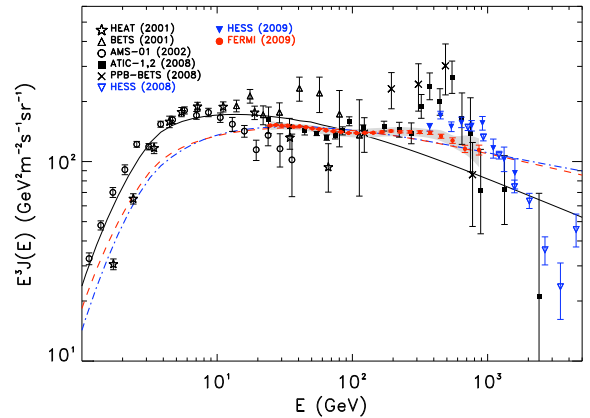

Fig. 3.2: Measurements of the cosmic ray $e^+ + e^-$ spectrum. The FERMI measurements have the best statistics so far and are in reasonable agreement with the HESS results. The solid line is the conventional background model and the dashed and dot–dashed lines are different model with non-standard injection spectra. Figure from Grasso et al. (2009).

rate (e.g. Lattanzi & Silk, 2009), with an additional contribution from clumping of dark matter into substructures of the main halo. On the other hand, the dark matter interpretation implies that a large amount of radiation has been produced by annihilation in halos over the history of the Universe, which may be in conflict with the observed level of the diffuse gamma ray background and could also affect the reionization history of the Universe (Belikov & Hooper, 2009; Cirelli et al., 2009a; Profumo & Jeltema, 2009).

A much more nearby source where annihilation is expected to take place is the Sun. A WIMP in the Galactic halo that passes through the Sun can lose energy through elastic scattering off a nucleus and become gravitationally bound. Eventually it will scatter again and sink to the centre of the Sun, and through this process the density of WIMPs in the centre will increase until it is large enough to become limited by annihilation. Due to the extreme density of the environment, the only annihilation products that can escape the Sun are neutrinos, which are typically secondary annihilation products but may even be primaries. These

neutrinos are very energetic, $E_\nu = \mathcal{O}(100\,\text{GeV})$, and can be detected in neutrino telescopes such as Super-Kamiokande (Desai et al., 2004) or IceCube (Deyoung, 2009). If the WIMP accretion is balanced by annihilation, the limiting factor is the nuclear scattering cross section that determines the efficiency of accretion, not the annihilation cross section. Therefore the neutrino searches probe the same parameter space as direct detection experiments, discussed below. The direct searches seem to rule out a neutrino detection if the accretion is governed by spin-indepedent interactions while the spin-dependent channel is still a possibility (see Hooper, 2009).

Unstable dark matter candidates can also be detected indirectly through their decay. In this case the rate scales with the number density, so the centres of halos are again the most promising target. For sterile neutrinos there is a suppressed one-loop decay into an active neutrino and an x-ray photon which yields a line at $E_\gamma = M/2$ in the keV range. Unfortunately galaxies and galaxy clusters have fairly large x-ray backgrounds, but prime targets are the Milky Way dwarf satellites, which are devoid of x-ray emitting gas, or the dark matter concentration of the Bullet Cluster where the hot gas has been removed by the collision (Riemer-Sorensen et al., 2007; Riemer-Sørensen & Hansen, 2009). The lack of signals has been used to rule out large parts of the mass-mixing angle parameter space (Kusenko, 2009).

There are already a number of unexplained astrophysical signals that have been analyzed in the dark matter context. The EGRET gamma ray satellite observatory measured a diffuse flux of gamma rays with a spectral distribution that could be explained by annihilating dark matter. However, early FERMI data do not confirm this excess (Sgrò, 2008). The INTEGRAL satellite has measured a flux of 511 keV photons from the Galactic center which is roughly circularly symmetric with an angular extent of a few degrees (Churazov et al., 2005). The simplest dark matter interpretation of this signal requires a particle with a mass of at most a few MeV which interacts through a new, light boson in order to avoid being produced overabundantly in the early Universe. An interesting alternative is TeV-scale exciting dark matter which has two states separated by $\Delta E \approx 1\,\text{MeV}$ (Finkbeiner & Weiner, 2007). Finally, there is a residual Galactic foreground signal in the WMAP measurements found in a region extending $\sim 20°$ around the Galactic centre, known as the WMAP Haze (Dobler & Finkbeiner, 2008). This emission could be explained by dark matter annihilating to e^+e^--pairs which then produce synchrotron radiation in the Galactic magnetic field. FERMI should be able to probe the dark matter origin of the WMAP Haze (Hooper et al., 2008).

To summarize, indirect detection offers a promising method of detecting some of the most popular dark matter candidates, and also to probe the properties of dark matter halos *in situ*. A generic difficulty is to identify the signal at high significance from astrophysical backgrounds and to rule out an unknown astrophysical nature of the source.

3.3 Direct detection

Since WIMPs are weakly interacting, it is reasonable to expect that it may be possible to measure the scattering of Galactic WIMPs off nuclei directly. This idea forms the basis of dark matter searches in direct detection experiments.

Nuclear scattering

The basic process to consider is elastic scattering of a WIMP with a nucleus. The interaction cross-section of this process is generally model-dependent but the observable energy transfer can be calculated from the kinematics alone. The energy transfer depends on the WIMP mass m_χ and the mass of the nucleus M as

$$E_{\text{rec}} = \frac{\mu^2 v^2 (1 - \cos\theta)}{M}, \qquad (3.1)$$

where $\mu = m_\chi M/(m_\chi + M)$ is the reduced mass of the system, v is the relative speed, and θ is the scattering angle of the WIMP. This turns out to be on the scale of tens of keV with a scatter of one magnitude in either direction, depending on the mass of the target nucleus and the WIMP mass. The recoil energy spectrum is given by

$$\frac{\mathrm{d}N}{\mathrm{d}E_{\text{rec}}} = \frac{\sigma_0 n_\chi}{2\mu^2} F^2(q) \int_{v_{\text{min}}}^\infty \mathrm{d}v \frac{f(v)}{v}, \qquad (3.2)$$

where σ_0 is the cross-section at vanishing momentum transfer, n_χ is the local number density of dark

matter, $F^2(q)$ is the nuclear form factor which depends on the momentum transfer q, and $f(v)$ is the speed distribution of WIMPs in the laboratory frame. The speed distribution vanishes at speeds greater than the local escape velocity, and in any realistic detector there is a minimum recoil energy detection threshold below which no signal can be seen, and therefore the lower limit of the integration is $v_{\min} > 0$.

The physics of the WIMP is contained in σ_0 which in general contains both spin-dependent and spin-independent contributions. The spin-dependent term requires interaction with an unpaired nucleon, while the spin-independent term is coherently enhanced across all nucleons, which means that the WIMP essentially interacts with the whole nucleus. This enhancement boosts the interaction cross-section by a factor A^2. At higher momentum transfer this coherence effect is lost as described by the nuclear form factor $F^2(q)$. The spin-independent term receives contributions from the direct couplings to protons and neutrons and the coupling through a loop diagram to gluons.

Detection strategies

The keV-scale nuclear recoil is extremely difficult to distinguish from backgrounds in a detector and at least three methods, or combinations of methods, are being employed in present experiments. The first is detection through the heat (phonons) which is deposited into the detector. This can be measured as a temperature change in cryogenic bolometers which are kept at a critical temperature close to the super-conducting phase transition. The recoil energy deposited into phonons pushes the temperature above this transition so that the electrical resistance changes abruptly and measurably. The second method is to detect ionization produced as the recoiling nucleus loses its energy. In a gas or liquid time projection chamber (TPC), this ionization is drifted to a cathode by a magnetic field, where the signal is amplified in an electron avalanche and can be read out as a current in the cathode. This can be achieved with both liquid and solid state materials. A similar principle can be utilized in semiconductor detectors. Finally, the detector can be constructed with a scintillating medium which emits a fraction of the deposited energy as scintillation light that can be measured by photomulti-

pliers. A few of the specific experimental set-ups are discussed in section 3.4.

The main issue in detector design is to minimize backgrounds while increasing the fiducial detector mass. The main sources of background include muons produced by cosmic rays and radioactivity from impurities in the materials in the detector itself or its surroundings. The cosmic rays can be reduced by placing the detector deep underground in mine shafts or under mountains while radioactive backgrounds are minimized through the choice of materials and through shielding. Even so, unwanted sources will still deposit energy in the detector at some level, and it is necessary to be able to discriminate against such events. By far the most common approach is to build a very well defined detector in which backgrounds are reduced to extremely low levels. Most backgrounds, such as radioactively produced gammas and betas, will interact electronically and the detector can be designed to produce distinguishable signals for electronic and nuclear interactions. This can be achieved by the timing of scintillation signals or by the rate of energy loss through ionization, and in many designs two of the three signals (heat, ionization, scintilation) are combined for a more efficient background rejection. However, the need for a well-defined detector means that it is more difficult to scale up in mass. This is a problem since the sensitivity of a given design can only be improved by reducing backgrounds or increasing the target mass. Liquid noble gas TPCs seem to offer one way out of this problem. If electronic backgrounds can be separated then the main problem is neutrons from radioactive decays which are an unavoidable source of noise. Hence a WIMP signal must be greater than this background to be detected.

A different approach to background rejection is based on a novel time-dependence of the expected dark matter signal (Drukier et al., 1986; Freese et al., 1988). The motion of the solar system in the Galaxy means that the detector is sweeping through the dark matter halo at a velocity $v_\odot \sim 220 \, \mathrm{km\,s^{-1}}$, but the additional rotational motion of the Earth with $v_\oplus \sim 30 \, \mathrm{km\,s^{-1}}$ around the Sun is superimposed on top of this. This means that at one point the detector is moving slightly faster with respect to the halo and half a year later it is moving slightly slower. Hence, there is an annual modulation of the mean WIMP speed in the detec-
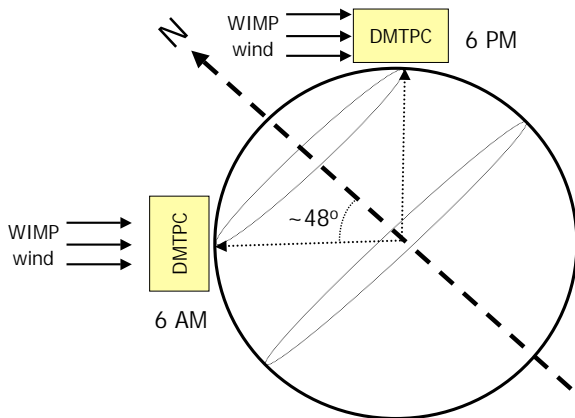
Fig. 3.3: The daily variation of the direction of the WIMP wind in a detector, in this case the DM-TPC prototype located at 42°N. Figure from Sciolla (2008).

tor system which translates directly into an annual modulation of the signal rate, which is expected to be at the level of a few percent. This can be exploited in a massive detector in which the WIMP interaction rate is orders of magnitude greater than in the zero-background detectors. There will be a sizable, even dominant, background but the dark matter signal can be recognized by the presence of an annual modulation with the correct phase. It is of course necessary to make sure that no background can mimic the annual modulation.

A final possibility for background discrimination is to build a detector which is sensitive to the direction the of the nuclear recoil (see Sciolla & Martoff, 2009, for a review). The WIMP wind induced by the motion of the Sun means that WIMPs will predominantly pass through the detector in one direction at any given time. Therefore the nuclear recoils will also tend to travel in one direction, although the signal is degraded since there is a distribution of scattering angles. Though it is easily possible for a background source to induce a directional signal, that direction would be constant in the laboratory frame whereas the WIMP signal changes direction in the laboratory during the day, see figure 3.3. Hence, one advantage of this strategy is that a WIMP signal is unambiguously astrophysical. Another advantage is that such a detector design is in fact a WIMP telescope. After a first detection of

WIMPs is established, a direction sensitive detector can proceed to do 'WIMP astronomy', mapping out the properties of the local dark matter velocity distribution.[1] Analyses have shown that only about ten events are needed to distinguish if those events are due to a directional WIMP signal or an isotropic background (Morgan et al., 2005). However, this is for an ideal detector which is able to measure the recoil track in three dimensions and which can determine the sense of the recoil trajectory. If these requirements are not met, the number of events needed is increased by roughly one order of magnitude (Morgan & Green, 2005) and it increases even more if the WIMP signal is subdominant to an isotropic background. Also, it is much more difficult to determine the sense and orientation at very low energies and correspondingly short tracks (Green & Morgan, 2008).

Although there are ideas to use anisotropic crystal detectors or nuclear emulsions, the most promising type of detector for this purpose is a gaseous TPC. The nuclear recoil produces a cloud of ionization which is drifted onto a mesh of cathode (or anode) wires by an electric field. There, the x-y position of the ionization cloud can be measured from the currents induced in the wires and timing information can be used to constrain the z-position. Of course, there is a price to pay for being sensitive to the direction: in order for the nuclear recoil track to be measured, it must have some spatial extent which limits the maximum pressure. The pressure in turn limits the target mass that can be contained in a given volume. On the other hand, a lower pressure means an increase in the diffusion length of the electrons and ions, which tends to wash out the information about the original shape of the cloud. Ideally, the detector should not only be sensitive to the shape of the ionization cloud, it should also reconstruct the head and the tail. A number of collaborations are in various stages of R&D towards a viable direction sensitive gas TPC for dark matter searches, including DRIFT (Alner et al., 2005; Burgos et al., 2009), DM-TPC (Dujmic et al., 2008a,b), and NEWAGE (Miuchi et al., 2007).

---

[1] This ability is not completely unique to direction sensitive detectors as some information about the velocity distribution can be inferred from the energy spectrum even without directional information (Drees & Shan, 2008).

3.4   Present status

In this section, I review a selection of the more important present direct detection experiments, including detector design and target materials. The experimental effort is reviewed in e.g. Gaitskell (2004) as well as in numerous conference proceedings such as Baudis (2007a).

The CDMS experiment (Ahmed et al., 2009) in its latest configuration operates solid state cryogenic detectors made of germanium and silicium which measure events through heat and ionization. The design is mainly sensitive to spin-independent coherent interactions, but both detector types contain isotopes with an unpaired neutron which gives some sensitivity to spin-dependent neutron couplings. The ratio of the energies measured in phonons and in ionization, as well as signal timing, allows discrimination of electronic interactions at a level of 10^6. The released results are based on a total exposure of 121.3 kg-days exposure of the Ge detectors, and an older 12 kg-day Si exposure (Akerib et al., 2006), and in both cases no events passed the selection cuts. The lowest energy electronic recoils have also been used to constrain axion dark matter (Ahmed et al., 2009). The collaboration has proposed an upgrade, SuperCDMS, which will increase the sensitivity by an order of magnitude through a larger target mass and a deeper site for improved cosmic ray background shielding. A similar experiment, EDELWEISS, is also using cryogenic Ge detectors to detect events through heat and ionization, and they have achieved an exposure of 62 kg-days (Sanglard et al., 2005). An upgrade with more refined technology is taking data at the moment and is also a step towards a 100 kg-scale cryogenic detector, EURECA.

The XENON collaboration uses a liquid xenon TPC design in which the deposited energy produces both prompt scintillation light and ionization which is detected through a delayed scintillation signal. The relative strength of the two signals allows discrimination against electronic backgrounds and the detector is sensitive to spin-dependent couplings because about half of the naturally occurring Xe-isotopes have an unpaired nucleon. The collaboration has completed the XENON10 phase with a 5.6 kg fiducial mass design with no signal in either the spin-independent or the spin-dependent channels (Angle et al., 2008a,b), but the results must

be revised in light of a new measurement of the low energy scintillation light yield (Aprile et al., 2009). The current set-up, XENON100, with 65 kg fiducial mass is taking data and it is expected to reach an exposure of 6000 kg-days at the end of the year (Aprile & Baudis, 2009).

A very different design is that of COUPP (Bolte et al., 2007) which is a bubble chamber in which a superheated CF_3I liquid responds to the heat deposit by nucleation of the gas phase. The bubbles created in this way and can be seen by the naked eye and photographed. By optimizing the temperature and pressure of the chamber, it becomes impossible for electronic recoils to produce bubbles because they do not deposit sufficient energy rapidly enough to initiate nucleation. The choice of CF_3I as detector medium makes the design sensitive to spin-independent couplings through the heavy iodine nuclei and to spin-dependent proton couplings through the fluorine. A 1.5 kg prototype has been operated close to the surface for a 52 kg-day exposure and has set the presently most stringent limits on the spin-dependent proton coupling (Behnke et al., 2008).

The KIMS experiment, which uses scintillating crystals made of CsI(Tl), is sensitive to spin-dependent couplings to both protons and neutrons. Electronic background rejection is achieved through pulse shape discrimination, i.e. analysis of the time variation of the scintillation light. The experiment has published results on 3409 kg-days of exposure, providing the strongest constraint on the spin-dependent proton coupling (Lee et al., 2007).

Finally, one of the most important direct dark matter searches is DAMA, which has been running firstly the DAMA/NaI and then its successor DAMA/LIBRA, as well as other detectors. Their strategy is based on NaI(Tl) scintillation detectors without discrimination against electronic backgrounds. Instead they rely on the annual modulation of the signal rate to identify a dark matter signal. The only background discrimination is rejection of events that trigger more than one detector at the same time, which could for example be caused by cosmic rays but not by a weakly interacting particle. Indeed, with a very significant total exposure of 0.82 t-yr the collaboration has reported the observation of such an annual modulation in the single-hit events at very high significance over a period of 11 years (Bernabei et al., 2008).
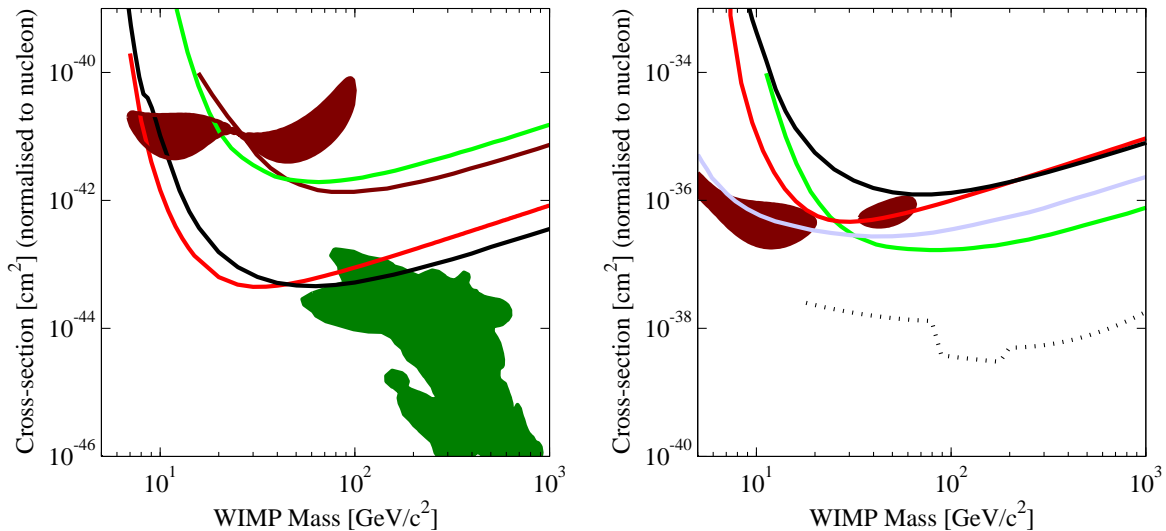
Fig. 3.4: WIMP mass vs cross section for the spin-independent coupling (left) and spin-dependent proton coupling (right). The data are CDMS (black), XENON10 (red), EDELWEISS (brown line), COUPP (light blue), KIMS (light green), and DAMA (brown shaded area). The dotted line is a constraint from SuperKamiokande on annihilation in the Sun (Desai et al., 2004). The dark green area is a prediction based on the Constrained MSSM supersymmetric model (Trotta et al., 2008). In such a plot there are certain assumptions about the halo model and the detector responses. These plots were generated on the webpage http://dmtools.berkeley.edu/limitplots/.

The phase of the signal is consistent with that expected from the motion of the Earth around the Sun. The collaboration emphasize that their result is strongly model-independent, i.e. it does not have to be caused by a conventional WIMP, but could also be induced by other dark matter candidates which may be rejected as background in other experiments.

The collaboration first claimed detection of the annual modulation signal one decade ago (Bernabei et al., 1999). This claim has been heavily debated and criticized for just as long, since it appears to conflict with the results of other searches. Some of the issues raised include the possibility of backgrounds with an annual modulation as well as a limited understanding of the detector. An interesting recent development is the issue of channeling: only a fraction of the nuclear recoil energy is actually detected as scintillation light while the rest is dissipated into heat, and this means the observed energy is QE_{rec} where Q is the quenching factor ($Q_{\mathrm{Na}} = 0.3$ and $Q_{\mathrm{I}} = 0.09$). However, some re-

coils will follow paths along the symmetry planes of the crystal lattice structure and effectively lose all their energy to electrons. This means that for a fraction of the events in the detector, the actual energy threshold (the minimum detectable nuclear recoil energy) is lowered, in the case of DAMA to as little as $2\,\mathrm{keV}$. This can affect the comparison with other searches with higher thresholds.

Figure 3.4 shows a selection of the recent experimental results. The claimed detection by DAMA is largely ruled out by other experiments, but the exclusion curves shown are derived for each experiment on its own. In the literature, there are also several joint analyses of the DAMA signal and the various null results which attempt to identify any allowed regions of parameter space in a consistent statistical analysis (e.g. Savage et al., 2009a,b; Fairbairn & Schwetz, 2009). There seems to be agreement that both in the spin-independent and the spin-dependent neutron channels, the dark matter interpretation of DAMA is ruled out by the null results of other experiments. On the other hand

there is a small low-mass window around $10\,\mathrm{GeV}$ for spin-dependent proton scattering which is consistent with all the experimental results, i.e. where nuclear scattering of WIMPs can explain the DAMA result without being in conflict with other experiments.[2]

3.5   Establishing a detection

Several different strategies are being pursued in order to reveal the particle nature of dark matter. All the possible paths are model-dependent to some degree, in the sense that no detection method can identify all possible candidates, and some of them relate only to very specific models. The various approaches also have astrophysical or experimental backgrounds from which the dark matter signal must be disentangled.

In light of this, it is reasonable to ask under which circumstances a detection of particle dark matter can be established. It is unlikely that any single experiment can establish this alone, as exemplified by the conflicting interpretations of the DAMA signal in light of other null results, or the ambiguous indirect signals from PAMELA and ATIC. Moreover, even if the existence of, say, the axion becomes established in laboratory experiments, it will be necessary to examine its properties carefully before its astrophysical impact can be determined. Therefore, it is likely that at least three independent, mutually consistent observations that can be interpreted as caused by dark matter are needed. For WIMPs, a direct detection signal should be established for more than one choice of target nucleus and in more than one type of detector design, and it would ideally be complemented by some annihilation signal from the Sun or the Galaxy.

The dark matter search undoubtedly requires a large effort with complementary contributions from many branches of experimental physics, but the near future seems promising with the FERMI telescope taking data, upgrades of direct detection experiments to tonne-scale masses, and constraints from the LHC on the underlying particle physics theory. Yet, it should be kept in mind that for all dark matter candidates there are regions of the

relevant parameter space in which the particle can evade identification by all of the planned experiments.

Of course, another question one might ask is whether we already have seen the particle nature of dark matter. The unexplained astrophysical signals, the DAMA modulation signal, and the cosmic ray anomalies have spawned a number of papers which attempt to explain (some of) these by a specific dark matter particle. To mention just a few, the inelastic dark matter scenario (Tucker-Smith & Weiner, 2001) involves a heavy doublet which has a mass-splitting between the two states $\approx 100\,\mathrm{keV}$ and only scatters inelastically. In that case, the modulation amplitude is boosted so that the DAMA result is fully compatible with other direct searches, and the expected spectrum is very different. A similar model is exciting dark matter (Finkbeiner & Weiner, 2007) where a mass splitting of $1-2\,\mathrm{MeV}$ explains the Integral $511\,\mathrm{keV}$ line as e^+e^- emission during deexcitation. The properties of these two scenarios are unified in the model of Arkani-Hamed et al. (2009) in which a new force carrier that couples to the dark matter generates a multiplet of states with various mass splittings. This new force carrier also induces a Sommerfeld enhancement so that the PAMELA and ATIC results can be explained without dark matter being produced overabundantly in the early Universe. The robustness of the unexplained signals when improved observations become available will determine the plausibility of these models.

---

[2] The COUPP result constrains this region somewhat (see figure 3.4) but the collaboration has not published sufficiently detailed data to be included in the spin-dependent analysis in Savage et al. (2009b).

4. DARK MATTER HALOS

In this section, I discuss the theoretical, numerical, and observational methods that are used to probe the physics of the dark matter halos that galaxies and galaxy clusters are embedded in. There are two major points of interest: is there an equilibrium configuration of a dark matter halo, and how is a halo assembled to reach that configuration?

4.1 Theory

Since dark matter particles are expected to have weak interactions at most, the dark matter fluid is effectively collisionless, so dark matter does not thermalize. Dark matter halos can be treated classically by Newtonian theory, i.e. there is no need to go to a full general relativistic treatment. The theory of collisionless gravitating systems has been developed in the context of stellar systems, but much of galactic dynamics can be applied directly to dark matter halos as well. As a result, this section is mainly based on the textbook of Binney & Tremaine (2008).

In the continuum limit the fundamental description of the dark matter fluid is the six-dimensional phase-space distribution function (DF) $f(x,v)\mathrm{d}x\mathrm{d}v$ which gives the number of dark matter particles in the (infinitesimal) phase-space volume $\mathrm{d}x\mathrm{d}v$. The physical number density is straight-forwardly

$$n(x) = \int \mathrm{d}^3 v f(x,v). \qquad (4.1)$$

More generally, the DF can be given in terms of any set of canonical coordinates $f(p,q)$. The DF obeys a conservation equation, the collisionless Boltzmann equation (CBE), which in Cartesian coordinates is

$$\frac{\partial f}{\partial t} + v_i \frac{\partial f}{\partial x_i} + \frac{\partial \Phi}{\partial x_i} \frac{\partial f}{\partial v_i} = 0, \qquad (4.2)$$

where $\Phi(x)$ is the Newtonian gravitational potential. Since dark matter is self-gravitating, the gravitational potential is sourced by the dark matter

itself through the mass density $\rho(x) = mn(x)$ as described by the Poisson equation,

$$\nabla^2 \Phi = 4\pi G\rho. \qquad (4.3)$$

To model a dark matter halo, one searches for simultaneous steady-state ($\partial f/\partial t = 0$) solutions of the CBE and the Poisson equation. If we consider a spherically symmetric gravitational potential $\Phi(r)$, this is obviously sourced by a spherically symmetric mass distribution, $\rho(r)$. The distribution function can only depend on angular momentum $L = r(v_\theta^2 + v_\phi^2)^{1/2}$ and on the Hamiltonain $H = \frac{1}{2}v^2 + \Phi(r)$. If we further assume that there are no bulk flows, the mean velocity components vanish, $v_r = v_\theta = v_\phi = 0$ and the velocity dispersion tensor

$$\sigma_{ij}^2(x) = \frac{1}{n(x)} \int \mathrm{d}v(v_i - \bar{v}_i)(v_j - \bar{v}_j) f(x,v), \quad (4.4)$$

is diagonal along the axes $(\hat{r}, \hat{\theta}, \hat{\phi})$. Since the orientation of the polar axis of the coordinate system is arbitrary, $\sigma_\theta^2 = \sigma_\phi^2$. On the other hand there is no reason to expect that the radial velocity dispersion should be equal to the tangential velocity dispersions. This motivates the introduction of the velocity anisotropy parameter (Binney, 1980),

$$\beta = 1 - \frac{\sigma_\theta^2}{\sigma_r^2}, \qquad (4.5)$$

which is zero for isotropic velocity dispersion tensors, $0 < \beta < 1$ for a radially biased tensor, and $\beta < 0$ in the case of tangential bias.

The CBE cannot immediately be applied to quantities that are observationally accessible, but instead one can take moments of the CBE towards this end. For a spherically symmetric system in a steady state, the first-order moment with respect to the radial velocity component yields one of the Jeans equations, often referred to as *the* Jeans

equation,

$$\sigma_r^2 \left(\frac{\mathrm{d}\ln\rho(r)}{\mathrm{d}\ln r} + \frac{\mathrm{d}\ln\sigma_r^2(r)}{\mathrm{d}\ln r} + 2\beta(r) \right) = -\frac{GM(r)}{r},$$
(4.6)

where $M(r) = 4\pi \int_0^r \mathrm{d}r' r'^2 \rho(r')$ is the mass interior to the radius r. As already hinted at in section 2.3, there are various observational methods to infer the mass profile of a dark matter halo, and the Jeans equation provides a link to the internal dynamics of the halo.

Even in the restricted case of spherical symmetry there is no unique equilibrium configuration. There are several potential-density pairs which simultaneously solve the Jeans and Poisson equations, but there is also al degeneracy between the radial velocity dispersion and the velocity anisotropy. Hence, additional constraints are needed. One possibility to find such constraints is to apply some set of first principles, such as the maximum entropy method. Based on the Shannon entropy, $S = \sum p_i \ln p_i$, this method identifies the most probable state of a system of particles, subject to a number of moment constraints such as the total energy or the volume of the system. The most probable state is the one that maximizes the Shannon entropy, and when this method is applied to an ordinary gas it yields the Maxwell distribution. However, when applied to a self-gravitating system it becomes clear that there is no upper bound to the entropy. The only apparent solution (Lynden-Bell, 1967) is the singular isothermal sphere, which has a constant velocity dispersion and $\rho \sim r^{-2}$, but this profile violates energy and mass conservation. The main reason for this behavior of self-gravitating systems is the non-extensive nature of the potential energy: if the system is divided into two isolated subsystems, the potential energy of the two parts is less than the potential energy of the total system (Padmanabhan, 1990, 2008). For this reason a lot of attention has been given to generalized non-extensive entropy functions such as the Tsallis entropy (Tsallis, 1988) which is based on q-exponentials (e.g. Vergados et al., 2008). So far, these approaches have not resulted in a definite answer either.

However, numerical simulations of the formation of structure suggest that there is a (near) universal mass distribution of relaxed halos, which is reached by halos irrespective of the cosmological model, the redshift considered, or the halo merger history, i.e. whether the halo has accreted smoothly in near isolation or it has been disturbed through major mergers. It is not understood why this equilibrium configuration is picked out. Some authors have emphasized the role of cosmology-dependent boundary conditions imposed by infalling matter, both during periods of steady accretion (secondary infall) and during major mergers (Gunn & Gott, 1972; Manrique et al., 2003, and references therein). This yields results which appear to be in good agreement with the numerical simulations. On the other hand, the universality appears to be more general phenomenon than suggested in these scenarios (Wang & White, 2009).

4.2   Numerical simulations

Perhaps the most important tool in the study of dark matter halos is numerical N-body simulations, both in the form of pure dark matter simulations and simulations that also include hydrodynamical gas processes. Again, Binney & Tremaine (2008) is a reference as well as the recent review of Diemand & Moore (2009).

Pure dark matter simulations attempt to follow the formation and evolution of structure in the dark matter fluid, essentially by solving the CBE for the distribution function $f(x, v, t)$. At early times, this can be done analytically using a perturbation approach which, as mentioned, breaks down once the perturbation modes enter the nonlinear regime. The key ingredient in the N-body method is to approximate the distribution function with a discrete sampling of it. These N samples each represent a mass m_i and are referred to as 'particles'. The known distribution function at some high redshift ($z > 30$) is then replaced with the sample of particles. This allows the Newtonian potential to be treated as the potential generated by the particles,

$$
\begin{aligned}
\Phi(x,t) &= -GM \int \mathrm{d}^3 x' \mathrm{d}^3 v' \frac{f(x', v', t)}{|x - x'|} \quad (4.7) \\
&\simeq -\frac{GM}{N} \sum_{i=1}^{N} \frac{f(x, v, t)/f_s(x, v, t)}{|x - x'|},
\end{aligned}
$$

where M is the total mass of the system and $f_s(x, v, t)$ is the sampling distribution chosen to generate the sample of particles. The simplest choice is $f_s(x, v, t) = f(x, v, t)$ but there are more

general schemes as well. The acceleration of each particle is given by the potential, and the particle trajectories can then be advanced a small step Δt forward in time. The size of Δt depends on the size of the accelerations: large accelerations require small time steps in order to track the evolution accurately. The sample of particles represent the distribution function after Δt, and the process can be repeated until the desired redshift (usually $z = 0$) is reached.

This scheme appears straight-forward to implement, but in fact there are several further tricks and approximations that are necessary. In principle, the potential Φ must be calculated at the position of each particle by a Poisson solver algorithm. In practice it is not feasible to calculate the distances needed in eq. (4.7) for a large number of sample particles, since the number of interparticle distances is $\sim N^2$. Different schemes exist which trade a little accuracy with a significant reduction of computational effort by, e.g., interpolating the particle masses onto a mesh, calculating the forces on the mesh nodes, and then interpolating back to the particle positions. With such methods the computational effort can be reduced to scale as $N \ln N$. Another problem arises when two particles come very close to each other and experience very large forces. This is both unphysical, as a side effect of the discretization of the problem, and numerically problematic, as it requires very small time-steps to follow. It is solved by softening the gravitational force at short distances which means that the r^{-1} behavior of the potential is altered for small r so that there is no singularity. For example, Plummer softening replaces r^{-1} with $(r^2 + \varepsilon^2)^{-1/2}$ where the choice of ε sets the scale of the softening.

For these reasons there are certain limitations to N-body simulations. The gravitational softening sets a minimum scale below which the results of the simulation are not reliable, and for halos this means that the centre of the halo cannot be probed. Another discreteness issue is the mass resolution: clearly, (sub-)structures on a mass scale lower than the mass ascribed to the sample particles cannot be resolved in the simulation. Similarly, low-density regions between halos are poorly resolved due to the small number of particles in such volumes, although this is of less importance for halos. In the recent literature, it has become customary to test convergence and resolution by running series of sim-

ulations based on the same algorithms and initial conditions but with increasing number of particles. The results of one simulation can then be gauged against those of its higher resolution sibling.

Finally, it is important to stress two conceptual limitations of cosmological N-body simulations. The simulations require a specified cosmological model, such as ΛCDM, as well as definite values of the cosmological parameters, i.e. the Hubble constant, the matter content, the amplitude of mass fluctuations, etc. Therefore, cosmological simulations are model-dependent by nature. The second issue is that cosmological simulations may provide a solution to the structure formation problem, but they do not explain *why* that solution is realized. Hence, simulations cannot provide a fundamental understanding of the equilibrium and formation of dark matter halos, with or without baryons.

The mass profile

More than ten years ago Navarro, Frenk, and White (NFW) pointed out that the mass profiles of relaxed dark matter halos found in cosmological simulations are similar, irrespective of halo mass or redshift (Navarro et al., 1996, 1997). This universal mass profile was found to be well described by a double power-law with an inner slope of -1 and an outer slope of -3. There is no freedom in the NFW profile except two scaling parameters which fix the mass and the radial extent of the halo. Since then several other functional forms have been proposed and tested against higher resolution numerical simulations, and some of these introduce an extra shape parameter which can vary the shape of the profile. A critical question is whether such a shape parameter is universal or varies from halo to halo. In the latter case, there are several interesting possible relations between the shape parameter and, e.g., halo mass, redshift of last major merger, or the spatial size of the halo.

The NFW profile and a number of other profiles can conveniently be expressed in terms of a general double power law (Hernquist (1990); Zhao (1996)),

$$\rho(r) = \frac{\rho_0}{(r/r_s)^\gamma [1 + (r/r_s)^\alpha]^{(\beta-\gamma)/\alpha}}. \qquad (4.8)$$

The shape of the profiles are specified by the parameters (α, β, γ) which control the width of the transition and the inner and outer logarithmic
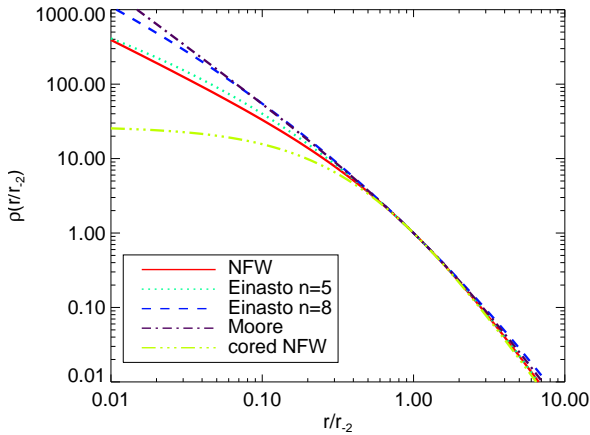
Fig. 4.1: Mass profile as a function of radius in
units of r_{-2}, which is the radius where the
logarithmic slope is -2. The profiles have
been normalized to unity at r_{-2}. For the
cored NFW $\gamma = 0$ in eq. (4.8).

slopes, respectively. The NFW profile is given by
$(1,3,1)$, the Hernquist profile by $(1,4,1)$, and the
Moore profile (Moore et al., 1998) by $(1,3,1.5)$.
Also, Dehnen et al. (2006) used dynamical re-
lations extracted from numerical simulations to
close the Jeans equation and obtain the parame-
ters $([4-2\beta_0]/9, [31-2\beta_0]/9, [7+10\beta_0]/9)$, where
β_0 is the velocity anisotropy at $r = 0$.

For the three-parameter profiles, one immedi-
ately obtains a family of generalized NFW profiles
where one of the (α, β, γ)-parameters is left free to
vary. In light of the limited resolution of simula-
tions in the centre of halos as well as the cusp-core
problem (see section 4.3) a lot of attention has been
given to a varying inner slope, γ. Another three-
parameter profile is the Einasto (or Sérsic) profile
(Einasto, 1969; Sérsic, 1963),

$$\rho(r) = \rho_{-2} \exp\left(-2n\left[\left(\frac{r}{r_{-2}}\right)^{1/n} - 1\right]\right), \quad (4.9)$$

where ρ_{-2} labels the density at the radius r_{-2}, at
which the logarithmic slope of the profile is -2.
The Einasto profile is characterized by a contin-
uous 'roll' and does not asymptote to a power
law at small or large r. This parametrization has
been used extensively as a two-dimensional pro-

file to model surface brightness profiles of galax-
ies (usually then referred to as the Sérsic profile)
and it is itself a generalization of the de Vau-
couleurs' profile (de Vaucouleurs, 1948). The recent
high resolution Aquarius simulations of Milky Way-
sized halos have indicated that the Einasto pro-
file is a better description than any two-paramater
model, including the NFW. The best fit is achieved
with a shape parameter varying from halo to halo
(Navarro et al., 2008). Figure 4.1 shows examples
of some parametrized mass profiles.

The total mass of a halo, whether real or sim-
ulated, is somewhat ambiguous since there is no
boundary in the form of a sharp transition in the
density field. One definition of the boundary is the
'virial radius' r_{vir} within which the halo is virial-
ized, but this radius is not easily determined nei-
ther in numerical simulations nor observationally.
Formally, the virial radius can be defined through
the collapse of a spherical top-hat overdensity in an
Einstein-de Sitter universe (Peebles, 1980) where it
turns out to be the radius enclosing a mass with
mean overdensity $\Delta_{\text{vir}} = 18\pi^2 \approx 178$, compared to
the mean matter density, i.e.,

$$M_{\text{vir}} = \frac{4\pi r_{\text{vir}}^3}{3} \Delta \rho_m. \quad (4.10)$$

With this definition, however, r_{vir} depends on both
cosmology and redshift (Bryan & Norman, 1998).
Alternatively, one may just define an overdensity
which forms the basis for comparison of different
halo masses. It is common to take $\Delta = 200$ with
respect to either the critical density or the mean
matter density. The radius defined in this way is
labeled r_{200}, but it is often referred to, nonetheless,
as the virial radius. This is a convenient definition
of the extent of a halo in numerical simulations as
it does not involve any physical properties of the
individual halo. A related parameter is the concen-
tration, $c_{200} = r_{200}/r_s$ which is weakly correlated
with the cluster mass (see below).

Simulations now probe not only the mass dis-
tribution of the primary halo but also that con-
tained in substructures, which are halos that have
been accreted but are cold enough to survive tidal
disruption (Springel et al., 2008a; Diemand et al.,
2008). The abundance of substructures can be
compared with the observed number of Milky Way
satellites. Several hundreds of subhalos are pre-
dicted by simulations whereas traditionally only 11

satellites were known. This discrepancy has been referred to as the satellite abundance problem of ΛCDM. However, on one hand 14 new satellites have been discovered in the ∼ 20% of the sky observed by the Sloan Digital Sky Survey (Adelman-McCarthy et al., 2008; Tollerud et al., 2008), and on the other the understanding of star formation and the detectability of these very small halos has improved (Kravtsov et al., 2004; Koposov et al., 2008; Maccio' et al., 2009). Thus, it now seems there is no strong disagreement between observations and expectations.

Substructures potentially play an important part for indirect detection of annihilating dark matter. Several of the known satellites are located in low gamma-ray background regions of the sky, whereas a possible annihilation signal from the main Milky Way halo peaks in the complex background of the Galactic centre. Predictions of the annihilation signal have been made both based on numerical simulations (Kuhlen et al., 2008, 2009; Springel et al., 2008b) and on the observed satellites (Strigari et al., 2008). These predictions are of course particularly pertinent with FERMI taking data. It should perhaps be kept in mind that the observed mass profiles of spiral galaxies such as the Milky Way are often found to be more cored than those of simulated Milky Way-sized halos. Hence the annihilation signal from the main halo may not be as strong as predicted. Likewise, while the number of Milky Way satellites does not appear to be in strong disagreement with simulations anymore, there is a long way to go before the observations can be said to confirm the predicted abundance, and so there is also considerable uncertainty in this respect. If FERMI detects an annihilation signal this would provide a very interesting test of the numerical predictions.

The dynamical structure

The dynamical structure of simulated dark matter halos has received somewhat less attention than the mass profile, largely because it is not immediately accessible in observations. However, the dynamical structure in the solar neighborhood plays a very important role for direct detection experiments. Dynamical structure can also provide clues about the fundamental nature of halo physics. Roughly speaking, there are two parts to the dy-
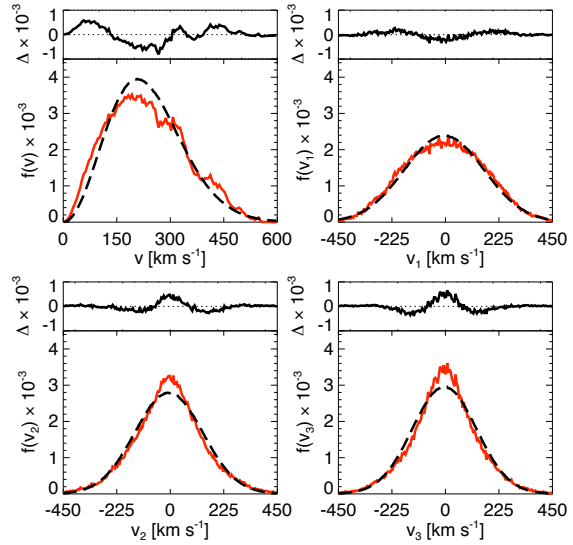

Fig. 4.2: The velocity distribution in the vicinity of the Sun in a Milky Way-sized halo. Upper left: speed distribution, others: components along the axes of σ_{ij}. The red curves are the actual distributions and the black dashed curves are Gaussian fits. Figure from Vogelsberger et al. (2009).

namical structure: the angular momentum distribution, which has been shown to be universal (Bullock et al., 2001a), and the velocity dispersion tensor which enters the Jeans equation. I will focus on the latter.

Just as the mass distribution, the velocity dispersion tensor is usually analyzed in spherically averaged radial bins. The only freedom, in principle, is the total velocity dispersion and the velocity anisotropy β, both as functions of radius. However, local substructure or tidal effects can complicate this idealization. The velocity dispersion and anisotropy are very sensitive to discreteness effects since a) there may be a non-zero mean velocity in a bin (which can be physical, e.g. caused by substructure, or it may be a discreteness issue), and b) as a second moment, it is quite sensitive to particles which are outliers in the velocity distribution.

Figure 4.2 shows the dark matter velocity distribution at the radius of the solar orbit in a simulated halo similar to the Milky Way. Compared to
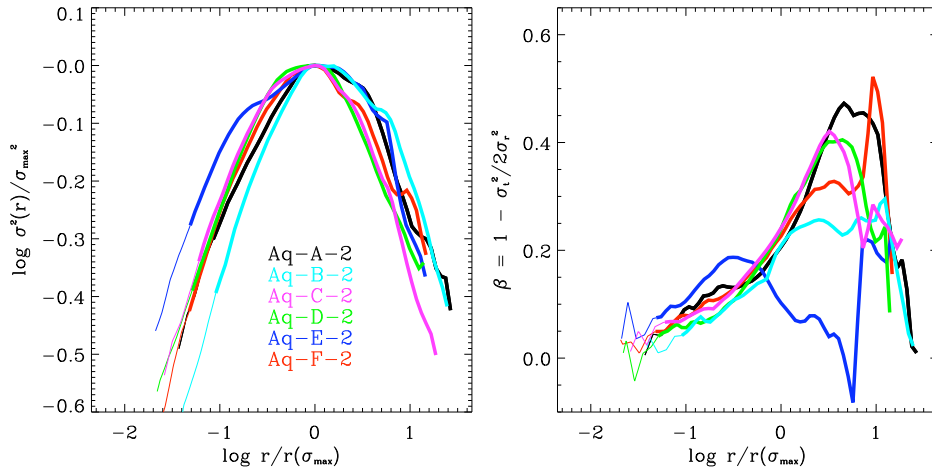
Fig. 4.3: Velocity dispersion (left) and velocity anisotropy (right) for the six Milky Way-sized halos of the Aquarius simulations (from Navarro et al., 2008).

a Maxwell-Boltzmann distribution, it is clear that the radial component v_1 has a more 'boxy' shape (kurtosis < 0) while the tangential components v_2 and v_3 have more 'spiky' shapes (kurtosis > 0). This behavior holds within r_{-2}, but it is opposite in the outer parts (Wojtak et al., 2008a). The velocity distribution is better approximated by a Tsallis-type generalization of the Maxwell-Boltzmann distribution (Hansen et al., 2006).

The dispersion profile σ^2 is found to increase slightly with radius until r_{-2}, where it reaches its maximum, and then it declines gradually. The left panel of figure 4.3 shows the total velocity dispersion for the six halos of the Aquarius project, rescaled to the radius of the peak dispersion $\sigma^2_{\max}$. The logarithmic slope of the profile is about 0.4 in the region interior to $\sigma^2_{\max}$ and -0.4 outside. The radius corresponding to the peak velocity dispersion coincides with r_{-2} and the virial radius is about one magnitude larger than this, with some halo-dependent scatter. The right panel shows the velocity anisotropy profile which increases slowly from a near-isotropic level in the central regions to reach a radial bias in the outer regions. Clearly, collisionless structures have a more complicated stress tensor than collisional gases. A linear relation has been identified between the velocity anisotropy and the logarithmic slope of the density profile $\mathrm{d}\ln\rho/\mathrm{d}\ln r$ (Hansen & Moore, 2006; Hansen &

Stadel, 2006), shown in figure 4.4. This has been confirmed to hold within r_{-2} in the Aquarius simulations.

Another quantity that has drawn considerable attention is the combination of the density profile and the velocity dispersion profile in the form ρ/σ^3, termed the pseudo-phase space density. As can be seen in figure 4.5, this has been found to be well described by a *single* power law $r^{-\chi}$ with $\chi \approx 1.875$ (Taylor & Navarro, 2001), despite the more complex radial dependences of both the density and velocity disperison profiles. This has been connected to the self-similar solution to radial infall onto a point mass in an Einstein-de Sitter universe, as found by Bertschinger (1985). It is not quite clear if the power law behavior is more consistent with ρ/σ^3 or ρ/σ_r^3, but in any case the pseudo-phase space density appears to be a strong candidate for a universal trait of dark matter halos. The phase space density profile is also sensitive to substructure in the outer parts (Stadel et al., 2009). The simple power law behavior of ρ/σ_r^3 was combined with the velocity anisotropy–density slope relation by Dehnen & McLaughlin (2005) who found a single physically viable solution, $\chi = 35/18 \approx 1.94$ (see also Austin et al., 2005), which determines all the terms in the Jeans equation up to a free parameter $\beta(r = 0)$.

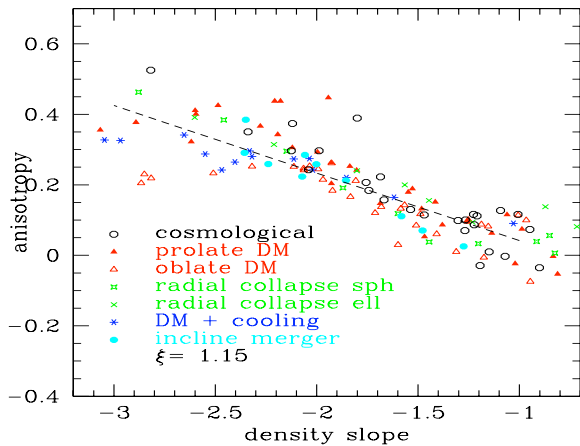If the mass profile of relaxed dark matter

Fig. 4.4: The density slope–velocity anisotropy relation, which appears not only in cosmological simulations but also in various toy models. Figure from Hansen & Moore (2006).

Fig. 4.5: Pseudo-phase space density profiles ρ/σ^3 of the six Aquarius halos. The near-power law behavior is evident. The lower panels show the residuals from the $r^{-1.875}$ profile and from the best fitting free slope power law. The best fitting slopes are in the range -1.86 to -1.92. Figure from Navarro et al. (2008).

structures is near-universal and the pseudo-phase space density is described by a simple power law, the velocity dispersion profile and the velocity anisotropy must also be near-universal. However, the anisotropy profiles in figure 4.3 appear to be only qualitatively rather than quantitatively similar. This apparent contradiction can be caused by slight disturbances of the halos, or it may be connected to the fact that halos are actually triaxial (e.g., Dubinski & Carlberg, 1991; Novak et al., 2006; Stadel et al., 2009) with typical axis ratios as low as 0.5. The errors induced by the spherical binning of the N-body particles may then be responsible for the variation of the anisotropy profile at large radii.[1]

Statistical properties

Not only the properties of individual halos can be predicted by cosmological numerical simulations, the ensemble of halos in a large simulation can also be investigated to reveal clues about the physics of

structure formation. One example, the halo mass function, was already discussed in section 2.2.

The concentration of the NFW profile is defined as $c_{200} = r_{200}/r_s$ but this can easily be generalized to the model independent $c_{200} = r_{200}/r_{-2}$. This parameter measures the scale of the 'roll' of the mass profile compared to the virial radius. The concentration has been found to be negatively correlated with the virial mass of the halo (Navarro et al., 1996, 1997) although there is appreciable intrinsic scatter about the mean relation. This behavior can easily be understood in terms of the hierarchical formation of structure in the ΛCDM cosmology: small halos are the first to form and they do so in the higher density environment of the high-redshift universe. Hence their central densities are greater and the density contrast compared to the background, i.e. the concentration, is larger. The normalization of the mass–concentration rela-

---

[1] It may also be suspected that three-parameter mass profiles such as the Einasto profile will never be truly universal, since similar halos with different axis ratios could then also have different shape parameters in the spherical approximation.
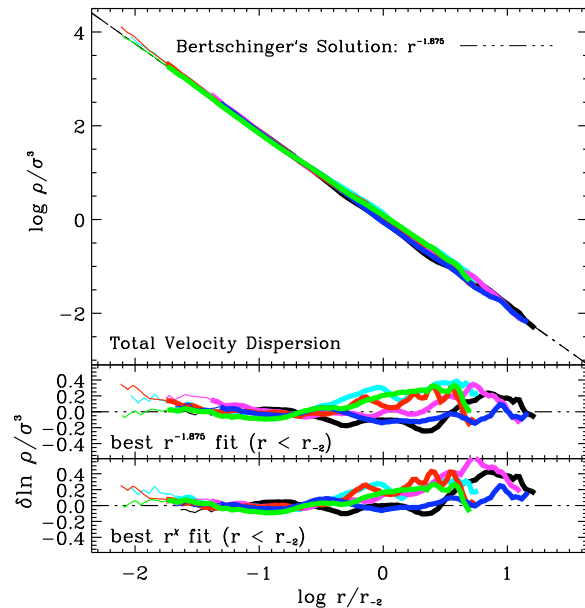
tion is quite sensitive to the cosmology, particularly to the amplitude of mass fluctuations, σ_8 (Neto et al., 2007; Macciò et al., 2008). The concentration is also correlated with redshift, which means that galaxies in the early universe were more extended and hence likely to have lower surface brightness, compared to a $z = 0$ galaxy of similar mass (Bullock et al., 2001b).

Baryonic effects

A major problem when confronting the results of high-resolution cosmological simulations with observations is the uncertain properties and effects of the baryonic component. Baryonic effects can steepen the inner slope of the dark matter profile by adiabatic contraction, where the dissipative clustering of baryons steepens the inner slope (e.g. Gnedin et al., 2004). The inner slope can also be affected by black holes, formed either through accretion, which yields a steepening of the profile in the same way as adiabatic contraction, or through mergers, which can energize the dark matter so it forms a constant density core (Merritt et al., 2002).

The missing baryonic effects can be alleviated for example by putting additional gas particles, subject to hydrodynamic forces as well as gravitational, into the N-body simulations in a scheme known as smoothed particle hydrodynamics (Monaghan, 1992; Springel & Hernquist, 2002). The gas particles are associated with a pressure and an entropy, and the pressure yields an extra term in the equation of motion. Additionally, an artificial viscosity term is introduced in order for the gas to be able to increase its entropy and dissipate energy. More advanced schemes include models for radiative cooling of the gas particles and complex processes such as star formation and reheating due to feedback. Still, the models are very simplified and involve a degree of tuning in order to obtain realistic results. The effort required to track the additional properties of gas particles means that they are computationally much more expensive to simulate than pure dark matter, and the spatial resolution and mass resolution are considerably reduced for a given computing time. Thus, cosmological hydrodynamical simulations are not yet at the level where they can probe the impact on the dark matter halo mass profile and dynamics reliably, particularly not in the centre, but they provide extremely valuable benchmarks

for direct comparison with x-ray observations including estimates of the non-thermal pressure (Valdarnini, 2006; Nagai et al., 2007).

Another approach to modeling baryons are semi-analytical models which combine an approximate analytical description of baryonic physics with N-body simulations of dark matter (e.g. Croton et al., 2006). The crucial information from the simulations is the halo merger tree, which specifies how structure is built up of hierarchical mergers of smaller halos. Each halo is assumed to contain a Universal baryon fraction which is subject to external UV radiation, radiative cooling, star formation, AGN and supernova feedback processes, etc. The final step is a model of the luminosities and spectra of the halo galaxies which facilitates direct comparison with observations. Again, the results are quite model-dependent and the various schemes used in the literature are still being optimized. Compared to the SPH approach, the semi-analytical models do not degrade the resolution of the N-body simulation, and it is possible to try different semi-analytical models on the same simulations, as the baryonic modeling is done entirely post-simulation. On the other hand, the effect of baryons on the dark matter halo itself can only be estimated coarsely and the semi-analytical models must in general be tuned by results from hydrodynamical simulations.

4.3   Observational probes

The same types of observations that reveal the need for dark matter in galaxies and galaxy clusters can also be used to probe the properties of dark matter halos. For galaxies the most important source of data is stellar kinematics while for clusters both gravitational lensing and x-ray observations of the hot gas in the intra-cluster medium provide valuable data. Again, a general reference is the textbook of Dodelson (2003) and, for clusters, the review of Sarazin (1986).

Kinematical data

As discussed earlier, the line-of-sight velocities of stars in galaxies can be measured from their redshifts. In ellipticals or dwarf galaxies, where there is no significant ordered motion, the stars can (to lowest order) be described by the Jeans equation
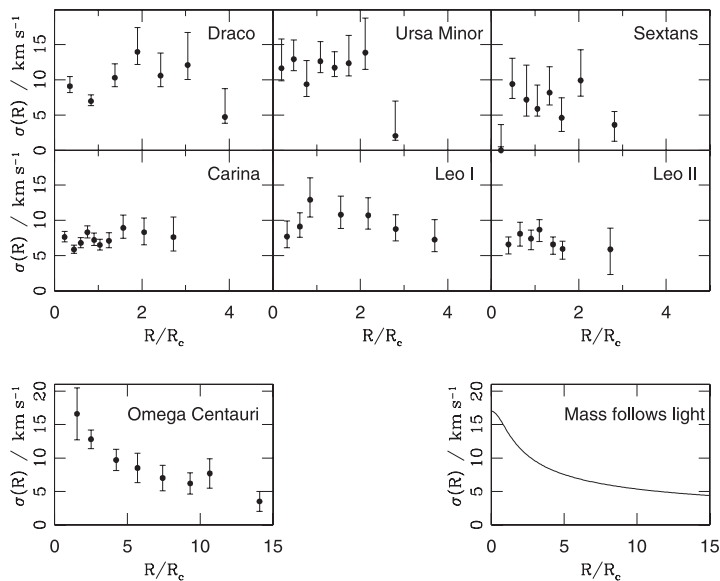
Fig. 4.6: Line-of-sight velocity dispersions of six dwarf spheroidals, as well as the globular cluster Omega Centauri, and the velocity dispersion profile of a model in which mass follows light. The model is in good agreement with the globular cluster, but not with the dSphs. Figure from Gilmore et al. (2007).

(4.6), while in spiral galaxies the rotation is simply related to the mass as $v_c^2 = GM(r)/r$.

The Milky Way satellites are dwarf spheroidal galaxies with luminosities $\sim 10^6 L_\odot$. They are the most dark matter-dominated systems known with observed line-of-sight velocity dispersions $\sigma_{\rm los} \sim 10\,{\rm km s}^{-1}$, which imply mass-to-light ratios in the range of tens or even hundreds in solar units. The measured $\sigma_{\rm los}$ is usually found to be roughly constant with radius. Figure 4.6 shows examples of the measured velocity dispersion profiles of dSphs as well as that of a globular cluster with similar luminosity. For globular clusters, which are not believed to contain any dark matter, the dispersion profile can be explained by the stellar mass but this is not the case for the dSph profiles. The line–of–sight velocity dispersion is formally a moment of the distribution function integrated along the line–of–sight. For this reason a major problem in the modeling of these systems is the unknown velocity anisotropy profile of the stars $\beta_\star(r)$, which is partially degenerate with the total mass profile. Even so, a cored mass profile with constant density in the central regions is preferred by the data

although a tangentially biased cuspy NFW profile is also a possibility (Gilmore et al., 2007; Walker et al., 2009). In a few cases the presence of old substructures have been argued to imply a cored profile, since the substructures ought to have been tidally disrupted in a cuspy profile (Kleyna et al., 2003; Goerdt et al., 2006). The presence of a core is also supported by recent more advanced modeling based on thousands of stellar velocities (Gilmore, 2009). Dwarf spirals are also better described by a cored mass profile than by a cuspy one (e.g. van Eymeren et al., 2009).

The shape of the rotation curve of larger spiral galaxies is also a probe of the mass distribution in the halo. The shape of the total mass profile seems to be mass-dependent (Kirillov & Turaev, 2006; Salucci et al., 2007). As the dSphs, the spiral rotation curves prefer a cored mass profile over a cuspy one. However, spirals are much more efficient at forming stars than either dwarf galaxies or clusters, so baryonic effects that may affect the dark matter distribution are expected to be strong (Conroy & Wechsler, 2009). Secondly, the spiral disk itself is difficult to build in numerical simu-

lations with baryons and so the nature of baryonic effects is not well understood in this context. There are also indications that the spectral analysis may be affected by systematics (Spekkens et al., 2005).

Kinematic analyses are also applied to the motion of galaxies in clusters, but in this case there is again the partial degeneracy between the velocity anisotropy of the galaxies and the mass profile (but see Łokas & Mamon, 2003). Therefore x-ray and lensing observations are better probes of clusters.

Gravitational lensing

Gravitational lensing probes the total mass distribution along the line of sight, independent of the type of matter that exerts the gravitational pull. Light emitted by a background source is deflected by any mass located between the source and the observer. A source located at the true position on the sky β is observed at a position θ, which is given by the solution of the lens equation (see, e.g., Schneider, 2006),

$$\beta = \theta - \frac{1}{\pi} \int \mathrm{d}^2\theta' \kappa(\theta') \frac{\theta - \theta'}{|\theta - \theta'|^2}. \qquad (4.11)$$

Here, $\kappa(\theta)$ is the surface mass density of the lensing objects. If there are multiple images (or arcs) of the same background object, there is more than one β that solves the lens equation This is the strong lensing regime already mentioned. Whether this is the case depends both on the strength of the lens and on the redshifts, i.e. the geometrical configuration, of the lens and the source. Several galaxy clusters are strong lenses and various methods, both parametric and non-parametric, have been developed to infer the lensing potential by matching the observed images and arcs to that produced by model potentials. This allows a mapping of the central parts of clusters. In the other case, weak lensing, there is only one solution to the lens equation and hence only one image is observed. This image will in general be magnified and distorted in shape. Whether this is the case for a single source is impossible to determine, but the field of background galaxies will be distorted in a coherent fashion. Therefore the lensing potential can be determined from the statistics of the ellipticities of background galaxies, which allows a mapping of the potential in the outer parts of a galaxy cluster.
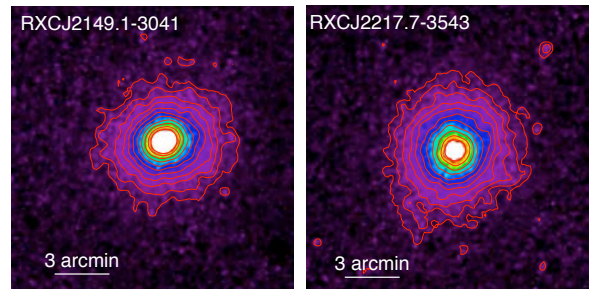

Fig. 4.7: X-ray emission from the clusters Abell 1384 (left) and Abell 3854 (right). Figure from Pratt et al. (2009).

X-rays

The spaceborn X-ray observatories *XMM-Newton* and *Chandra* allow observations of the intra-cluster medium (ICM) with unprecedented spatial resolution. From such observations, the radial profile of both the temperature and the density of the ICM can be obtained. Typically, the temperature profile can be obtained by spectral fitting in ~ 10 radial bins over more than a decade in radius. The density profile can be obtained from spectral fitting as well, but also directly from the flux with much higher spatial resolution. In order to probe the gravitational potential, the thermal gas pressure is assumed to provide the support against gravitational collapse which leads to the equation of hydrostatic equilibrium,

$$\frac{GM(r)}{r} = -\frac{k_B T}{\mu m_H} \left(\frac{\mathrm{d}\ln n_e}{\mathrm{d}\ln r} + \frac{\mathrm{d}\ln T}{\mathrm{d}\ln r} \right). \qquad (4.12)$$

Here, n_e is the number density of electrons in the ionized ICM, and $\mu = 0.6$ is the mean molecular weight of the ICM. If there are significant bulk flows in the gas, additional terms of the form $(\vec{v} \cdot \nabla)\vec{v} - (v_\theta^2 + v_\phi^2)/r$ appear on the right-hand-side of eq. (4.12), but this is usually not a major issue for systems that appear relaxed (Piffaretti & Valdarnini, 2008; Lau et al., 2009). The spherical approximation is often surprisingly good as can be seen in figure 4.7.

An important problem in the x-ray analysis is the step from 2D projected profiles to 3D deprojected profiles which, even assuming spherical symmetry, is not trivial. One type of solution

involves parametrized 3D models for the density and temperature profiles which are projected onto the sky analytically or numerically and then fitted to the observations. If one is more interested in the properties of the ICM, a variation of this method parametrizes the total mass profile instead (e.g., with an NFW profile), and leaves the deprojected temperature profile to be determined through eq. (4.12). Another option, sometimes referred to as 'onion-peeling', involves the stepwise subtraction of the contribution of outer bins to the projected signal from further in. This method is less model-dependent as it can be done without parametrizing the density and temperature profiles. However, it is susceptible to spikes or outliers in the 2D profiles which induce an oscillatory behavior in the 3D profiles.

The contribution from the individual galaxies to the total mass profile is negligible, except in the centre of clusters, and so the ICM density profile and the total mass profile obtained through eq. (4.12) allow the dark matter density profile to be determined. In general, the NFW profile has been found to be in good agreement with observations, but often the data only support fits over a limited radial range and so the Hernquist profile, or in some cases even simple power laws, can also be adequate descriptions. On the other hand, the steeper cusp of the Moore profile has often been found to be in tension with the observations. Unfortunately, the x-ray observations have difficulties in probing the centre well enough to determine if the power law slope becomes less steep than in the NFW case. This is due to a combination of spatial resolution, the uncertainty of the stellar contribution in the centre, and the very small mass contained there. Part of Paper III is an investigation of observational constraints on the inner slope.

Predictions vs. observations

So what is the status between the predictions of numerical simulations on one hand and the observational results on the other?

For the mass profile, the benchmark for comparison has been the NFW profile. As already hinted at, the kinematics of dwarf galaxies and spiral galaxies prefer a profile with a more shallow inner slope than the NFW, although the modeling means there is some uncertainty. This core-

cusp problem could be solved by warm dark matter such as keV-scale sterile neutrinos. Warm dark matter is slightly relativistic at decoupling and it leads to a suppression of the matter power spectrum on smaller scales than hot dark matter. The free streaming could eradicate the cusps predicted by numerical simulations.

On larger scales, several studies of galaxy clusters have found the NFW profile to be in good agreement with both strong and weak lensing observations (Broadhurst et al., 2005; Comerford et al., 2006; Limousin et al., 2008), although there are also claims of a less steep central density profile (Sand et al., 2004). X-ray studies of galaxy clusters also find varying inner slopes but this may be a real effect or scatter (observationally induced or perhaps intrinsic) around the NFW cusp (Ettori et al., 2002; Lewis et al., 2003; Zappacosta et al., 2006; Saha & Read, 2009). There has also been several joint analyses of clusters using both x-rays and lensing which do not always find agreement on the mass distribution (Loeb & Mao, 1994; Mahdavi et al., 2007; Miralda-Escude & Babul, 1995; Zhang et al., 2008; Riemer-Sørensen et al., 2009). Disagreement is usually ascribed to deviations from spherical symmetry or non-thermal pressures which bias the x-ray analysis, but the lensing studies may also be contaminated by the presence of additional mass concentrations along the line of sight. Targets for strong lensing are often perturbed systems with significant amounts of substructure which are more attractive to model because they produce several lensing arcs, but such systems cannot be expected to be in hydrostatic equilibrium so an x-ray mass model will likely not be accurate. Observations, particularly lensing, also tend to prefer a high normalization for the concentration–mass relation (Buote et al., 2007; Gastaldello et al., 2007; Broadhurst et al., 2008) (but see Paper III), although the negative correlation between c and M, as predicted by ΛCDM, is observed at very high significance.

The dynamical structure of dark matter halos is not well studied observationally due to the difficulty of making robust measurements of quantities which are not immediately observable. Ikebe et al. (2004) found that the specific energy of dark matter $\sim \sigma_{\rm DM}^2$ was always smaller than that of the ICM, however they assumed a vanishing dark matter velocity anisotropy in clear disagreement with numerical simulations. Then, Hansen & Piffaretti (2007)

instead assumed equipartition of the specific ener-
gies in two cool core clusters and solved the Jeans
equation for the velocity anisotropy, which was as-
sumed to be constant. They found β to be nonzero
at $\sim 3\sigma$, with best-fitting values of 0.4 and 0.6 for
the two clusters (Paper II is an improvement and
extension of this work). More effort has gone to-
wards determining the dynamical strucuture of the
galaxy population in clusters where the line-of-sight
velocity dispersion can be measured directly (e.g.,
Natarajan & Kneib, 1996; Lemze et al., 2009).

5. SUMMARY & DISCUSSION OF PAPER I-III

In this section I summarize the purposes and results of Paper I-III within the observational and theoretical context of the previous sections. A few select figures from the papers are also included here, but the reader is referred to the appendices for the detailed analysis, results, and discussion of each paper, as well as full references.

5.1 Paper I: Host & Hansen (2007)

What it takes to measure a fundamental difference between dark matter and baryons: the halo velocity anisotropy

In this paper we determine whether the dark matter velocity anisotropy β can be measured in a direction-sensitive dark matter detector.

The signal rate in direct detection experiments, eq. (3.2), can be divided into two parts, one which is determined by the particle physics nature of dark matter, and one which depends on the properties of the Galactic dark matter halo. After a first detection of WIMPs has been established by direct searches, the next goal is to measure these two parts, i.e. to determine the couplings of the WIMP and put these into a theoretical context, and to measure the spectrum and direction of the WIMPs. For the latter purpose, a direction-sensitive detector is needed.

The detection rate depends on two properties of the halo, namely the local density of dark matter ρ_0 and the local velocity distribution $f(\vec{v})$. The local density is degenerate with the nuclear scattering cross section, but it can be inferred if the cross section is measured in collider experiments or fixed by the underlying theory. There is the possibility that local substructure or tidal streams may cause an unusual signal, but the more likely scenario is that the measured event distribution is representative of the Milky Way halo. As discussed in section 4.1, even though the halo dark matter is in the classical regime, there is no reason to expect that the velocity distribution is Maxwellian. In fact, numerical simulations show that the dark matter velocity distribution shape varies with radius, and that the velocity dispersion tensor σ_{ij}^2 is expected to be anisotropic in a halo. Figure 4.2 shows the three components of the dark matter velocity distribution and the speed distribution in a simulated Milky Way-sized halo at the orbit of the Sun. There is a clear difference in the shape of the radial and the two tangential distributions. The velocity anisotropy parameter,

$$\beta = 1 - \frac{\sigma_t^2}{\sigma_r^2}, \tag{5.1}$$

is typically found to be in the range $0.1 - 0.3$ at the solar orbit. The purpose of Paper I is to investigate whether such an anisotropy is measurable in a direction-sensitive direct detection experiment.

We only consider coherent spin-independent scattering, and we take a model-independent approach in the sense that we do not consider a particular combination of detector mass and WIMP. Instead we ask how many events are required to measure the velocity distribution with a given accuracy. We assume the most simple Galactic dark matter velocity distribution that allows for a velocity anisotropy, which is a multi-variate Maxwellian,

$$f(\vec{v}) \propto \exp\left(-\frac{v_r^2}{2\sigma_r^2} - \frac{v_\theta^2 + v_\phi^2}{2\sigma_t^2}\right). \tag{5.2}$$

Even if the Maxwell-Boltzmann distribution is not necessarily a perfect representation of the velocity components distributions, it is likely a reasonable approximation, and it has the clear advantage that it does not require extra parameters to be fixed either by hand or measured from the data. Events, i.e. random Monte Carlo samples, are drawn from this velocity distribution and they are then transformed to the laboratory frame, which is moving with respect to the Galactic frame with a speed $\vec{v}_\odot + \vec{v}_\oplus(t)$. We scatter the events at random points
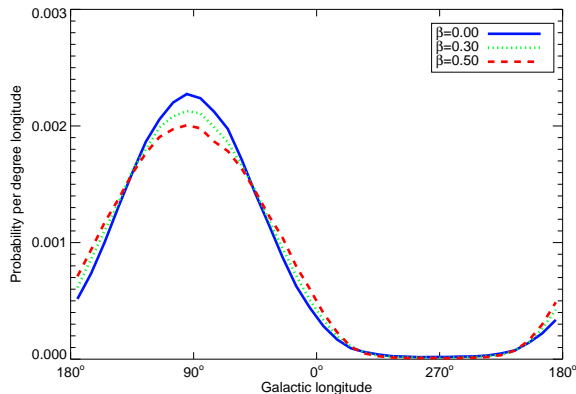
Fig. 5.1: The longitudinal distribution of nuclear recoils induced by dark matter for three different values of the velocity anisotropy β. The motion of the Sun is towards $90°$ longitude, and the β-dependence of the distribution leads to an asymmetry between the number of events from the forwards- and backwards directions. We use this asymmetry as the observable signature of β.

Fig. 5.2: The sensitivity to the velocity anisotropy, i.e. the predicted measurement uncertainty, σ_β for varying threshold energy and acceptance angle. The shape of these curves are general, but the actual value of σ_β is model-dependent, see the text for details. A large number of events, 3×10^4 for a $100\,\text{keV}$ threshold energy, are required to reach the sensitivity shown in this figure.

of the sidereal year. We simulate the momentum-dependent nuclear scattering with the standard Helm form factor. This determines the scattering angle and the nuclear recoil for each event. We model the limited angular resolution of a realistic detector by the Fisher distribution, the spherical analogy to a Gaussian. This, finally, represents the measured nuclear recoil. We can vary the detector-dependent angular resolution, which gives the dispersion of the Fisher distribution, and the detection threshold, which determines if a given event is actually measured. We consider a number of realistic values for both.

We find that the velocity anisotropy has a very simple observational signature in the number of nuclear recoils which are measured to arrive from the forwards hemisphere (defined by the solar motion), relative to the number from the backwards. The variation of this 'forwards–backwards' asymmetry is shown in figure 5.1. We use this asymmetry within a defined solid angle (the acceptance region) as an estimator for the velocity anisotropy. Then we consider how accurately the velocity anisotropy
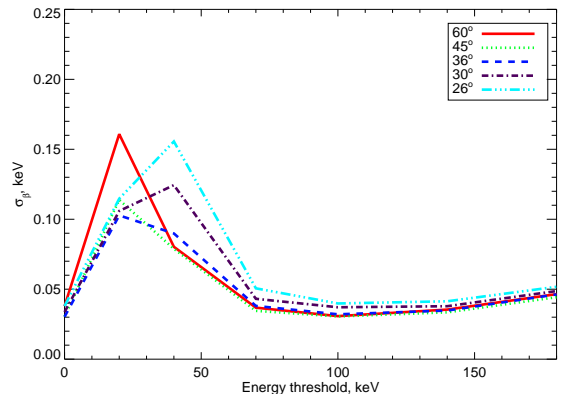
can be measured under given circumstances. As a fiducial model we consider a conservative value for the anisotropy, $\beta = 0.1$, perfect angular resolution, a WIMP mass of $100\,\text{GeV}$, and a ^{32}S target nucleus (as used in the DRIFT TPC design). The asymmetry increases with β for small detection thresholds, but this trend reverses around $E_{\text{thr}} \approx 40\,\text{keV}$. We do not assume an accurate energy reconstruction and therefore a relatively high energy threshold is not necessarily a disadvantage.

The variance σ_β of the simulated detections is shown in figure 5.2 for the fiducial model for 10^6 events. The optimal scenario with $E_{\text{thr}} = 100\,\text{keV}$ yields a sensitivity of $\sigma_\beta = 0.03$, corresponding to a better than 3σ detection of a non-zero velocity anisotropy. Only about 3% of all events pass this energy threshold, but for lower thresholds the turnover of the asymmetry–anisotropy correlation means that the sensitivity is degraded.

We can then investigate the effects of the various parameters. For example, the sensitivity depends on the number of events roughly as $1/\sqrt{N}$, as might be expected, while a limited angular resolution of $30°$ degrades the sensitivity by about 30%. An

isotropic background, which adds events to both the forwards and the backwards acceptance region, with a level of 25% of the WIMP signal increases σ_β by about 25%.

However, the main result is that it will take a very large number of events to make a statistically significant measurement of a non-zero velocity anisotropy, if $\beta \approx 0.1$. For comparison, the enormous DAMA/LIBRA exposure of 0.53 t-yr resulted in 2×10^5 events, of which only a fraction may be WIMPs causing the observed annual modulation. For a direction-sensitive detector, this number of events is far into the future. For this reason we did not go into a more detailed analysis, but we expect a somewhat improved sensitivity if the recoil energy can be measured. There will likely be a non-trivial detector-specific energy dependence of both the spectral and the angular resolution. Our results are largely unchanged if WIMPs are primarily detected through spin-dependent interactions, since the WIMP distribution does not probe the strongly varying high-momentum transfer part of the nuclear form factor.

It is not clear whether there are other halo properties that can generate a varying forwards–backwards asymmetry. There are, of course, many possible parametrizations of the velocity distribution and the anisotropy signature might vary slightly between these models. Constraining the shape of the velocity distribution will, however, be much more difficult. A local disturbance of the velocity field, even if subdominant, might also cause an ambiguous signal.

5.2 Paper II: Host et al. (2009)

Measurement of the dark matter velocity anisotropy in galaxy clusters

In this paper we make a first measurement of the dark matter velocity anisotropy profile, based on x-ray observations of 16 galaxy clusters.

As discussed in section 4.3, satellite x-ray telescopes such as *Chandra* and *XMM-Newton* allow high-resolution observations of the hot, ionized ICM. It is possible to determine the radial temperature and density profiles, $T(r)$ and $n_e(r)$, through a spectral deprojection analysis, and the data we use here consists of the deprojected temperature and
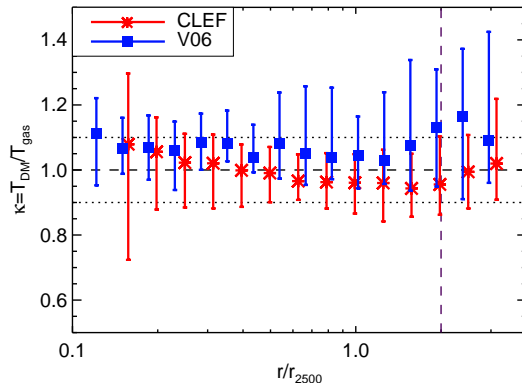

Fig. 5.3: The ratio of the specific energies of the ICM and dark matter for two ensemble of relaxed cluster-halos found in the CLEF and V06 cosmological SPH simulations. The fact that this ratio is close to unity is used as an extra constraint in the analysis, which allows us to close the Jeans equation and determine the velocity anisotropy $\beta(r)$.

density profiles, with uncertainties, in six or seven radial bins for each of the 16 clusters. All profiles were deprojected without assuming parametrized models for either the density or the temperature.

The use of x-ray observations to measure the mass distribution in galaxy clusters based on hydrostatic equilibrium has become standard in the literature. The dark matter density profile can also be inferred as the difference between the total density and the measured ICM density. This still leaves two degrees of freedom in the Jeans equation (4.6),

$$\sigma_r^2 \left(\frac{\mathrm{d}\ln\rho}{\mathrm{d}\ln r} + \frac{\mathrm{d}\ln\sigma_r^2}{\mathrm{d}\ln r} + 2\beta \right) = -\frac{GM(r)}{r}.$$

In order to close the Jeans equation, we make an additional assumption that the specific energy of dark matter tracks the specific thermal energy of the ICM, i.e. the temperature. This assumption is inspired by the results of two cosmological radiative SPH simulations of the formation of structure. Figure 5.3 shows the ratio κ of the specific energies for the most relaxed halos found in each simulation (67 for CLEF, 20 for V06). Clearly, the specific energies are close to equal. The two simulations are
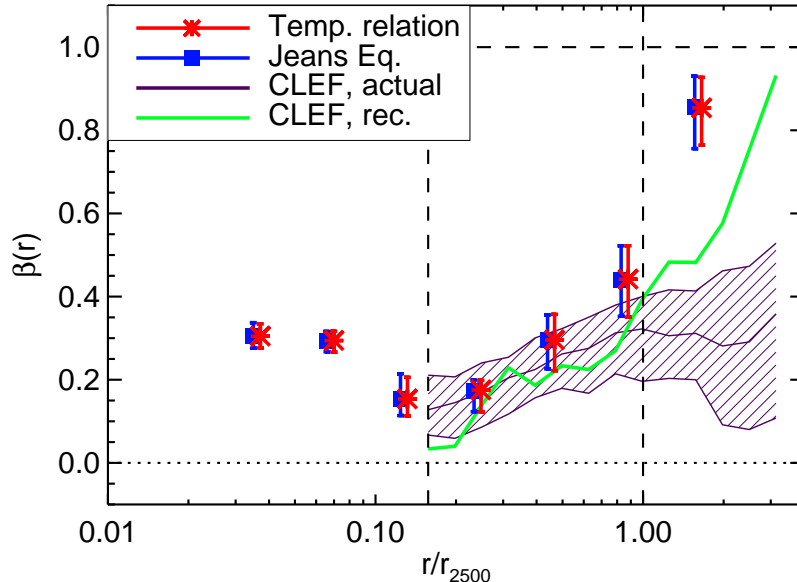
Fig. 5.4: The stacked measured velocity anisotropy profile $\beta(r)$ for all 16 clusters. There are two different, but not independent, ways of finding β from the observations. The dashed line shows the anisotropy profile for the 67 halos in the CLEF simulations, and the green line is the median anisotropy recovered by our method for those simulated halos. The measured β-profile is in good agreement with CLEF at intermediate radii, while it is overestimated outside r_{2500} due to a lack of hydrostatic support. The relatively large anisotropy interior to $0.1\,r_{2500}$ is somewhat unexpected, see text for details.

completely independent and based on two different numerical codes. By fixing $\kappa(r)$, it is possible to solve the Jeans equation to find $\sigma_r^2(r)$ and $\beta(r)$ from the measured $T(r)$ and $n_e(r)$.

The anisotropy-profiles of the individual clusters are found to be qualitatively similar, but they show some scatter and in some cases quite large uncertainties. Hence, we also consider the sample-averaged velocity anisotropy profile, shown in figure 5.4. At intermediate radii we find a slowly increasing radial bias in the range $0.1-0.5$, as predicted by numerical simulations. At radii greater than r_{2500} we measure a very large anisotropy parameter of ~ 0.8. We believe this is an overestimate due to a lack of hydrostatic support of the gas in the outer parts of the clusters, as demonstrated by testing our method on the simulated halos. Towards the centre we find a slight, but significant, increase of β to 0.3. This is somewhat surprising since the

anisotropy parameter is expected to approach zero in the centre according to higher resolution pure dark matter simulations (e.g. figure 4.3). The increase takes place in a region which is smaller than the spatial resolution of the hydrodynamical simulations so we do not have a handle on the value of κ. However, the increase of β persists even if we assume different sensible κ-profiles with $\kappa \neq 0$ in the centre.

The measurement of a non-zero velocity anisotropy implies that dark matter is effectively collisionless in galaxy clusters. We can put an order–of–magnitude upper limit on the self-scattering cross section per unit mass, $\sigma/m \lesssim 1\,\mathrm{cm}^2\mathrm{g}^{-1}$. This value is derived from the typical densities in the intermediate radial range where we observe good agreement with simulations. If we take the central densities instead, the upper limit improves by one magnitude. The present result is

very close to ruling out the self-interacting dark matter model (Spergel & Steinhardt, 2000), introduced to explain the core–cusp problem.

After publication of Paper II we investigated whether the presence of large cD-galaxies in the centres of the clusters could account for the increase of β in the centre. This could be a direct effect where the measured quantity would correspond to the velocity anisotropy in the halo of the cD-galaxy. It could also be an indirect effect, as the cD-galaxy could alter the measured density slope of the dark matter and hence β through the Jeans equation. To investigate this, we found brightness profiles of the brightest cluster galaxy for nine members of our sample in the 2MASS survey (Skrutskie et al., 2006), and included these in the mass budget of the clusters. However, we immediately found that only unrealistically large mass-to-light ratios for the central galaxies could affect our mass-modeling, confirming the assumption that the galaxy masses are negligible. This ruled out the indirect effect. We also considered two higher-resolution simulated galaxy cluster halos (see Sommer-Larsen & Limousin, 2009), where a more detailed model of galaxy formation was included. However, the velocity anisotropy was found to be, $\beta \sim 0.1$, and roughky constant close to the innermost resolved radius. Hence, while not negligible, there was no indication of the large central anisotropy we measured. We hope to investigate this issue in the future with both higher resolution observational data and numerical simulations.

There is considerable potential in using the velocity anisotropy profile to constrain the thermal state of the ICM. For example, it may be possible to use a universal velocity anisotropy profile as a measure for testing hydrostatic equilibrium of the ICM. For that, a better understanding of the dynamical state of simulated dark matter halos is needed, including a systematic picture of the halo-to-halo scatter around the typical anisotropy profile. A first step observationally is an investigation of how the measured velocity anisotropy correlates with other probes of the dynamical state such as the centroid shift.

5.3 Paper III: Host & Hansen (2009)

A detailed statistical analysis of the dark matter mass profiles of galaxy clusters

In this paper we investigate the mass distribution of clusters in a subsample of 11 of the clusters used in Paper II. We perform detailed statistical comparisons with a number of different parametrized mass models from the numerical simulation literature.

Lacking a fundamental prediction of the dark matter mass profile, various parametrized fitting models are used to model halos in numerical simulations (section 4.2). While the two-parameter NFW is the de facto standard, there is some tension between this profile and observations regarding the inner slope for dwarfs and spirals, and even in some cases for clusters. Recent high-resolution simulations also seem to prefer the Einasto model, which has an additional free shape parameter.

The ubiquitous χ^2 goodness-of-fit statistic is not necessarily a good basis for model comparison if there are more free parameters in one model than in the other, if the parameters of different models have very different physical meaning, or if an extra parameter has very limited effect on the observables in the measured range. Hence it is necessary to define a metric in the parameter space of each model, in which the agreement between model and data can be assessed quantitatively and unambiguously. In Bayesian statistics, this is the prior probability distribution of the model parameters. This describes the *a priori* 'state of knowledge' about the parameters, before the data are taken into account. As usual, the measurements are described by the likelihood of the data given the parameters, $\mathcal{L}(x_i|\theta) \propto \exp(-\chi^2/2)$, which assumes Gaussian-distributed measurement uncertainties. The performance of a model in describing the data can be summarized by the average of the likelihood over the prior of the model, and this average is the Bayesian evidence E. The Bayes factor of two models is the ratio $B_{12} = E_1/E_1$ and says how much more (or less) probable model 1 is in light of the data than model 2. This basis for comparison by default penalizes extra parameters, unless these parameters result in a significantly better description of the data.

We use Bayes factors to compare a number of two- and three-parameter mass profile models
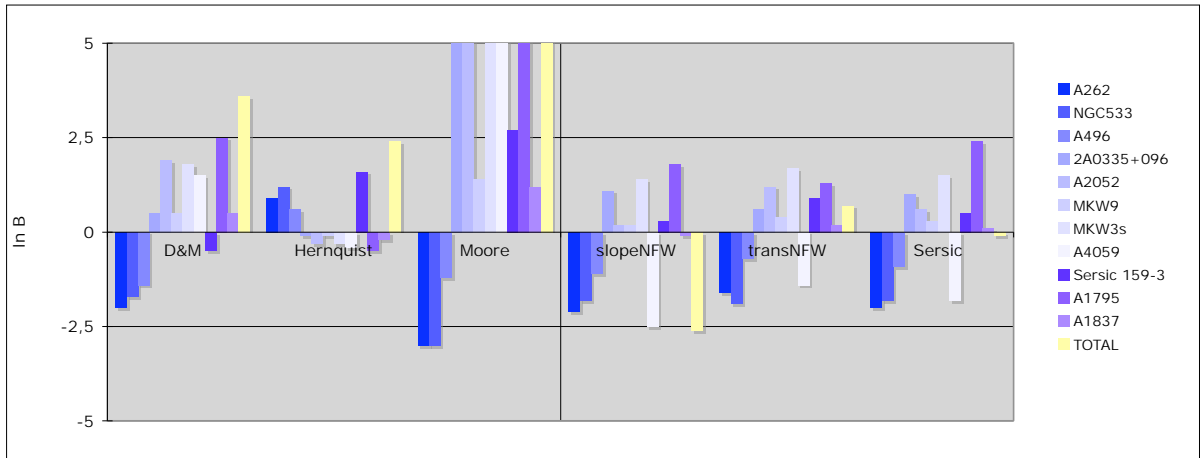
Fig. 5.5: Logarithm of the Bayes factors (the relative odds) of the different models relative to the NFW
for each cluster and for the sample as a whole. A positive Bayes factor shows that the NFW
is preferred. The NFW is the best two-parameter profile, but there is moderate evidence that
the slopeNFW model, a generalized NFW model with a freely varying inner slope, is preferred
by the data.

against the observed mass profiles. The models
include the NFW and the Einasto/Sersic profiles,
as well as generalized NFW profiles where the in-
ner slope or the transition parameter is allowed to
vary. Figure 5.5 shows the Bayes factors for each
model relative to the NFW. For the two-parameter
models we find that the NFW is preferred, and
that the Moore profile with a steep inner cusp
($\alpha = 1.5$) is convincingly ruled out. For the three-
parameter models, the 'slopeNFW' profile with a
free inner slope is significantly preferred over the
NFW and over all the other models considered.
The 'transNFW' and Sersic models perform as well
as the simple NFW. In all cases there is consider-
able and significant variation from cluster to cluster
regarding which model is preferred and how strong
that preference is. In particular, the least massive
and/or lowest redshift clusters prefer steep inner
slopes, but the sample is too small to claim this is
a general trend. There is also significant variation
in the preferred value of the shape-parameter of
all three three-parameter models, i.e. the shape pa-
rameters do not converge. We conclude that there
is moderate evidence of a non-universal mass profile
in our sample, and that the best parametrization
is an NFW-like double power law with free inner
slope.

Additionally, we consider the NFW mass–
concentration relation of our sample which is shown
in figure 5.6. At $\Delta = 2500$ the relation is robust and
quite model-independent since r_{2500} is within the
radial range of the data, but at $\Delta = 200$ it is nec-
essary to extrapolate outside the range of the data.
Our sample is not ideal for constraining the M–c re-
lation since more than half of our clusters have very
similar masses and concentrations. However, we
can study the normalization of the $M - c$ relation,
and there is good agreement for both $\Delta = 2500$
and $\Delta = 200$ with the relations found in numerical
simulations.

Paper III presents a more thorough model com-
parison of mass profiles than what is usually found
in the literature, either observationally or for nu-
merical simulations. Several authors have claimed
to observe discrepancies with ΛCDM predictions,
especially for the inner slope, based on only a single
or a few observed clusters. The statistical meth-
ods we use can readily be carried over to other
observations or applied to numerical simulations.
In particular, it would be interesting to analyze
Chandra observations since the improved angular
resolution would likely provide stronger constraints
on the inner slope. It is also worth noting that
we find good agreement with the normalization of
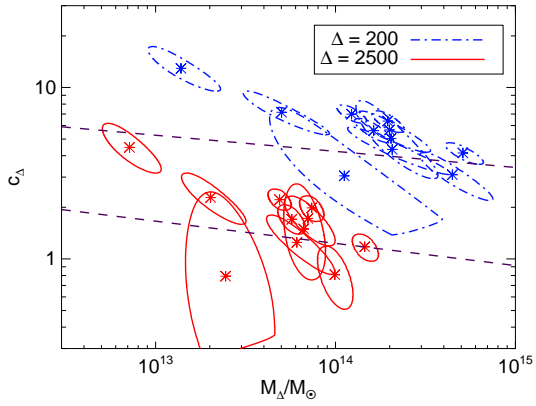
Fig. 5.6: The mass–concentration relation, M_Δ vs. c_Δ, of our sample for $\Delta = 200$ and $\Delta = 2500$. The dashed lines are the relations from the simulations of Macciò et al. (2008), based on the WMAP 5-year cosmology, and are in good agreement with our results, unlike several other recent observational studies.

the mass-concentration relation as predicted in the WMAP 5-year results, unlike some other analyses.

APPENDIX

A. PAPER I: WHAT IT TAKES TO MEASURE A FUNDAMENTAL DIFFERENCE BETWEEN DARK MATTER AND BARYONS: THE HALO VELOCITY ANISOTROPY

Ole Host, Steen H. Hansen

Dark Cosmology Centre, Niels Bohr Institute, University of Copenhagen, Juliane Maries Vej 30, DK-2100 Copenhagen Ø, Denmark

Abstract

Numerous ongoing experiments aim at detecting WIMP dark matter particles from the galactic halo directly through WIMP-nucleon interactions. Once such a detection is established a confirmation of the galactic origin of the signal is needed. This requires a direction-sensitive detector. We show that such a detector can measure the velocity anisotropy β of the galactic halo. Cosmological N-body simulations predict the dark matter anisotropy to be nonzero, $\beta \sim 0.2$. Baryonic matter has $\beta = 0$ and therefore a detection of a nonzero β would be strong proof of the fundamental difference between dark and baryonic matter. We estimate the sensitivity for various detector configurations using Monte Carlo methods and we show that the strongest signal is found in the relatively few high recoil energy events. Measuring β to the precision of ~ 0.03 will require detecting more than 10^4 WIMP events with nuclear recoil energies greater than $100\,\mathrm{keV}$ for a WIMP mass of $100\,\mathrm{GeV}$ and a $^{32}\mathrm{S}$ target. This number corresponds to $\sim 10^6$ events at all energies. We discuss variations with respect to input parameters and we show that our method is robust to the presence of backgrounds and discuss the possible improved sensitivity for an energy-sensitive detector.

A.1 Introduction

Several cosmological probes have shown that there is a dark matter component in the universe comprising about one quarter of the average energy density (Tegmark et al., 2004; Cole et al., 2005; Spergel et al., 2007). The local density of dark matter in the solar neighborhood is estimated to be in the range $\rho_0 = 0.2 - 0.6\,\mathrm{GeV/cm^3}$ (Jungman et al., 1996). Several dark matter candidates in the form of WIMPs, Weakly Interacting Massive Particles, have been suggested including the lightest supersymmetric particle (LSP) in SUSY extensions of the standard model, sterile neutrinos and axions – see the review Bertone et al. (2005) for a discussion.

Recent years have seen a remarkable progress in the understanding of dark matter structures. Universal trends have been identified and quantified using numerical cosmological simulations. One of the most discussed general trends lies in the behaviour of the universal density profile (Navarro et al., 1997; Moore et al., 1998; Fukushige & Makino, 1997), which has likely been explained (Hansen, 2004; Austin et al., 2005; Dehnen & McLaughlin, 2005). Another general result of cosmological simulations is that the velocity anisotropy is zero near the central region, and positive in the outer region (Buote & Lewis, 2004; Cole & Lacey, 1996). There even appears to be a universal connection between the local slope of the density profile and the local velocity anisotropy, which allows one to predict that the value of the velocity anisotropy near the Earth should be non-zero and of the order 0.2 (Hansen & Moore, 2006; Hansen & Stadel, 2006). Studies have shown that the velocity anisotropy can have a measurable effect on the detection rates of WIMPs (Vergados, 1999; Evans et al., 2000; Green, 2002). The physical interpretation of this velocity anisotropy is that the local dark matter 'temperature' is different in the tangential and radial directions with respect to the galactic centre. Thus, a non-zero velocity anisotropy of the dark matter presents a sharp contrast with a typical baryonic gas. This implies that an eventual measurement of the anisotropy would be a strong proof that dark matter really behaves significantly and fundamentally different from ordinary matter. This is the main reason why we here present a possible method, based on direct detection of dark matter, by which one eventually will be able to measure this property characterizing the dark matter halo.

Detecting dark matter directly involves measuring the recoil of a nucleus which is scattered by the WIMP. At present, several direct detection experiments search for WIMPs from the galactic halo. Strategies differ, but the best exclusion limits at the moment are provided by low background cryogenic detectors detecting phonons and either ionization, such as CDMS (Akerib et al., 2006) and EDELWEISS (EDELWEISS Collaboration, 2007), or scintillation as CRESST (Bravin et al., 1999). However, KIMS (Lee et al., 2007) are also competitive using only scintillation. A promising alternative is dual-phase noble gas detectors measuring scintillation and ionization, for example ZEPLIN (Alner et al., 2007), XENON10 (Baudis, 2007b) and ArDM (Laffranchi & Rubbia, 2007). These are relatively easily scalable to ton-mass detectors. The only collaboration to claim a detection so far is DAMA (Bernabei et al., 2000) which relies on detecting the weak annual modulation of the signal rate induced by the motion of the Earth (Freese et al., 1988). However, the claim appears to be ruled out by CDMS (Akerib et al., 2006) and is heavily disputed. Of particular interest to the present work are the direction sensitive detectors DRIFT (Alner et al., 2005) and NEWAGE (Miuchi et al., 2007). DRIFT is a $1\,\mathrm{m^3}$ negative ion time projection chamber (TPC) situated in the Boulby Mine in the UK. The collaboration has provided proof-of-principle and are running the second stage of the detector. NEWAGE is a micro-TPC in the R&D stage.

Direction-sensitive detectors search for a WIMP signal induced by the solar motion through the WIMP halo (Spergel, 1988). This causes a large forward-backward asymmetry in the recoil signal rate as shown in figure A.1. The magnitude of the asymmetry depends mainly on the solar orbital speed. Analyses suggest that less than 10 WIMP events in a direction-sensitive detector may confirm the signal as being galactic due to the large forward-backward asymmetry (Copi et al., 1999; Copi & Krauss, 2001; Green & Morgan, 2007; Morgan et al., 2005). Hence, while direction sensitive detectors are less likely to provide first detection, they may well provide a crucial confirmation of the galactic origin of a WIMP signal. However, the asymmetry is also weakly dependent on the velocity anisotropy of the dark matter halo and therefore a careful measurement of the asymmetry allows for a determination of β.

A.2 Modelling

In this section we discuss the components of the Monte Carlo simulation. The simulation generates a detector event by randomly selecting a WIMP velocity in the galactic halo, transforming the velocity to the detector and calculating the detector response to the event.

Dark matter velocity distribution

We make the simplest assumption for the velocity distribution which is a modified Maxwell-Boltzmann dis-
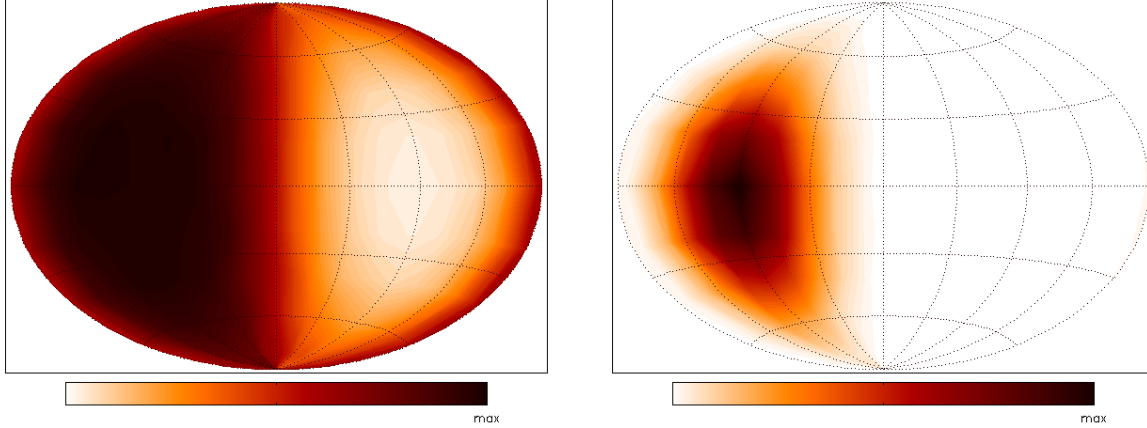
Fig. A.1: Hammer-Aitoff projections of the sky in galactic coordinates showing the directional nuclear recoil rate in our fiducial model. On the left all recoils are shown, on the right only those with a recoil energy $E_{\mathrm{rec}} > 100\,\mathrm{keV}$. The Sun moves towards $90°$ longitude on the Galactic equator.

tribution,

$$f(\vec{v})\,\mathrm{d}^3 v \;=\; \frac{1}{(2\pi)^{3/2}\sigma_r\sigma_t^2} \times$$
$$\exp\left(-\frac{v_r^2}{2\sigma_r^2} - \frac{v_\theta^2 + v_\phi^2}{2\sigma_t^2}\right)\mathrm{d}^3 v, \quad (\mathrm{A.1})$$

in which the one-dimensional radial and tangential velocity dispersions are related through $\beta = 1 - \sigma_t^2/\sigma_r^2$. As explained in the introduction, numerical simulations predict $\beta \sim 0.2$ near the Earth. When varying β we fix the total velocity dispersion $\sigma = \sqrt{\sigma_r^2 + 2\sigma_t^2}$ at $\sigma = v_0 = 230\,\mathrm{km s^{-1}}$, the circular orbit velocity. The distribution is cut off at an escape velocity of $v_{\mathrm{esc}} = 600\,\mathrm{km s^{-1}}$. More general distributions (Hansen et al., 2006; Vergados et al., 2008) will require a more detailed study.

The velocity of the Earth through the Galaxy is calculated as specified in Appendix B of Lewin & Smith (1996) to obtain the WIMP velocity $\vec{v}$ in the detector. The velocity is the sum of the Earth's orbit around the Sun $\vec{v}_E$, the solar motion $\vec{v}_\odot$ with respect to the local standard of rest and the galactic orbital speed of the local standard of rest, which is just the circular orbit velocity v_0. The solar motion measured by the Hipparcos satellite (Dehnen & Binney, 1998) is, in Galactic coordinates, $\vec{v}_\odot = (10.0, 5.2, 7.2)\,\mathrm{km s^{-1}}$. We refer to Lewin & Smith (1996) for the calculation of $\vec{v}_E$ as a function of time and date.

WIMP-nucleus interaction

A WIMP can be detected by the nuclear recoil produced when it scatters off a target nucleus in a detector. We consider the case where the dominant channel is spin-independent elastic scattering, which is coherently enhanced by the number of nucleons at low energies. The cross section depends on the momentum transfer q as

$$\sigma(q) = \sigma_0 |F(q)|^2, \quad (\mathrm{A.2})$$

where $F(q)$ is the nuclear form factor and σ_0 is the cross section in the limit of zero momentum transfer. Following Lewin & Smith (1996), the WIMP-nucleus interaction is modelled by the Helm form factor (Helm, 1956),

$$F(qr_n) = 3\frac{j_1(qr_n)}{qr_n}\exp\left(-(qs)^2/2\right), \quad (\mathrm{A.3})$$

where $r_n = 1.14A^{1/3}$ is the approximate nuclear radius and $s = 0.9\,\mathrm{fm}$ is the skin thickness parameter. For elastic scattering the momentum transfer is given by

$$q = 2\mu v\cos\theta, \quad (\mathrm{A.4})$$

where $\mu = m_t m_W/(m_t + m_W)$ is the reduced mass of the WIMP-target system, v is the laboratory speed of the incoming WIMP and θ is the recoil angle of the nucleus with respect to $\vec{v}$. For each event, the maximum possible momentum transfer is determined by the velocity of the WIMP. The distribution $|F(q)|^2$ is then randomly sampled in the interval up to the maximum momentum transfer to determine the actual momentum transfer. This fixes the scattering angle θ through eq. (A.4).

Detector

The directional WIMP signal is unavoidably smeared out by the fact that only the nuclear recoil is observed, not the WIMP itself. In addition to this, the detector will have a limited angular resolution with which the initial nuclear recoil direction can be reconstructed. For example, in the DRIFT time projection chamber, the ionization cloud from a typical recoil will drift onto only a few anode wires in the readout (Spooner, 2007). This, coupled with the charge diffusion, necessarily limits the accuracy with which the recoil can be reconstructed. High energy recoil events produce longer ionization tracks, hence it is easier to measure the direction of more energetic events.

In an actual experiment the angular resolution must be carefully measured. Here, we model it by rotating the recoil velocity in a random direction by an angle α drawn from the Fisher distribution on the sphere $p(\alpha) \propto \exp(\kappa \cos \alpha)$ (Fisher, 1953). The parameter κ fixes the width of the distribution with larger κ corresponding to a more centralized distribution. We consider perfect reconstruction of the direction, $\kappa = \infty$, as well as $\kappa = 5$ and $\kappa = 2.3$ corresponding to half the sampled angles being greater than $30°$ and $45°$, respectively.

Another parameter characterizing the detector is the detector threshold energy E_{thr}. A realistic detector cannot measure the direction of nuclear recoils below this energy since low energy recoils will not move sufficiently long distances in the detector. Naturally the total signal rate is lowered for increasing threshold energy.

Calibrating the asymmetry-anisotropy relation

The observed asymmetry depends on β in a non-trivial way which necessitates Monte Carlo calibration.

We define the angle ϕ between the observed nuclear recoil direction and the direction of the solar motion through the halo. If ϕ is less than a chosen acceptance angle α_{acc} the event is counted as a forward event while if ϕ is greater than $180° - \alpha_{\mathrm{acc}}$ the event is a backward event. The observed asymmetry is the difference between the number of forward and backward events. From figure A.2, it is evident that the asymmetry is large, compared to the total number of signals, but the dependence on β is weak. The relative asymmetry is the difference between the number of forward and backward events with $E_{\mathrm{rec}} > E_{\mathrm{thr}}$, divided by the total number of generated events, regardless of recoil energy. In other words, it is the probability that a random detector event will add to the asymmetry given E_{thr} and α_{acc}.

The relation between the relative asymmetry and the velocity anisotropy is calibrated by simulating 10^8 events for β in the range $(-0.5, 0.5)$ in steps of 0.05. For each β, the relative asymmetry is tabulated for a number of threshold energies and acceptance angles. Third order polynomials are fitted to the calculated relative asymmetries and used as calibration curves. Figure A.3 shows the calibration curves at threshold energies of $0\,\mathrm{keV}$ and $100\,\mathrm{keV}$. Note that for low threshold energy, the relative asymmetry increases with β while the opposite is true for high threshold energy. This change in behaviour occurs in the region of $E_{\mathrm{thr}} \simeq 40\,\mathrm{keV}$, increasing with the smaller acceptance angles.

The calibration depends on both the WIMP and target masses, m_W and m_t, on the assumed velocity dispersion σ, and on the angular resolution of the detector, κ. Further, each configuration of detection energy threshold and acceptance angle results in a different calibration. We calculate calibration curves for $E_{\mathrm{thr}}/(\mathrm{keV}) \in [0, 20, 40, 70, 100, 140, 180]$ and $\alpha_{\mathrm{acc}} \in [90°, 60°, 45°, 36°, 30°, 26°, 22°]$.

A.3 Results

Now we discuss the sensitivity, i.e. the mean or expected accuracy, with which the velocity anisotropy can be measured, depending on the experimental configuration. We simulate a large number of experiments, each measuring β from a number of observed nuclear recoils. The measurement is done by converting the observed relative asymmetry in each experiment to a value for β using the calibration curves discussed above. This yields a distribution of measurements and the sensitivity is the width of this distribution.

Signal rates

We do not calculate specific rates, rather we assume a WIMP mass and a target nucleus and estimate the sensitivity from a number of generated events for different E_{thr} and α_{acc}. Increasing E_{thr} lowers the signal rate by a factor depending on the masses. Table A.1 lists the fraction of recoils with energy above a given threshold for some combinations of m_W and target nucleus. For example, out of 1000 recoils only about 30 would have recoil energy greater than $100\,\mathrm{keV}$ if $m_W = 100\,\mathrm{GeV}$ and the target is $^{32}\mathrm{S}$. It is therefore natural to compare sensitivities for different threshold energies between simulations with the same number of total generated events.

The actual signal rate in a detector is proportional to ρ_0/m_W, where ρ_0 is the WIMP density in the vicinity of the solar system.
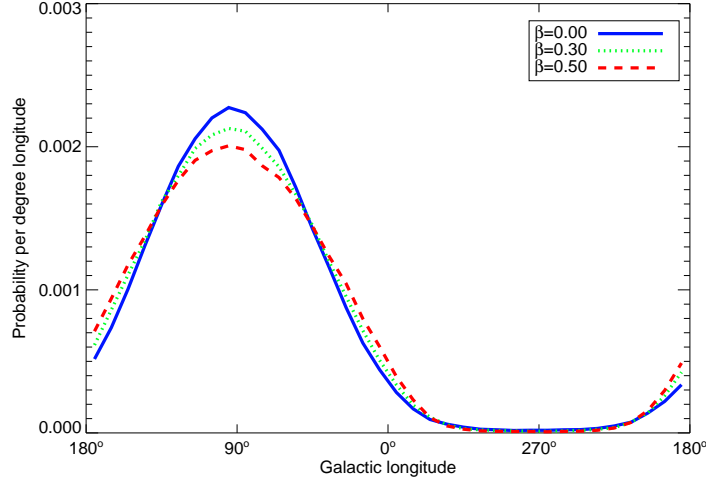
Fig. A.2: Distributions of nuclear recoils with respect to galactic longitude, normalized to unity, for three values of β. An energy threshold of $E_{\text{thr}} = 100\,\text{keV}$ has been applied, other parameters are as in the fiducial model.

Tab. A.1: Fraction of nuclear recoils with recoil energy above E_{thr}.

E_{thr} (keV)	0	20	40	70	100	140	180
^{32}S target, $m_W = 100\,\text{GeV}$	1.0	0.35	0.18	0.074	0.030	0.0082	0.0018
^{12}C target, $m_W = 100\,\text{GeV}$	1.0	0.22	0.073	0.013	0.0014	-	-
^{32}S target, $m_W = 500\,\text{GeV}$	1.0	0.44	0.27	0.14	0.073	0.031	0.013

Fiducial model

We consider a fiducial model with velocity anisotropy $\beta = 0.1$, a WIMP mass of $m_W = 100\,\text{GeV}$, a ^{32}S target nucleus and perfect reconstruction of the recoil direction, $\kappa = \infty$. We simulate a total of 10^9 detector events which we group as 1000 experiments obtaining 10^6 WIMP detections each. The distribution of measured β's for these 1000 simulated experiments is shown in figure A.4 for $E_{\text{thr}} = 100\,\text{keV}$ and $\alpha_{\text{acc}} = 45°$. The width σ_β of the distribution is the desired estimate of the experimental sensitivity to β. Explicitly, a detector reconstructing the direction of the roughly 3×10^4 events with recoil energy greater than $100\,\text{keV}$ (out of the 10^6 events at all energies) is expected to be able to measure β with an accuracy of $\sigma_\beta = 0.029$, if $\beta = 0.1$.

The sensitivity in the fiducial model is shown in figure A.5 for various acceptance angles as a function of threshold energy. The best sensitivity is obtained for the above-mentioned configuration, $\alpha_{\text{acc}} = 45°$ and $E_{\text{thr}} = 100\,\text{keV}$, for which $\sigma_\beta = 0.029$. Very similar results are obtained for $E_{\text{thr}} = 0\,\text{keV}$ while inter-mediate threshold energies are less optimal. The dependence on α_{acc} is weak for large threshold energies, but rather strong at low and intermediate E_{thr}. The optimal threshold energy at $100\,\text{keV}$ should be understood as the best compromise between a steep calibration curve and a large number of events. Explicitly, the asymmetry is more enhanced if only high energy events are detected, but the lower number of events reduces the signal to noise ratio. For zero threshold energy, the opposite happens as there is a large number of events but each event contains less information. The poor performance at intermediate E_{thr} is mainly due to the calibration curves changing from positive to negative slope as the threshold energy increases while the increase in σ_β for $E_{\text{thr}} > 100\,\text{keV}$ is due to the low number of events with sufficient recoil energy. The simulated experiments reproduce the input $\beta = 0.1$ consistently. The only unfortunate exceptions are for $\alpha_{\text{acc}} = 90°$ and $E_{\text{thr}} = 20$ or $40\,\text{keV}$ in which case the flatness of the calibration curves and the low signal per event smear the distribution out over a wide range of β's.
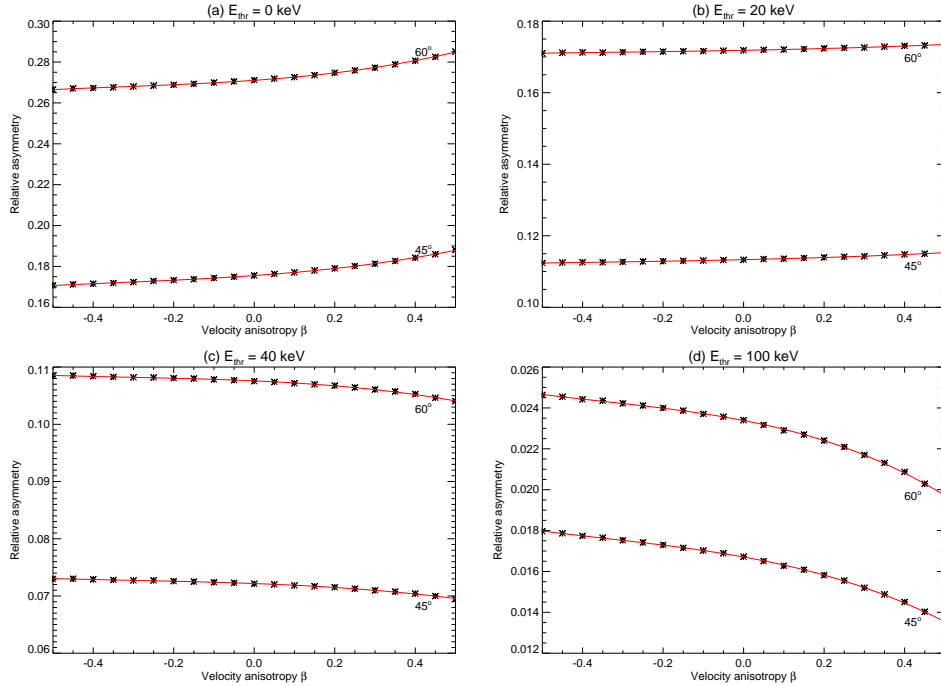
Fig. A.3: Calibration curves for (a) $E_{\mathrm{thr}} = 0\,\mathrm{keV}$, (b) $E_{\mathrm{thr}} = 20\,\mathrm{keV}$, (b) $E_{\mathrm{thr}} = 40\,\mathrm{keV}$ and (d) $E_{\mathrm{thr}} = 100\,\mathrm{keV}$, acceptance angles as labelled. The calibration is for the fiducial model, i.e. $\kappa = \infty$, $m_W = 100\,\mathrm{GeV}$ and $^{32}\mathrm{S}$ target.

The measured value of the relative asymmetry in the 1000 experiments is close to Gaussian since the number of forward events is very large, the number of backward events is very small and each number is Poisson distributed. However, since the calibration curves are not straight lines the distribution of measured β's is distorted. The measure of this distortion is the sample skewness, which is the ratio of the third sample moment to the second,

$$\gamma = \frac{\mu_3}{\sigma^3} = \frac{\sqrt{n}\sum_i(\beta_i - \bar{\beta})^3}{[\sum_i(\beta_i - \bar{\beta})^2]^{3/2}}. \quad (A.5)$$

In particular, we find large, negative skewness $\gamma \lesssim -1$ for low threshold energies as well as for $\alpha_{\mathrm{acc}} = 90°$. In these cases a Gaussian fit is not a good representation of the distribution of β's and we take the sample standard deviation of the unbinned distribution as the sensitivity instead.

The dependence on the number of detected events is investigated by regrouping the 10^9 simulated events into more experiments with fewer detections. Figure A.6 shows the obtained accuracy for 4×10^5 events, i.e. 2.5 times fewer than the fiducial configuration. The

best σ_β is again obtained at $E_{\mathrm{thr}} = 100\,\mathrm{keV}$ and $\alpha_{\mathrm{acc}} = 45°$, for which $\sigma_\beta = 0.047$. In general we find that $\sigma_\beta \propto 1/\sqrt{N}$ for experiments with at least 10^5 events, as expected. However, the skewness becomes more and more pronounced as the number of detector events is reduced.

In summary, to make a coarse measurement of the velocity anisotropy of the dark matter halo with an accuracy of about 0.1, about 10^5 WIMPs at all energies would be needed. However, a detector which is insensitive to the recoil energy should ideally only count the nuclear recoils with energy greater than $100\,\mathrm{keV}$. A precision measurement would require more than 10^6 events, corresponding to a ton-scale direction-sensitive detector operating for several years if the cross-section is $10^{-7}\mathrm{pb}$. These numbers, compared to the present status of WIMP directional detection experiments, are of course very large and would require a large dedicated experimental programme. Additionally, a cross-section of 10^{-7} pb may be too optimistic – for example, a recent study found that the most favored region would be the range $10^{-10} - 10^{-8}$ pb (Trotta et al., 2007).
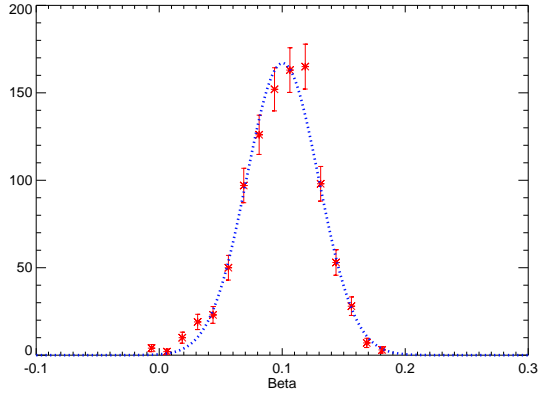
Fig. A.4: Binned distribution of measured β's in the fiducial model with 10^6 detector events, $E_{\mathrm{thr}} = 100\,\mathrm{keV}$ and $\alpha_{\mathrm{acc}} = 45°$. The width of the distribution defines the sensitivity for this experimental configuration. The curve shows the Gaussian fit which has $\sigma_\beta = 0.029$.

Parameter influence

Next, we investigate the consequences of varying each of the parameters of the fiducial model independently.

- First and most important, a limited detector angular resolution, $\kappa = 5$, is found to increase σ_β by 30%. A poorer detector with $\kappa = 2.3$ increases σ_β by 75%. The optimal acceptance angle in both cases is $\alpha_{\mathrm{acc}} = 60°$. In these cases, the σ_β's obtained at zero threshold energy are notably poorer than at $100\,\mathrm{keV}$, unlike in the fiducial model. One might expect the resolution would have a stronger effect but it should be remembered that the WIMP recoil distribution is already smeared out by the nuclear recoil distribution so the relative decrease due to a finite κ is small.

- If the target nucleus mass is lowered, the reduced mass of the WIMP-nucleus system is decreased and, from eq. (A.4), so is the width of the recoil angle distribution. Hence the nuclear recoil direction resembles the incoming WIMP direction better. For a $^{12}\mathrm{C}$ target, σ_β is decreased by 15%. The lower reduced mass also lowers the optimal threshold energy to $E_{\mathrm{thr}} = 70\,\mathrm{keV}$.

- If the WIMP mass is increased, the reduced mass is also increased and the recoil angle distribution becomes wider, resulting in poorer sensitivity. For $m_W = 500\,\mathrm{GeV}$ we find σ_β is increased by 10% and the optimal threshold energy is $180\,\mathrm{keV}$. It

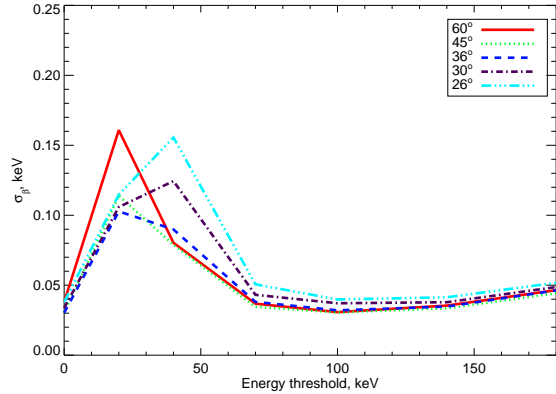Fig. A.5: Sensitivity σ_β of measurement of β as a function of detector energy threshold for various acceptance angles in the fiducial model.

Tab. A.2: Impact of varying the parameters of the fiducial model independently.

Parameter	Best σ_β	E_{thr} (keV)	α_{acc}
Fiducial model	0.029	100	45°
$\kappa = 5$	0.037	100	60°
$\kappa = 2.3$	0.051	100	60°
$m_W = 500\,\mathrm{GeV}$	0.033	180	45°
$^{12}\mathrm{C}$ target	0.025	70	45°
$\beta = -0.1$	0.045	100	45°

should be noted here that since the WIMP flux is inversely proportional to m_W, it would take five times as long to record the same number of events if $m_W = 500\,\mathrm{GeV}$ rather than $100\,\mathrm{GeV}$.

- Finally, if the 'true' value of β is instead -0.1 the smaller slope of the calibration curve causes σ_β to increase by about 50%. The opposite is true if $\beta = 0.3$, in which case σ_β decreases by 40%. Hence, if the actual value of β is larger than the 0.1 in our reference model, the number of events needed to measure β is significantly smaller. For example, measuring $\beta = 0.3$ to a precision of about ± 0.06 would require roughly 3 000 events above $100\,\mathrm{keV}$. Figure A.7 shows the variation of the sensitivity with the assumed true value of β.

The best obtained σ_β for these parameters and the corresponding optimal acceptance angle and threshold energy are summarized in table A.2.
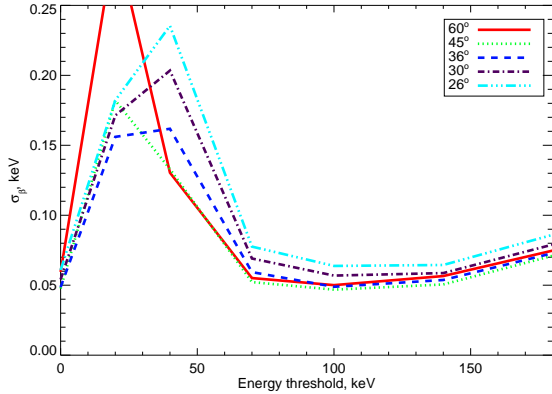
Fig. A.6: Same as figure A.5 but with 4×10^5 events per experiment.

Fig. A.7: Variation of the sensitivty with the input value of β for $\alpha_{\mathrm{acc}} = 45°$ and $60°$ and $E_{\mathrm{thr}} = 100\,\mathrm{keV}$. The dependence is primarily determined by the calibration curve.

Background

So far we have assumed a zero background level. Now we discuss the influence of a nonzero background which is assumed to be isotropic in the Galactic frame when averaged over time (Morgan & Green, 2005). We consider the impact on the optimal detector configuration for the fiducial model, $E_{\mathrm{thr}} = 100\,\mathrm{keV}$ and $\alpha_{\mathrm{acc}} = 45°$. For each simulated experiment we add a number of background events to the forward and backward signal events. These two numbers are drawn from a Poisson distribution with mean equal to a fraction of the number of forward signal events. The asymmetry is then calculated as before and the calibration curve is used to determine the measured value of β. We find that the degradation due to nonzero background is benign, as long as the signal is not weaker than the background. For a 25% background level the sensitivity $\sigma_\beta = 0.037$, an increase of less than 30%. For a 100% background, $\sigma_\beta = 0.06$ while for a 400% background $\sigma_\beta = 0.10$. The distribution of measured β's still reproduce $\beta = 0.1$ consistently as shown in figure A.8.

The well-behaved performance of the sensitivity with respect to nonzero backgrounds can be attributed to our method of measuring the velocity anisotropy from the difference of the number of forward and backward signals, defined within equal solid angles. This method is largely insensitive to the background level, since the expected number of background events is the same in the forward and backward bins.

Energy resolution

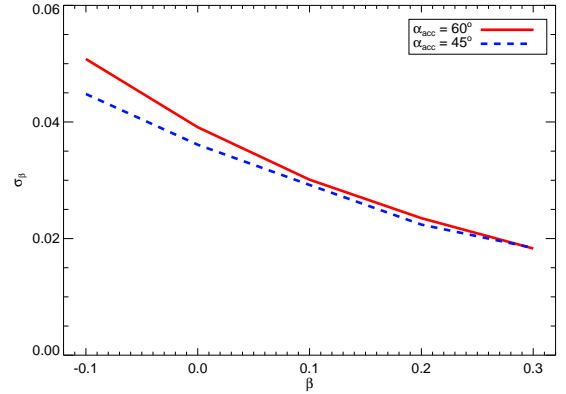We have not assumed that the detector can measure the nuclear recoil energy. However, as is evident from the calibration curves in figure A.3 the forward-backward asymmetry increases with β for low energy recoils but decreases for high energy recoils. Hence a 'cleaner' signal can be obtained if the experiment is able to place events into energy bins with some resolution.

We have investigated the possible improvements by binning events into 15 keV bins according to their recoil energy, i.e. with no additional detector resolution effects. For each energy bin and acceptance angle we calculate separate calibration curves. The flip from positive to negative slope of the calibration curves takes place at about $E_{\mathrm{rec}} = 60\,\mathrm{keV}$ for the fiducial model. Hence, at intermediate recoil energies there is virtually no sensitivity to β. Following the usual procedure, we calculate the distribution of measured β's in each energy bin. For 10^6 events distributed over all bins, the measurements reproduce the input β for low ($\lesssim 50\,\mathrm{keV}$) and high ($\gtrsim 100\,\mathrm{keV}$) recoil energies. The best sensitivity in individual bins is obtained in the lowest energy bin, $E_{\mathrm{rec}} \in (0, 15)\,\mathrm{keV}$ for which $\sigma_{\beta, E} = 0.032$. If the results of the bins that reproduce $\beta = 0.1$ are combined through $\sigma_\beta^{-2} = \sum_i \sigma_{\beta, E_i}^{-2}$, a sensitivity of $\sigma_\beta = 0.20$ is achieved. This corresponds roughly to the improvement obtained by our standard detector with no energy resolution taking data for twice as long.

It is interesting to note that a direction-sensitive detector with high energy resolution will be able to extend the study of (Drees & Shan, 2007) to extract the shape of the full 3-dimensional velocity distribution function.
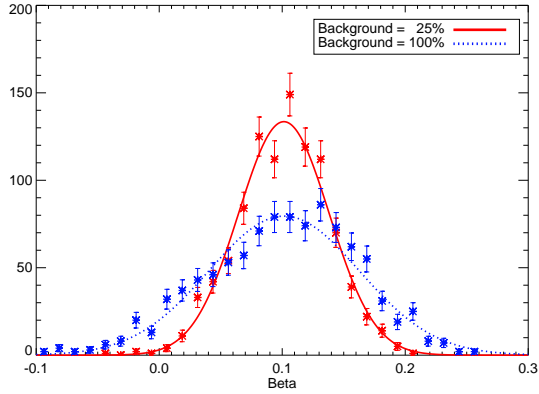
Fig. A.8: Binned distributions of measured β's in the fiducial model as in figure A.4 but including a background level set relative to the number of forward events. The sensitivities are $\sigma_\beta = 0.037$ and $\sigma_\beta = 0.06$ for 25% and 100% background levels, respectively.

anisotropy, implying a steep calibration curve, while intermediate energy recoils show little sensitivity. Since the calibration curves for low and high energy recoils have positive and negative slope, respectively, an energy-sensitive detector may improve the sensitivity.

A.4   Discussion

We have investigated the possibility of measuring the velocity anisotropy β of the galactic dark matter halo in a direction sensitive WIMP detector using Monte Carlo methods. The measurement is based on the well known forward-backward asymmetry in the directional spectrum of WIMP-induced nuclear recoils. A non-zero β alters the magnitude of the asymmetry slightly which makes it possible to measure β.

We find that in excess of 10^5 events across all energies are needed to make a coarse measurement of β. An experiment measuring 3×10^4 events with recoil energy greater than $100\,\mathrm{keV}$, equivalent to 10^6 events at all energies, should be able to measure β to a precision of 0.03. This result is obtained for an acceptance angle of $\alpha_{\mathrm{acc}} = 45°$, a velocity dispersion of $\sigma = 230\,\mathrm{km s^{-1}}$, a WIMP mass of $100\,\mathrm{GeV}$ and a $^{32}\mathrm{S}$ target. Such a measurement would provide a strong proof that dark matter behaves fundamentally different from baryonic matter. We also note that if β is actually larger than the 0.1 we have assumed, the required number of events can be reduced significantly.

We have investigated the dependence of the sensitivity with respect to the angular resolution and the threshold energy of the detector, the masses of the WIMP and the target and the background level. The main point is that low energy and high energy nuclear recoils carry more information about the velocity

B. PAPER II: MEASUREMENT OF THE DARK MATTER VELOCITY ANISOTROPY IN GALAXY CLUSTERS

Ole Host[1], Steen H. Hansen[1], Rocco Piffaretti[2], Andrea Morandi[1,3], Stefano Ettori[4], Scott T. Kay[5], Riccardo Valdarnini[2]

[1]Dark Cosmology Centre, Niels Bohr Institute, University of Copenhagen, Juliane Maries Vej 30, DK-2100 Copenhagen, Denmark

[2]SISSA, International School for Advanced Studies, via Beirut 2, I-34014 Trieste, Italy

[3]Dipartimento di Astronomia, Unversità di Bologna, via Ranzani 1, I-40127 Bologna, Italy

[4]INAF–Osservatorio Astronomico di Bologna, via Ranzani 1, I-40127 Bologna, Italy

[5]Jodrell Bank Centre for Astrophysics, School of Physics and Astronomy, The University of Manchester, Manchester M13 9PL, UK

Abstract

The internal dynamics of a dark matter structure may have the remarkable property that the local temperature in the structure depends on direction. This is parametrized by the velocity anisotropy β which must be zero for relaxed collisional structures, but has been shown to be non-zero in numerical simulations of dark matter structures. Here we present a method to infer the radial profile of the velocity anisotropy of the dark matter halo in a galaxy cluster from X-ray observables of the intracluster gas. This non-parametric method is based on a universal relation between the dark matter temperature and the gas temperature which is confirmed through numerical simulations. We apply this method to observational data and we find that β is significantly different from zero at intermediate radii. Thus we find a strong indication that dark matter is effectively collisionless on the dynamical time-scale of clusters, which implies an upper limit on the self-interaction cross-section per unit mass $\sigma/m \lesssim 1\,\mathrm{cm^2 g^{-1}}$. Our results may provide an independent way to determine the stellar mass density in the central regions of a relaxed cluster, as well as a test of whether a cluster is in fact relaxed.

B.1   Introduction

Our understanding of dark matter structures has increased significantly over the recent years. This progress has mainly been driven by numerical simulations which have identified a range of universalities of the dark matter structures. One of the first general properties to be suggested was the radial density profile (Navarro et al., 1996; Moore et al., 1998; Diemand et al., 2004; Merritt et al., 2006; Graham et al., 2006), whose radial behaviour was shown to change from a fairly shallow decline in the central region to a much steeper decline in the outer regions. This behaviour has been confirmed observationally for galaxy clusters, both through X-ray observations (Buote & Lewis, 2004; Pointecouteau et al., 2005; Arnaud et al., 2005; Vikhlinin et al., 2006; Pratt et al., 2006), and also more recently through strong and weak lensing observations (Sand et al., 2004; Broadhurst et al., 2005; Comerford et al., 2006; Limousin et al., 2008).

A slightly less intuitive quantity to be considered is the dark matter velocity anisotropy defined by

$$\beta \equiv 1 - \frac{\sigma_t^2}{\sigma_r^2}, \qquad (B.1)$$

where σ_t^2 and σ_r^2 are the 1-dimensional tangential and radial velocity dispersions in a spherical system (Binney & Tremaine, 1987). This anisotropy was shown in pure dark matter simulations to increase radially from zero in the central region to roughly 0.5 in the outer region (Carlberg et al., 1997; Cole & Lacey, 1996; Hansen & Moore, 2006). For collisional systems, in contrast, the velocity anisotropy is explicitly zero in the equilibrated regions. Therefore, eventually inferring β from observational data is an important test of whether dark matter is in fact collisionless, as assumed in the standard model of structure formation. On this note, it has been shown that the Galactic velocity anisotropy can affect the detection rates of direct dark matter searches (Vergados et al., 2008), and it is in principle measurable in a direction-sensitive detector (Host & Hansen, 2007).

The most massive bound structures in the Universe are clusters of galaxies, which consist of an extended dark matter halo, an X-ray emitting plasma making up the intracluster medium (ICM), and the individual galaxies. While the contribution of galaxies to the total mass is small, approximately 10 % of the cluster mass resides in the ICM. The present generation of X-ray satellites, *XMM-Newton* and *Chandra*, allows very accurate measurements of azimuthally-averaged radial profiles of density and temperature of the ICM. These are used, under the assumption of hydrostatic equilibrium and spherical symmetry of both gas and total mass distributions, to estimate total, gas, and dark matter mass profiles (Fabricant et al., 1980).

Below we infer the radial velocity anisotropy profile of dark matter in 16 galaxy clusters using a generally applicable framework without any parametrized modeling of the clusters. In short, we assume a universal relation between the effective temperature of dark matter and the ICM temperature, which allows us to solve the dynamics of the dark matter halo using the radial gas temperature and density profiles determined from X-ray data. We investigate the shape and validity of this temperature relation in two cosmological simulations of galaxy clusters, based on independent numerical codes. We apply our method to 16 galaxy clusters from two different samples and find a velocity anisotropy significantly different from zero in the outer parts, in qualitative agreement with simulations.

Our approach here is a generalization of the nonparametric analysis in Hansen & Piffaretti (2007) where β was inferred neglecting the radial dependence. We also note the parametrized analyses in Ikebe et al. (2004) and Morandi & Ettori (2007), where the total dark matter velocity dispersion was inferred assuming either $\beta = 0$, or the analytical β-profiles of Colín et al. (2000) or Cole & Lacey (1996) (see also Wojtak et al. (2008b)). In particular, Morandi & Ettori (2007) found that the dark matter temperature and the ICM temperature were essentially the same in strong cooling-core clusters.

The structure of the paper is the following: In the next section, we discuss how we relate the temperature of dark matter to the observable gas temperature. In section 3 we show how we can then solve the dynamics of the dark matter. In section 4 we test the assumed temperature relation and our method on numerical simulations, and in section 5 we apply the method to observational data. Section 6 is the summary and discussion.

B.2   The temperature of dark matter

The equality of inertial and gravitational mass implies that the orbit of a test particle in a gravitational system is independent of mass. For example, the velocity of a circular orbit in a spherical mass distribution $v_c^2 = GM(r)/r$ depends only on the distance to the center of the system and the mass contained within that radius. Therefore it is natural to assume that, at a given radius, all species in a relaxed, spherical gravitational system have the same average specific kinetic energy. Obviously, they also have the same specific potential energy. In a gas system, equilibrium implies energy equipartition between all species. It is clear that the corresponding principle for a relaxed gravitational system is a common velocity dispersion, precisely because

gravitational dynamics are independent of mass. Since the average velocity is associated with the thermal energy content, this relationship is expressed by

$$T_{\rm DM} = \kappa T_{\rm gas}. \qquad (B.2)$$

The parameter κ is constant as long as the impact of radiative or entropy-changing processes affecting the gas is negligible and the system is relaxed. Therefore, we allow for a radial dependence, $\kappa = \kappa(r/r_{2500})$, where r_{2500} is the scale radius within which the mean total density is 2500 times the critical density at the redshift of the cluster.

The dark matter temperature in eq. (B.2) is naturally not well-defined as there is no thermodynamic equilibrium for a collisionless gas. Instead, we simply define an effective dark matter temperature which is proportional to the three-dimensional velocity dispersion,

$$
\begin{aligned}
k_B T_{\rm DM} &= \frac{1}{3}\mu m_H \sigma_{\rm DM}^2 & (B.3)\\
&= \frac{1}{3}\mu m_H \left(\sigma_r^2 + 2\sigma_t^2\right). & (B.4)
\end{aligned}
$$

The velocity dispersion has been decomposed into the contributions from the one-dimensional radial and tangential dispersions. We choose the constant of proportionality to be the mean molecular mass of the intracluster gas simply to allow κ to be of order unity. Equations (B.2)–(B.4) are equivalent to assuming that the specific energies of gas and dark matter particles are the same up to a factor of κ, on average. The same conjecture was made in Hansen & Piffaretti (2007) but with $\kappa = 1$ explicitly.

It should be mentioned that the temperature relation eq. (B.2) was recently analyzed in simulations by Evrard et al. (2008). Whereas we allow a possible radial variation in the temperature relation, those authors considered averages within r_{200} and found that

$$\tilde{\kappa}_{<r_{200}} \equiv \frac{k_B \overline{T_{\rm gas}}/\mu m_H}{\overline{\sigma_{\rm DM}^2}} = 1.04 \pm 0.06, \qquad (B.5)$$

This was based on their determination of $\bar{\kappa}_{<r_{200}}^{-1} = (0.87\pm0.04)\langle T_{\rm spec}/T_{\rm mw}\rangle$, where the ratio of the spectroscopic temperature to the mass-weighted temperature was $\langle T_{\rm spec}/T_{\rm mw}\rangle = 1.1 \pm 0.05$ (Nagai, 2006). Then, in Rines et al. (2008) it was noted that by applying virial scaling to the WMAP5+SN+BAO results (Komatsu et al., 2009), an average value of $\tilde{\kappa}^{-1}|_{<r_{500}} = 1.1$ was found. The authors concluded that the observational results indicated that the average specific energy of the ICM was close to both that of the dark matter and that of the galaxies. In section B.4, we will arrive at the same conclusion for simulated galaxy clusters.

B.3 Solving the dark matter dynamics

Equation (B.2) allows us to estimate the total velocity dispersion profile of the dark matter structure from measurements of the radial temperature profile of the gas. In this section we discuss how we can proceed to determine the dark matter velocity anisotropy.

The collisionless Jeans equations relate the dynamical properties of the dark matter to the gravitational potential of the cluster. Assuming that the system is spherically symmetric and in a steady state, the second Jeans equation can be put in the form (Binney & Tremaine, 1987)

$$\frac{d(\nu\overline{v_r^2})}{dr} + \frac{\nu}{r}\left[2\overline{v_r^2} - \left(\overline{v_\theta^2} + \overline{v_\phi^2}\right)\right] = -\nu\frac{GM}{r^2}, \qquad (B.6)$$

where ν is the dark matter number density, $\overline{v_i^2}$ is the second moment of the ith velocity component, and M is the mass contained within radius r. If it is further assumed that there are no bulk flows, $\overline{v_i} = 0$, and that the tangential velocity dispersions are equal, $\sigma_\theta^2 = \sigma_\phi^2 \equiv \sigma_t^2$, the Jeans equation becomes

$$\sigma_r^2 \left(\frac{d\ln\rho_{\rm DM}}{d\ln r} + \frac{d\ln\sigma_r^2}{d\ln r} + 2\beta\right) = -\frac{GM(r)}{r}, \qquad (B.7)$$

where $\rho_{\rm DM}$ is the mass density, σ_r^2 is the radial velocity dispersion, and β is the velocity anisotropy introduced in (B.1).

Similar to the Jeans equation, the radial part of the Euler equations of the ICM expresses the condition that the thermal pressure of the gas balances the gravitational potential. This equation of hydrostatic equilibrium reads

$$\frac{k_B T_{\rm gas}}{\mu m_H}\left(\frac{d\ln n_e}{d\ln r} + \frac{d\ln T_{\rm gas}}{d\ln r}\right) = -\frac{GM(r)}{r}, \qquad (B.8)$$

where $T_{\rm gas}$ is the gas electron temperature and n_e is the number density of electrons. This important equation has been widely used to estimate the total mass of a galaxy cluster from X-ray data. In case there is turbulence or larger scale bulk motion in the gas additional terms of the form $(\vec{v}\cdot\nabla)\vec{v} - (v_\theta^2 + v_\phi^2)/r$ appear (Landau & Lifshitz, 1987). Neglecting such terms may lead to an underestimate of the mass, however this is usually not a major effect for systems that appear relaxed (Piffaretti & Valdarnini, 2008).

By equating (B.7) and (B.8) and using (B.1) and (B.2) to eliminate β, we obtain the following differential equation for the radial velocity dispersion,

$$\sigma_r^2 \left(\frac{d\ln\rho_{\rm DM}}{d\ln r} + \frac{d\ln\sigma_r^2}{d\ln r} + 3\right) = \psi(r), \qquad (B.9)$$

where the function ψ is defined by

$$\psi(r) = 3\kappa \frac{k_B T_{\text{gas}}}{\mu m_H} - \frac{GM}{r}. \tag{B.10}$$

Clearly, ψ is determined directly from the X-ray observables and the κ-profile, which we discuss in section B.4.

The differential equation (B.9) is solved by finding an integrating factor which yields

$$\sigma_r^2(r) = \frac{1}{\rho_{\text{DM}}(r) \, r^3} \int_0^r dr' \, \psi(r') \rho_{\text{DM}}(r') r'^2. \tag{B.11}$$

The dark matter density is determined as usual through $\rho_{\text{DM}} = \rho_{\text{tot}} - \mu m_H n_e$. With the radial velocity dispersion profile determined, the velocity anisotropy is easily recovered from either the temperature relation eq. (B.2) or the Jeans equation (B.7),

$$2\beta_{\text{tr}} = 3\left(1 - \kappa \frac{k_B T_{\text{gas}}}{\mu m_H \sigma_r^2}\right), \tag{B.12}$$

$$2\beta_{\text{Je}} = -\frac{d\ln(\rho_{\text{DM}} \sigma_r^2)}{d\ln r} - \frac{GM}{r\sigma_r^2}. \tag{B.13}$$

Obviously these two expressions should be equal. This can be used as a consistency check on whether numerical issues related to the differentiations and integration involved are kept under control.

To summarize, the assumed relation eq. (B.2) between the effective dark matter temperature and the gas temperature, along with the mass estimate from (B.8), allows us to solve the dark matter dynamics directly from X-ray data, and determine both the radial velocity dispersion and the velocity anisotropy as functions of radius.

B.4   Cluster simulations

We use numerical simulations of the formation of galaxy clusters in the ΛCDM cosmology to investigate the validity and shape of the temperature relation eq. (B.2), and to test the method for determining the velocity anisotropy. In order to check systematic effects we take samples from two different simulations based on two completely independent numerical codes.

CLEF

We first consider a sample of 67 clusters taken from the CLEF simulation (Kay et al., 2007), details of which are briefly summarized here. The CLEF simulation was run with the GADGET2 N-body/SPH code (Springel, 2005) and followed the evolution of large-scale structure within a box of comoving length, $200h^{-1}$Mpc. The following cosmological parameters were assumed: $\Omega_{\text{m}} =$

$0.3; \Omega_\Lambda = 0.7; \Omega_{\text{b}} = 0.0486; h = 0.7; n_{\text{s}} = 1; \sigma_8 = 0.9$. Here the value of the Hubble constant is written as $100 \, h \, \text{km s}^{-1} \, \text{Mpc}^{-1}$ and σ_8 is the rms mass fluctuation at the present epoch in a sphere of radius $8 \, h^{-1}$Mpc. The number of particles was set to 428^3 for each of the gas and dark matter species, thus determining the particle masses to be $m_{\text{DM}} = 7.1 \times 10^9 h^{-1} \text{M}_\odot$ and $m_{\text{gas}} = 1.4 \times 10^9 h^{-1} \text{M}_\odot$ respectively. The equivalent Plummer softening length was set to $20 \, h^{-1}$ kpc and held fixed at all times in comoving co-ordinates. Pressure forces were calculated using the standard GADGET2 entropy-conserving version of SPH with an artificial viscosity to convert kinetic energy into thermal energy where the flow was convergent. The gas could cool radiatively assuming a fixed metallicity, $Z = 0.3Z_\odot$. Cold ($T < 10^5$K) gas with $n_{\text{H}} > 10^{-3} \text{cm}^{-3}$ either formed stars or was heated by an entropy, $\Delta S = 1000 \, \text{keV cm}^2$. This choice was determined stochastically by selecting a random number, r, from the unit interval and heating the particle if $r < 0.1$, i.e. a 10 per cent probability of being heated. This high level of feedback was necessary to reproduce the observed excess entropy in clusters (see Kay et al. (2007) for further details).

To select the cluster sample, we first consider all clusters at $z = 0$ with X-ray temperatures, $kT > 2$ keV; this produces 95 objects, with virial masses, $M_{\text{vir}} > 1.3 \times 10^{14} h^{-1} \text{M}_\odot$ (correspondingly, $> 15,000$ dark matter particles). We then select those clusters with 3D substructure statistic, $s < 0.05$. The substructure statistic (Thomas et al., 1998) measures the displacement of the centre of mass from the potential minimum of the cluster (taken to be its centre), relative to r_{500}, which is the scale radius within which the mean total density is 500 times the critical density. By making this cut, we therefore exclude all clusters that show significant signs of dynamical activity, i.e. major mergers.

V06

The second sample is a subsample of the one presented in Valdarnini (2006) which we refer to as V06. These simulations assumed a concordance flat ΛCDM with the same cosmological parameters as for the CLEF simulation.

The simulation ensemble of galaxy clusters was constructed according to a procedure described in (Piffaretti & Valdarnini, 2008). Here we briefly summarize the most important aspects. The hydrodynamic simulations were run using an entropy-conserving multistep TREESPH code for a sample of 153 clusters spanning a range from $\simeq 1.5 \times 10^{15} h^{-1} M_\odot$ down to $M_{vir} \simeq 1.5 \times 10^{14} h^{-1} M_\odot$. The initial conditions ($z_{in} = 49$) were extracted from a set of purely N-body cosmological simulations in which clusters of galaxies

were identified from the particle distribution at $z = 0$ using a friends–of–friends algorithm. In order to investigate the effect of the implemented gas processes on the energy equipartition between gas end dark matter particles, we performed both adiabatic and radiative simulations. The radiative simulations are of course more realistic than the adiabatic ones, because they additionally take into account radiative cooling, star formation, energy and metal feedback (Valdarnini, 2003). More details concerning the simulation technique and the implementation of physical processes of the gas are given in Valdarnini (2006).

In order to avoid contamination from dynamically perturbed clusters, we select the 20 most relaxed objects at $z = 0$. The selection is based on the power ratio method, which measures the amount of substructure in X-ray surface brightness maps. The map sources a pseudo-potential which is expanded in plane harmonics, and the ratio of the third coefficient to the zeroth is a measure of substructure. More details are given in Piffaretti & Valdarnini (2008).

The temperature relation

We examine the temperature relation eq. (B.2) in the two simulated samples by comparing the gas mass-weighted temperature to the rescaled dark matter velocity dispersion. The resulting κ-profiles are shown in fig. B.1 and clearly $\kappa \approx 1$ for both samples. Since we apply somewhat different criteria to select the two simulation samples, it is not surprising to find slightly different profiles. This indicates a systematic uncertainty of ± 0.1 in the simulated κ profiles. The kinetic energy associated with bulk motions of both gas and dark matter particles is at most a few percent of the thermal energy within $2\,r_{2500}$, outside which bulk motion is not negligible. This is in agreement with what was found in Ascasibar (2003). Due to the standard problem of limited force resolution, the simulations do not probe the innermost region reliably. Therefore we exclude data inside a cutoff radius ($56\,h^{-1}$ kpc for CLEF, $0.1\,r_{2500}$ for V06), which means we cannot estimate κ in the central region where gas physics can make a significant impact.

The adiabatic version of the V06 sample exhibits a larger median κ-profile which is constant about 1.2 within r_{2500} and increases steadily to 1.4 at r_{200}. This is comparable with the earlier work of Rasia et al. (2004), where the specific energy of dark matter was seen to be larger than that of the gas by 20–30% in adiabatic simulations.
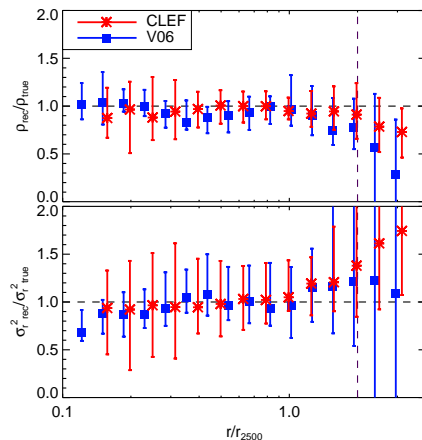

Fig. B.2: Comparison of estimated and true values of the physical quantities involved in determining the velocity anisotropy β in our simulations. Top, the ratio of the reconstructed total density to the true; bottom, the ratio of the reconstructed σ_r^2 to the true one. Error bars show the 1σ percentiles taken over the sample members.

Reconstructing the velocity anisotropy

In order to test the method outlined above for determining β, we reconstruct the anisotropy profiles observed in the simulated samples. Here, we assume $\kappa = 1$ for all radii even though we expect deviations at small radii. First we derive the integrated mass profile $M(r)$ for each cluster assuming hydrostatic equilibrium (B.8), and from that the total density profile. The numerical derivatives involved are calculated using three-point quadratic interpolation. The estimated density profile, shown in fig. B.2 (top), displays a satisfactory agreement with the actual density profile for both the CLEF and V06 samples. The only exception is at the outermost radii above r_{2500} where the density is underestimated. Next, we calculate the radial velocity dispersion eq. (B.11) by interpolating the integrand from $r = 0$ using a four-point natural spline interpolation. We compare the resulting radial velocity dispersion with the actual in fig. B.2 (bottom) which shows that there is good agreement except for the deviation at large radii already seen in the density profiles.

Finally we determine the velocity anisotropy parameter β. We find similar results whether we calculate β_{Je} or β_{tr}, however the temperature relation yields less noisy results. The median velocity anisotropy profiles
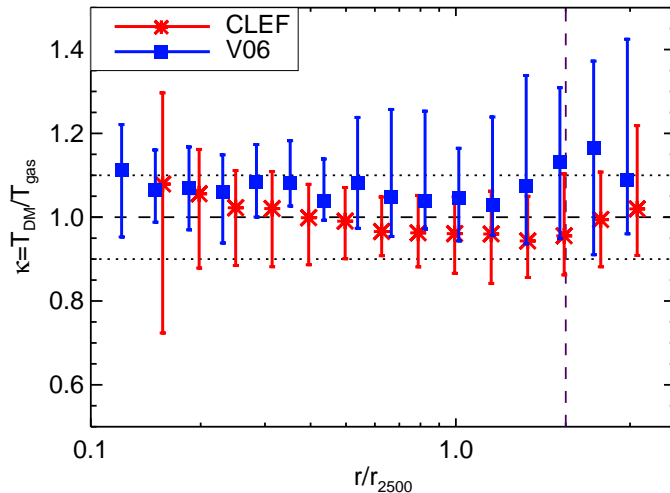
Fig. B.1: Radial profile of $\kappa = T_{\mathrm{DM}}/T_{\mathrm{gas}}$ for the samples of clusters obtained from the CLEF and V06 simulations comprising 67 and 20 clusters, respectively. We plot the median and 1σ percentiles taken over each sample. The vertical line indicates the largest radius of the observational data sample, while the vertical lines indicate the mean and standard deviation of the κ-profile that we use in the fiducial analysis. Note that, for the CLEF sample, only eight clusters contribute to the innermost bin.

are shown in fig. B.3 together with the median actual profile. The reconstructed profile tracks the actual anisotropy well in the inner parts but overestimates β in the outer parts. There is also considerable noise in the results.

In order to understand the origin of the deviations at large radii and the significant scatter in our results, we investigate the systematics of the analysis, as applied to the CLEF sample (similar conditions hold for the V06 sample). First, we substitute the dark matter density estimated from hydrostatic equilibrium with the true density. The β-profiles calculated on this basis are shown in the top panels of fig. B.4. The agreement between the estimated and actual β is considerably improved, and the error bars are significantly reduced. This clearly indicates that, in the fiducial analysis, the numerical derivatives necessary to estimate ρ_{DM} are responsible for the large error bars. Since we do not want to do any parametrized modeling of the gas properties, the numerical derivatives are liable to amplify noise and induce systematic deviations in the outermost bin, where the quantities are only constrained to one side. Additionally, this explains why β_{Je} appears more noisy in the fiducial analysis since an additional derivative must be calculated. The test also

shows that there is a deviation from hydrostatic equilibrium at large radii which is part of the reason why β is overestimated. As a second test, we additionally use the true three-dimensional velocity dispersion instead of using the temperature relation. This yields further improvement as to how well the reconstructed β tracks the true one, as shown in the bottom panels of fig. B.4. This implies that it is possible to get the correct scale of the radial velocity dispersion, calculated as an integral from the center, despite the lack of resolved data in the inner radii. We note that, with respect to observational data, the tests we apply here can possibly be utilized in the future, e.g. with accurate density profiles inferred from gravitational lensing, and with more detailed knowledge of κ from improved simulations. We conclude that the numerical simulations provide proof that our method is robust and that it is indeed possible to infer the β-profile despite lacking knowledge of κ in the center.

B.5   Observations

Next we apply our analysis to observational data from which the radial gas density and temperature profiles are recovered. This is done strictly using non-
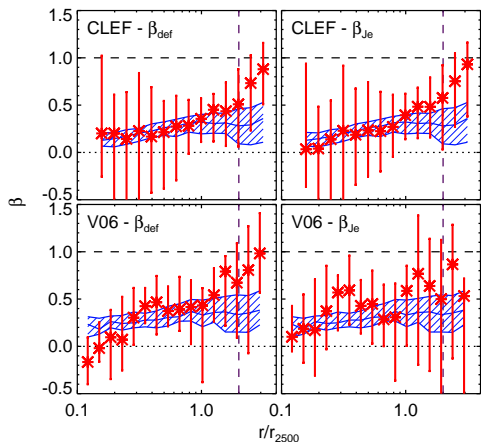
Fig. B.3: Reconstructed velocity anisotropies for the simulated samples. The hatched bands show the actual β-profiles of the samples. Error bars show the 1σ percentiles taken over the sample members.
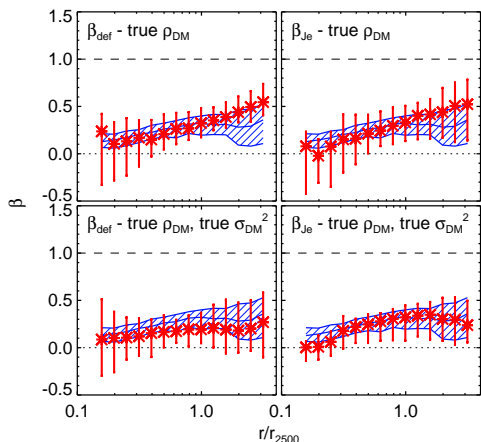

Fig. B.4: Systematics of the reconstruction of the β profiles for the CLEF simulation. Again, β is recovered both from eq. (B.12) (left) and eq. (B.13) (right). The true dark matter density is substituted for the estimated, and in the bottom panels we additionally use the true total velocity dispersion instead of estimating it from $T_{\mathrm{DM}} = \kappa T_{\mathrm{gas}}$.

parametric methods, i.e. no modeling of the gas properties is involved. Our data consists of the deprojected density and temperature profiles of two samples of clusters at low and intermediate redshift, respectively. The deprojected profiles were obtained from X-ray data analysis published in earlier work (details below). We consider clusters which appear relaxed and close to spherical, and for which sufficient spectroscopic data are available to analyze several annuli, so that the radial variations of the gas density and temperature are resolved with good statistics.

The first set of eleven clusters at low redshift is based on X-ray data from *XMM-Newton* of the clusters: A262, A496, A1795, A1837, A2052, A4059, Sérsic 159−3, MKW3s, MKW9, NGC533, and 2A0335+096. These objects are highly relaxed cool-core (CC) clusters selected as to match the requirements described above. The objects were part of the sample analyzed in Kaastra et al. (2004) (see this paper for an extensive presentation of the data analysis), in which deprojected radial temperature and density profiles were derived from spatially resolved spectroscopy. We adopt the radial bin selection of Piffaretti et al. (2005) in order to ensure a robust determination of gas temperature and density for the full radial range. Note that data for A2052 and Sérsic 159−3 were also used in the analysis by Hansen & Piffaretti (2007) where a constant velocity anisotropy was assumed.

The other set of five intermediate redshift X-ray galaxy clusters (RXJ1347.5, A1689, A2218, A1914, A611) is from the *Chandra* sample analyzed in Morandi et al. (2007). The radial deprojected temperature and density profiles were retrieved through resolved spectral analysis in a set of annuli, selected to collect at least 2000 net counts, by assuming spherical geometry and by using the definition of 'effective volume' (see Morandi et al. (2007) for further details).

B.6 Results

We determine the dark matter velocity anisotropy profile $\beta(r)$ of each cluster according to the recipe in section B.3 using a Monte Carlo method. For each radial bin the deprojected gas temperature and density are sampled assuming Gaussian uncertainties, i.e. a random number is chosen from a Gaussian distribution with mean equal to the estimated temperature or density and a standard deviation equal to the uncertainty of the estimate. The bins are sampled independently. The parameter κ is also sampled for each bin, assuming a Gaussian distribution with a mean of 1 and a standard deviation of 0.1, which is a reasonable value according to the simulations. The sampled profiles are used to reconstruct the total mass through (B.8), and then the
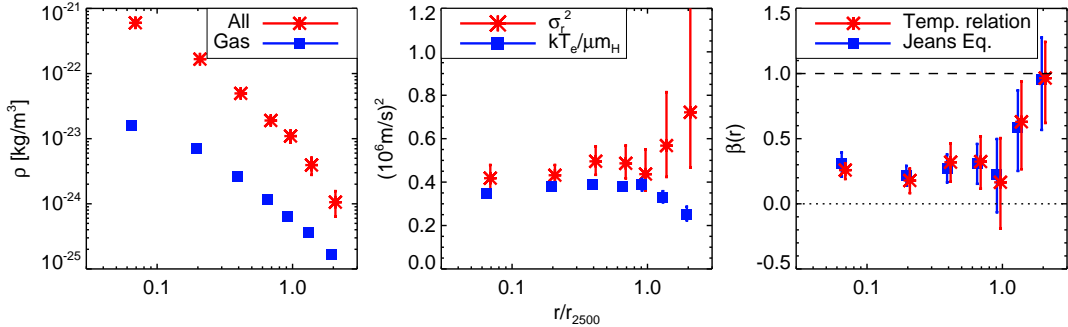
Fig. B.5: Three steps in the calculation of the velocity anisotropy for Sérsic 159−3. Left, the inferred total density; center, the radial velocity dispersion; right, the β-profiles. The gas density and temperature profiles are also shown. The scale radius for this cluster is estimated to be $r_{2500} = 337 \pm 13\,\mathrm{kpc}$. Error bars indicate the propagated statistical uncertainties on the ICM temperature and density profile, taken as the 1σ percentiles of 1000 Monte Carlo samples. This is unlike in the previous figures where the error bars indicate the spread over the numerically simulated samples. In the right panel, the radial positions of β_{tr} and β_{Je} have been offset slightly for clarity.

integrand, the radial velocity dispersion, and the velocity anisotropy are calculated in each bin. The sampled set of profiles is accepted only if the temperature and density as well as the reconstructed dark matter density and radial velocity dispersion are all non-negative in all bins. For each sample, we also estimate the scale radius r_{2500} and the mass M_{2500} contained within that radius. Table B.1 summarizes the properties of the clusters in our sample.

The numerical methods for calculating derivatives and integrals are the same as for the simulated samples, i.e. three-point quadratic interpolation is used for derivatives and four-point spline interpolation is used for the integral in eq. (B.11). The integration results are stable to using two-point linear, three-point quadratic, or four-point least squares quadratic interpolation instead.

Individual steps of the reconstruction are shown in fig. B.5 for the cluster Sérsic 159−3, and the deprojected input data are also displayed. We always plot the median and 1σ percentiles since spurious outliers in individual Monte Carlo samples can bias the mean and standard deviation significantly. The size of the error bars is mostly determined by the uncertainties of the temperatures, to a lesser degree by the uncertainties of the ICM densities, and it is virtually insensitive to the 10% variation assumed for the κ-profile.

As can be seen in the right panel of fig. B.5, the agreement between β_{tr} and β_{Je} indicates that numer-

ical effects associated with the integration and differentiations are small. On the other hand, β becomes unphysically large in the outermost bins since the reconstructed radial velocity dispersion for some samples becomes greater than the total velocity dispersion. This result is similar to that found in the blind analysis of the simulation samples. As discussed above, this behaviour is mainly due to a deviation from hydrostatic equilibrium of the gas, and to a lesser degree to edge effects making the numerical differentiations less well determined in the outermost bin. It is possible that systematic uncertainties in the input data or radial variations in κ for individual clusters also play a role. In principle, we could impose $\sigma_r^2 < \sigma^2$, thereby forcing $\beta < 1$, as another physical condition on each Monte Carlo sample, but we prefer not to do so in order to have a consistency check.

We repeat the data analysis for the remaining 15 clusters of our sample and the resulting velocity anisotropy profiles are shown in fig. B.6. In almost all cases the anisotropy is small in the inner radial bins and increases to between 0.5 and 1.0 in the outer parts. There is good agreement between the two derivations of β for all clusters, indicating that numerical issues are under control.

Since the qualitative behaviour of the velocity anisotropy profiles are similar, we combine all our data into a single 'stacked' profile, shown in fig. B.7. In the region where direct comparison is possible, the mea-
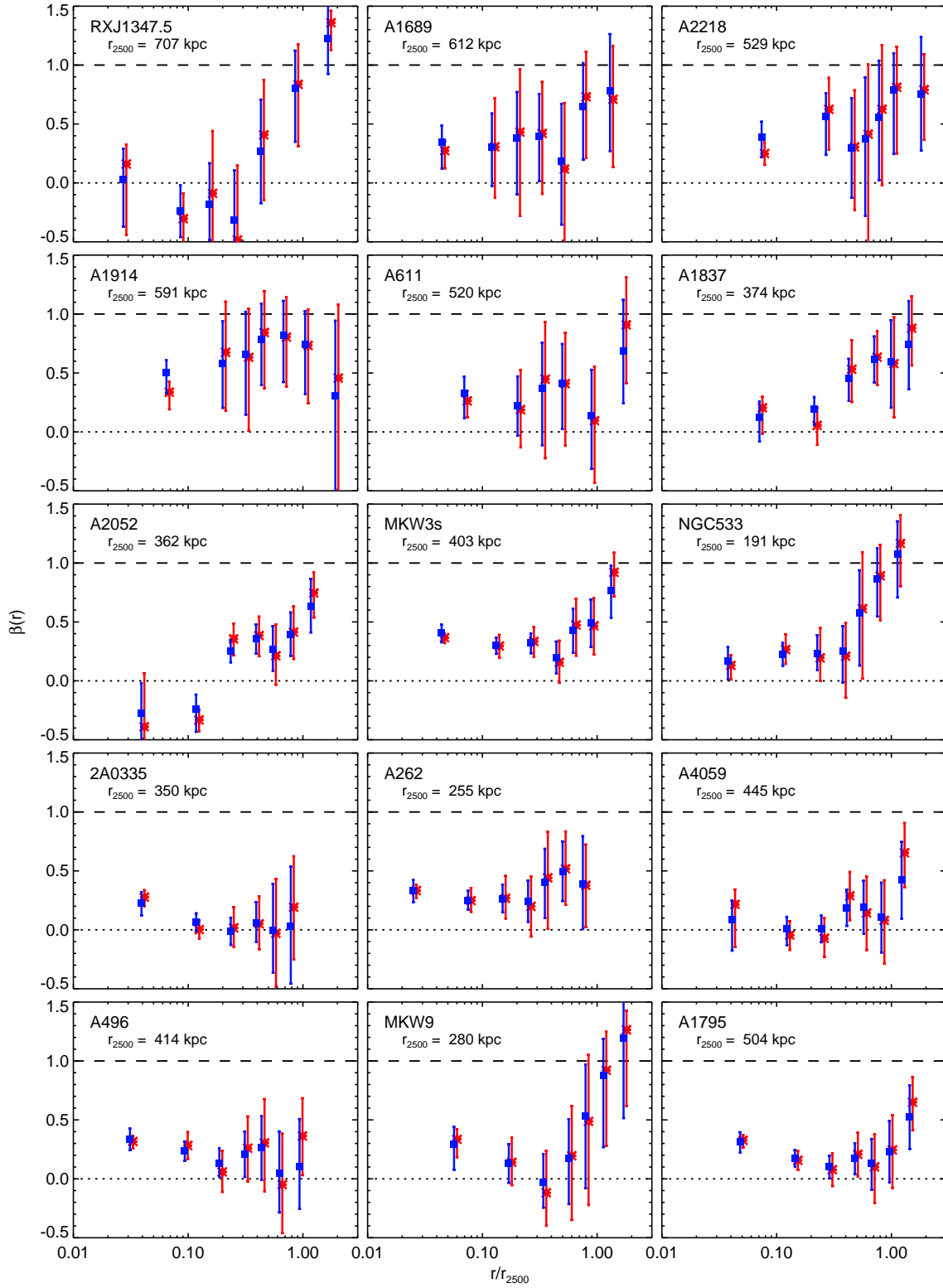
Fig. B.6: Median velocity anisotropy profiles for the remaining 15 clusters of our sample. The estimated scale radii are also shown, and the symbols are the same as in fig. B.5.

sured stacked profile is very similar to the reconstructed β profiles for the simulation samples (the green line), and within r_{2500} there is also agreement with the actual velocity anisotropy of the simulation samples (hatched band). The velocity anisotropy is likely overestimated outside r_{2500} for the same reason as for the simulated samples, i.e. deviation from hydrostatic equilibrium, but the effect appears to be even stronger for the observational data. Interior to the cut-off radius of the numerical simulations, the observations tend to $\beta \sim 0.3$. This is somewhat surprising since numerical simulations at all mass scales generally have very little anisotropy towards the center of structures. While we cannot exclude the possibility that cluster halos are anisotropic even at low radii, our result can also be explained by the neglected stellar contribution $\rho_\star$ to the total mass density. To first order, this contribution enters our analysis in the Jeans equation through the estimated dark matter density $\widetilde{\rho}_{DM} = \rho_{DM} + \rho_\star$. In terms of $\delta_\star = \rho_\star/\rho_{DM}$, the Jeans equation becomes

$$\sigma_r^2 \left(\frac{d \ln \widetilde{\rho}_{DM}}{d \ln r} + \frac{d \ln \sigma_r^2}{d \ln r} + 2\beta - \frac{d \ln(1 + \delta_\star)}{d \ln r} \right)$$
$$= -\frac{GM(r)}{r} \quad \text{(B.14)}$$

where the slope of $(1 + \delta_\star)$ is negative since the stellar density must fall off faster than the dark matter density. This means that we overestimate the velocity anisotropy in the central region by not accounting for the stellar mass. Indeed, if we assume that 50% of the total mass in the innermost bin is made up of stars, the velocity anisotropy in the two innermost bins becomes consistent with zero. There is also a second order correction through the appearance of $\widetilde{\rho}_{DM}$ in eq. (B.11) instead of ρ_{DM}, but this correction must be small since the density contributes to both the integrand and the normalization factor.

Finally, we investigate how the assumed shape of the κ-profile affects our results. We try five different profiles as functions of $x = r/r_{2500}$ with noise added as before, and calculate the velocity anisotropy profiles for each. The κ-profiles are chosen so as to mimick either the effects of gas radiative cooling or AGN heating in the central regions, or to check the results if the dark matter is generally hotter or cooler than the gas. The radially varying profiles we try are extreme cases of the simulation profiles, fig. B.1. Typically, the result is that the β-profile is shifted in the central regions while the outer regions are largely unaffected, as shown in fig. B.8. This analysis confirms that there is a significant velocity anisotropy at large radii, independent of the specific assumptions about the temperature relation.

B.7   Summary and discussion

In this paper, we have presented a non-parametric method to infer the velocity anisotropy of dark matter in clusters of galxies from the observable temperature and density of the intracluster medium. We assume that the intracluster medium has the same specific energy as the dark matter, and we investigate the validity of this assumption in two different cosmological simulations of the formation of galaxy clusters. Both confirm the simplest possible form of the relation, namely $T_{DM} \approx T_{gas}$ in the radial range which is resolved.

We have tested how well our method can reconstruct the actual velocity anisotropy in the simulated clusters, and we have found good agreement between the two, although the reconstruction is sensitive to systematic biases connected with deviations from hydrostatic equilibrium.

We have applied our method to the radial ICM density and temperature profiles of 16 galaxy clusters based on *Chandra* and *XMM-Newton* X-ray data. The shape of the velocity anisotropy profiles is always consistent with that seen in simulations, which tends to zero at the innermost radius where the temperature relation is calibrated. It then increases to about 0.5 at r_{2500} and even larger in the outer regions. The same is true of the fiducial analysis applied to simulated data and is likely caused by a deviation from hydrostatic equilibrium outside r_{2500}. We also find a significant anisotropy even if we assume radially varying κ-profiles, such as can be expected given the strong gas cooling and AGN heating in the core of many clusters, or if we assume $\kappa \neq 1$. The agreement between the observed velocity anisotropy and that predicted in numerical simulations shows that we are beginning to understand also the dynamical aspects of dark matter in halos.

In the innermost radial bins we measure a rather large anisotropy, but this is most likely an overestimation due to the neglect of the stellar mass in the center. This can be used as a means to estimate the stellar mass profile of galaxy clusters if one assumes that the velocity dispersion to be isotropic in the central regions. Similarly, our method may be used as a general test of whether a cluster is relaxed. A reconstructed velocity anisotropy which deviates significantly from the simulated profiles would be a strong hint that the data do not support the assumption of hydrostatic equilibrium.

The inferred velocity anisotropy profiles are significantly different from zero which means that the collective behaviour of dark matter is unlike that of baryonic particles in gases. This shows that dark matter is effectively collisionless on the timescale of $\tau \sim 10^9$, the dynamical timescale of galaxy clusters. By taking typical values at $\sim 0.3\, r_{2500}$ and allowing only a few
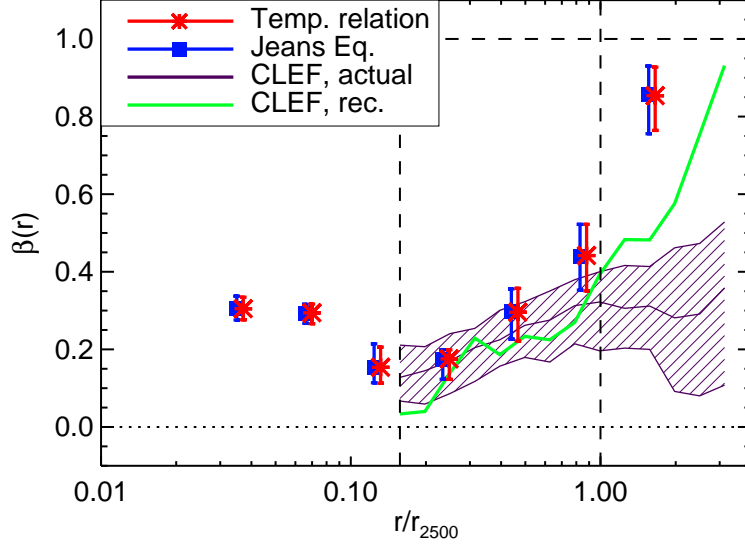
Fig. B.7: Median velocity anisotropy profile of all 16 clusters in our dataset. In this case the error bars denote the 1σ percentiles of the combined probability density of all clusters within the bin. The actual and reconstructed β-profiles from the simulations are also shown. The left vertical line is the innermost radius probed in the CLEF simulations and the right vertical line shows, roughly, the onset of significant deviations from hydrostatic equilibrium in the simulations, see fig. B.2.

Tab. B.1: Properties of our cluster sample

| Cluster	z	r_{2500}/kpc	$M_{2500}/M_\odot$
A262	0.015	256 ± 28	$(2.7 \pm 0.8) \times 10^{13}$
A496	0.032	398 ± 10	$(1.0 \pm 0.2) \times 10^{14}$
A1795	0.064	504 ± 22	$(1.9 \pm 0.2) \times 10^{14}$
A1837	0.071	374 ± 26	$(8.0 \pm 1.7) \times 10^{13}$
A2052	0.036	362 ± 11	$(6.7 \pm 0.6) \times 10^{13}$
A4059	0.047	445 ± 21	$(1.3 \pm 0.2) \times 10^{14}$
Sérsic 159−3	0.057	337 ± 17	$(5.7 \pm 0.8) \times 10^{13}$
MKW3s	0.046	404 ± 14	$(9.5 \pm 0.9) \times 10^{13}$
MKW9	0.040	279 ± 44	$(3.2 \pm 1.5) \times 10^{13}$
NGC533	0.018	191 ± 15	$(9.7 \pm 2.2) \times 10^{12}$
2A0335+096	0.034	350 ± 40	$(6.9 \pm 2.5) \times 10^{13}$
A611	0.29	519 ± 52	$(2.5 \pm 0.6) \times 10^{14}$
A1689	0.18	609 ± 4	$(3.5 \pm 0.7) \times 10^{14}$
A1914	0.17	590 ± 44	$(3.3 \pm 0.8) \times 10^{14}$
A2218	0.18	535 ± 51	$(2.5 \pm 0.7) \times 10^{14}$
RXJ1347.5-1145	0.45	710 ± 60	$(7.3 \pm 1.4) \times 10^{14}$
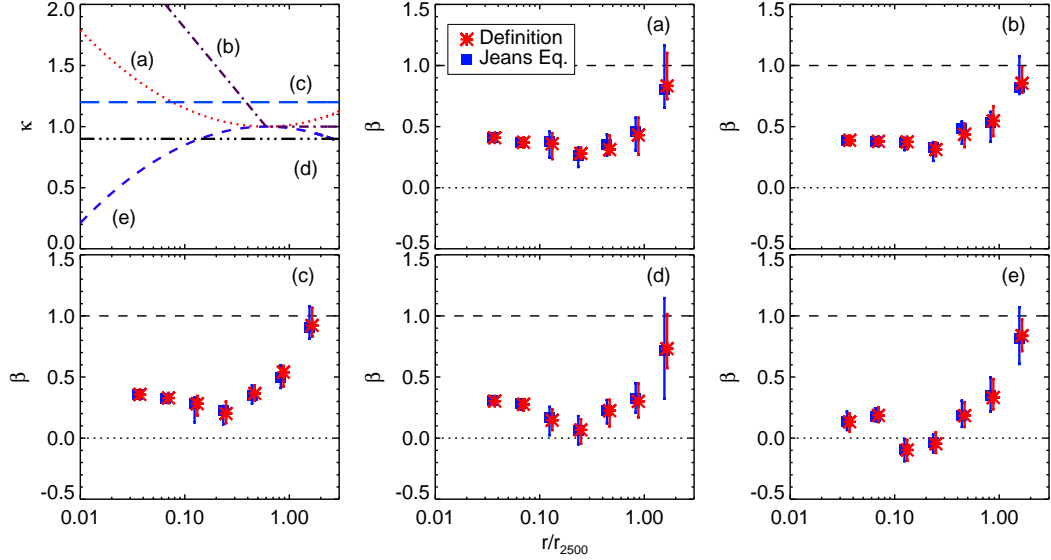
Fig. B.8: The effect of assuming different κ-profiles on the stacked velocity anisotropy profile. Top left, the five κ-profiles. Others, the resulting sample averaged β-profiles calculated assuming the numbered κ-profile. In all cases, β is greater than zero in the outer parts.

scatterings within the time τ, this corresponds to an order–of–magnitude upper limit to the scattering cross-section of roughly $\sigma/m = (\rho_{\mathrm{DM}}\tau v)^{-1} \lesssim 1\,\mathrm{cm^2 g^{-1}}$. This limit is similar to what has been found for merging clusters (Markevitch et al., 2004; Bradač et al., 2008), and within an order of magnitude of the scattering cross-section for self-interacting dark matter proposed in Spergel & Steinhardt (2000).

We emphasize that improvements to the numerical simulations in the near future will improve our understanding of the κ profile and hopefully track the impact of radiative effects in the center. We also hope that improved understanding of deviations from hydrostatic equilibrium will allow us to estimate how large the suspected bias at large radii is. On the observational side, the main problem at present is the uncertainty in the temperature profile. Improvements can be expected both with regards to the deprojection analysis and the amount of data available. Obviously, there is also the possibility of including a kinematical analysis of the galaxy clusters in our method.

C. PAPER III: A DETAILED STATISTICAL ANALYSIS OF THE DARK MATTER MASS PROFILES OF GALAXY CLUSTERS

Ole Host, Steen H. Hansen

Dark Cosmology Centre, Niels Bohr Institute, University of Copenhagen, Juliane Maries Vej 30, DK-2100 Copenhagen, Denmark

Abstract

The distribution of dark matter in the halos that surround galaxies and galaxy clusters has been probed observationally, theoretically, and in numerical simulations. Yet there is still confusion about which of several suggested parameterized models is the better representation, and whether these models are truly universal. We use the observed temperature and density profiles of the intracluster medium of 11 relaxed galaxy clusters to investigate mass models for the dark matter halo using a thorough statistical analysis. We make careful comparisons between two- and three-parameter models, including the issue of a universal third parameter. We find that, of the two-parameter models, the NFW is still the best representation, but we also find moderate statistical evidence that a generalized three-parameter NFW model with a freely varying inner slope is preferred, despite penalizing against the extra degree of freedom. There is a strong indication that this inner slope needs to be determined for each cluster individually, some clusters have central cores and others have steep cusps. This implies that x-ray observations do not support the idea of a universal inner slope, but perhaps show a hint of a dependence with redshift or mass. The mass-concentration relation of our sample is in reasonable agreement with the latest predictions based on numerical simulations.

C.1   Introduction

The potential of gravitationally bound structures in the Universe, ranging in size from dwarf galaxies to galaxy clusters, is sourced by a composite mass distribution of dark matter, baryonic matter in gas form, and collapsed objects such as stars in galaxies and galaxies in clusters. The investigation of these mass distributions entails a number of questions: what is the shape of the distributions? Is it universal across ten magnitudes of mass and at all redshifts? Does it depend on cosmology or on the merger history of the individual halos? Since the dominant component of relaxed structures is dark matter, much focus has been aimed at dark matter-only halos.

There is little theoretical understanding of the distribution of matter in a dark matter halo. The main developments have been found through numerical simulations of the formation of structure in the universe within a given cosmological model. Advances have been achieved through the improvement of numerical codes as well as the increase of raw computing power on one hand and a more refined understanding of which questions that need to be answered on the other. Perhaps the most fundamental idea that has come out of the numerical approach is that relaxed halos are (nearly) universal in many respects, including the distribution of matter (Navarro et al., 1997; Taylor & Navarro, 2001) and the dynamical structure (Bullock et al., 2001a; Hansen & Moore, 2006). However, the simulations have not been able to reach agreement about the exact behavior of the profiles in the innermost regions, where the limited force resolution of simulations sets a lower limit to the radial range that can be probed. Various authors claim that the logarithmic slope of the density profile reaches a value between -1 and -1.5, perhaps dependent on mass or merger history, and there is also discussion whether the inner slope is actually universal or not (Moore et al., 1998; Klypin et al., 2001; Navarro et al., 2004; Fukushige et al., 2004; Merritt et al., 2006; Graham et al., 2006; Gao et al., 2008). A further complication arises when the simulations are compared with observations since the gravitational potential of the baryonic component, which is very time consuming to model in the simulations, cannot be neglected in the center. This complication can in principle both change the slope of the dark matter profile as well as alter the total mass profile (Blumenthal et al., 1986; El-Zant et al., 2001; Gnedin et al., 2004; Sommer-Larsen & Limousin, 2009).

Theoretical efforts are hampered by the fact that, even under the strongest simplifying assumptions, there are not enough constraints to obtain unique solutions to the collisionless Boltzmann equation (Binney & Tremaine, 1987) which governs a dark matter structure. Instead, one can take phenomenological input from numerical simulations such as the density profile itself, the pseudo-phase space density (Taylor & Navarro, 2001; Dehnen & McLaughlin, 2005), or the density slope-velocity anisotropy relation (from which Hansen & Stadel (2006) predict an inner slope of 0.8), and implement this into a Jeans equation analysis to predict the consequences of the 'inspired guess' (see also Zait et al. (2008) and references therein). Alternatively one can attempt to model the formation history of the halo including major mergers and steady accretion (e.g., Ryden & Gunn (1987); Ascasibar et al. (2004); Salvador-Solé et al. (2007); Del Popolo (2009), and references therein). While these approaches typically yield results in rough agreement with simulations, the modeling can also explore the physical connection between the static and dynamic properties of the halo as well as offer constrained extrapolations which are not accessible in simulations.

Observationally, there is a strong discrepancy between the numerical results and the inferred mass distributions in dwarf and low surface brightness galaxies, which are much shallower than predicted, the so-called cusp/core-problem (see, e.g., Salucci et al. (2003); Spekkens et al. (2005); Gilmore et al. (2007)). At the opposite end of the mass spectrum, galaxy clusters are typically found to be in rough agreement with the cuspy numerical simulations, but with even greater scatter for the inferred inner slope. There is also significant discussion about the type of model and number of parameters that are necessary in order to obtain an acceptable description of the data. One common method is based on mass modeling through weak or strong gravitational lensing, which can yield results which are in good agreement with numerical simulations (Broadhurst et al., 2005; Comerford et al., 2006; Limousin et al., 2008; Richard et al., 2009), but also profiles that are significantly shallower (Sand et al., 2004, 2008). Another method is based on x-ray observations of the intracluster medium (ICM) which is supported against gravitational collapse by its own pressure. Again, authors find a range of inner slopes (Ettori et al., 2002; Lewis et al., 2003; Zappacosta et al., 2006; Saha & Read, 2009). For both lensing and x-ray studies most authors focus on only one or a few clusters, which of course makes it more difficult to assess the universality of the profiles on an observational foundation.

In the present work we take a sample of 11 highly relaxed clusters and use the measurements of the x-ray emitting gas to infer model-independent mass profiles. We then compare with a number of different models that have been applied as mass profiles in the literature, focusing on three key questions: Which parame-

terized model is the most successful? How many free parameters are needed to describe the data adequately? Is there evidence for a universal inner slope/shape-type parameter? We answer these questions using a detailed statistical analysis based on Bayesian inference where we use the Bayesian evidence (or marginal likelihood) to make judgments about which model is preferred by the data.

C.2 Density profile models

Most models that are used for modeling the mass distribution in halos have been proposed or introduced as fitting formulae applied to the halos found in the numerical simulations. Hence these models are not theoretically well-founded but rather form a basis on which the predictions of numerical simulations can be compared with observations. Almost all of these models have two free parameters which determine the mass scale and the spatial extent of the halo, and these two parameters are specific to each halo. Some models have one or more additional parameters which determines the shape of the profile, and which may or may not be universal. Here we consider a number of two- and three-parameter models.

A whole class of models are 'double power-laws' which asymptote to power laws at very small and very large radii. These models can conveniently be summarized in Hernquist's (α, β, γ) parametrization (Hernquist, 1990; Zhao, 1996),

$$\rho(r) = \rho_0 \left(\frac{r}{r_s}\right)^{-\alpha} \left[1 + \left(\frac{r}{r_s}\right)^\gamma\right]^{-\frac{\beta-\alpha}{\gamma}}, \qquad \text{(C.1)}$$

where ρ_0 and r_s are scaling constants to be determined for each halo individually. The inner power-law slope is α and the outer slope is β, while the width of the transition region is controlled by γ. We consider four such two-parameter profiles: the NFW (Navarro et al., 1997), the Dehnen-McLaughlin (Dehnen & McLaughlin, 2005), the Hernquist, and the Moore profile (Moore et al., 1998). The properties of these models are summarized in table C.1.

We also consider three three-parameter models: Two are simply generalized NFW profiles where, in the first case, we allow the inner slope α to vary. The motivation for this slopeNFW model was already apparent from the introduction. The second case, transNFW, is also a generalization of the NFW where now the transition parameter γ is free. Such a profile can mimic a steeper inner slope by pushing the inner power law behavior closer to the center. The third profile is the Sérsic (or

Einasto) profile (Sérsic, 1963; Einasto, 1969),

$$\rho(r) = \rho_s \exp\left(-2n\left[\left(\frac{r}{r_s}\right)^{1/n} - 1\right]\right), \qquad \text{(C.2)}$$

where the parameter n determines the shape of the profile. For $n = 4$ the de Vaucouleurs' law describing the surface brightness of elliptical galaxies is recovered. The shape parameter is sometimes given as $\alpha_s = n^{-1}$. Recently, the Sérsic profile has been claimed to provide a better fit than the NFW to Milky Way-sized haloes formed in numerical simulations, and, interestingly, with a shape parameter that varies significantly from halo to halo (Salvador-Solé et al., 2007; Navarro et al., 2008).

We map the scale radius r_s and scale densities ρ_s or ρ_0 of each model to the model-independent parameters r_{-2} and ρ_{-2}, which are the radius at which the slope of the density profile is -2 and the density at that radius, respectively. This mapping makes comparison of the models easier and enables identical priors to be used in the statistical analysis in all models.

C.3 Data analysis

We revisit the sample of 11 highly relaxed, low redshift ($z < 0.1$) galaxy clusters observed with *XMM-Newton* which we already used in Host et al. (2009) to measure the dark matter velocity anisotropy profile for the first time (see also Hansen & Piffaretti (2007)). The members of this sample were selected to appear close to round on the sky and not have strong features in the temperature and density profiles. The spectral analysis and deprojection of the x-ray data was carried out in Kaastra et al. (2004) and Piffaretti et al. (2005). The deprojection method was non-parametric, i.e. without any parametric modeling of the radial temperature or density profiles. The outcome, and the starting point for the present analysis, was estimates of the ICM temperature T_i and electron number density $n_{e,i}$ with associated uncertainties in six or seven radial bins, for each of the clusters.

Assuming hydrostatic equilibrium, the ICM gas traces the gravitational potential according to (Cavaliere & Fusco-Femiano, 1978)

$$\frac{k_B T}{\mu m_H} \left(\frac{d \ln n_e}{d \ln r} + \frac{d \ln T}{d \ln r}\right) = -\frac{G M_{\text{tot}}(r)}{r}, \qquad \text{(C.3)}$$

where $\mu = 0.6$ is the mean molecular weight of the ICM. Almost all of the cluster mass resides in dark matter and the ICM, and therefore the dark matter mass distribution can be determined through $M_{\text{DM}}(r) = M_{\text{tot}}(r) - M_{\text{ICM}}(r)$. The ICM mass profile is given straight-forwardly by the density $\rho_{\text{ICM}} = \mu m_H n_e$.

Tab. C.1: Density profile models

Model	(α, β, γ)	r_{-2}/r_s	ρ_{-2}/ρ_0	$\mu(x = r/r_s)$
NFW	$(1, 3, 1)$	1	$\frac{1}{4}$	$\ln(1+x) - x/(1+x)$
D&M	$(\frac{7}{9}, \frac{31}{9}, \frac{4}{9})$	$\frac{121}{169}$	0.0338	$\frac{9}{20}(1 + x^{4/9})^{-5}$
Hernquist	$(1, 4, 1)$	$\frac{1}{2}$	$\frac{16}{27}$	$x^2/[2(1+x)^2]$
Moore	$(\frac{3}{2}, 3, 1)$	$\frac{1}{2}$	$\frac{8}{3\sqrt{3}}$	$2\sinh^{-1}(\sqrt{x}) - 2\sqrt{x/(1+x)}$
slopeNFW	$(\alpha, 3, 1)$	$2 - \alpha$	$(2-\alpha)^{-\alpha}(3-\alpha)^{\alpha-3}$	-
transNFW	$(1, 3, \gamma)$	1	$\frac{1}{4}$	-
Sérsic	-	1	1	$8^{-n}e^{2n}n^{1-3n}\gamma(3n, 2nx^{1/n})$

NOTE. — Properties of the density profiles that we consider, including the (α, β, γ) specification, the relations between (r_{-2}, ρ_{-2}) and (r_s, ρ_0), and the shape $\mu(r)$ of the mass profile $M(r) = 4\pi r_s^3 \rho_0 \mu(r)$, if analytical. $\gamma(a, x)$ is the lower incomplete gamma function, $\gamma(a, x) = \int_0^x t^{a-1}e^{-t}dt$.

We calculate $M_{\mathrm{DM}}(r_i)$ of each radial bin through a Monte Carlo (MC) analysis in order to propagate uncertainties accurately. In detail, the prescription for each MC realization is as follows: In each bin i the best estimates of T_i and $n_{e,i}$ are added to random numbers drawn from Gaussian distributions representative of the uncertainties δT_i and $\delta n_{e,i}$. In order to apply eq. (C.3), we estimate the logarithmic derivative of, e.g., T at the bin-radius r_i by the slope of the unique parabola that passes through $(\ln r_{i-1}, \ln T_{i-1})$, $(\ln r_i, \ln T_i)$, and $(\ln r_{i+1}, \ln T_{i+1})$. In this way we can calculate the total mass interior to r_i for that data realization. We subtract the gas mass, estimated through a five-point Newton-Cotes integration formula applied to the same realization of the density data, and we arrive at the dark matter mass $M_{\mathrm{DM},i}$. We impose a number of checks to determine if the derived data realization is physically sensible: the ICM temperature and density must be greater than zero in all bins, the total mass profile must be increasing with radius, and the dark matter mass profile and derived density profile must also be everywhere positive. If these conditions are not met the entire realization is discarded. This process is repeated until $N = 5000$ realizations have been accepted. From these the sample mean of $\ln M_i$ in each bin is determined, as well as the sample covariance matrix with elements

$$C_{ij} = \frac{1}{1-N}\sum_k^N (\ln M_{ik} - \langle \ln M_i \rangle)(\ln M_{jk} - \langle \ln M_j \rangle),$$

(C.4)

where N is the number of Monte Carlo realizations. Even though we sample the ICM temperature and density in each bin independently, the covariance matrix is not diagonal since the derivatives and physical consistency checks induce bin-to-bin correlations in the ac-

cepted sample. We use the mean and covariance of $\ln M$ rather than M since, by inspection, the former is closer to being Gaussian distributed.

C.4 Statistical analysis

We take a Bayesian approach to the statistical analysis and the usual starting point is the likelihood function, which we calculate in the following manner.

It requires less manipulation of the data to calculate the mass profile from the observations than to calculate the density profile. Therefore we integrate the density profile analytically or numerically for each model to obtain the mass distribution and compare with the data in mass space, not density space. Further, as mentioned above, we have found in the MC analysis that the mass samplings in each bin are close to being log-normally distributed. Therefore we construct the likelihood $\mathcal{L}(M_i) = \exp(-\chi^2/2)$ from the χ^2 function,

$$\chi^2 = \sum_{i,j}(\ln M_i - \ln M(r_i))C_{ij}^{-1}(\ln M_j - \ln M(r_j)),$$

(C.5)

where $M(r_i)$ is the model mass profile at the radial centre r_i of bin i, and $\ln M_i$ and C_{ij} are determined by the MC analysis.

The main goal is to decide which model is the better representation of the data. We do this by calculating the Bayesian evidence of each model, which is a quantitative measure of the agreement between model and data (Trotta, 2008). First we calculate the likelihoods of each model on a grid in the parameter space $\theta = (\log r_{-2}, \log \rho_{-2})$. Next, we construct the posterior probability distribution by combining the likelihood function with a prior probability distribution $\pi(\theta)$ resembling our knowledge of $\log r_{-2}$ and $\log \rho_{-2}$ before

taking the data into account. We discuss the choice of prior below. We then integrate the posterior to obtain the Bayesian evidence,

$$E = \int_{\text{all}} d\theta \pi(\theta) \mathcal{L}(\theta, \ln M_i), \qquad (C.6)$$

which is essentially the weighted average of the likelihood over the prior volume. The evidence of a model, given the data and a prior, quantifies how well that model explains the data. It is important to stress that the comparison is made over all of the prior volume, not just at the best fitting set of parameters. When comparing models the Bayes factor $B_{12} = E_1/E_2$ shows how much more (or less) probable model 1 is than model 2, in light of the data. Traditionally, this is gauged on Jeffrey's scale where a Bayes factor of $\ln B_{12} < 1$ is labeled 'inconclusive' evidence for model 1 over model 2 while 'weak', 'moderate', and 'strong' evidence corresponds to $\ln B_{12}$ values < 2.5, < 5, and > 5, respectively.

We choose priors which are constant in the logarithms of r_{-2} and ρ_{-2}. The flat logarithmic prior is the uninformative prior for scaling parameters (Trotta, 2008) since it reflects ignorance about the magnitude of the parameter. However we restrict the range of the priors, so that we end up with top-hat priors in $\log r_{-2}$ and $\log \rho_{-2}$. As a reference point we first assume a top-hat prior relative to the best estimate of r_{2500} as determined in the MC analysis. (The scale radius r_{2500} is defined as the radius within which the mean density is 2500 times the critical density of the universe.) The top-hat prior in $\log r_{-2}$ ranges from 1.5 magnitudes below r_{2500} to 0.5 above. The basic idea behind this prior is that the transition or 'roll' of a model should occur close to r_{2500}, as it does in haloes in numerical simulations, and also to prevent the model from behaving as a simple power-law by pushing the transition from the inner to the outer power law far away from the range of the data. We emphasize that this is still a conservative prior, as current simulations typically resolve 2–3 radial magnitudes with r_{-2} located about one order of magnitude below the virial radius (Bullock et al., 2001b). The prior in ρ_{-2} is also a top-hat in the logarithm and a range of 10^{-26}–10^{-21} kg m^{-3}, which in practice means that the likelihood is vanishingly small at the boundaries of the prior.

Two-parameter model results

The result of the model comparison is summarized in table C.2, where the NFW model is compared against each of the other two-parameter models. A positive Bayes factor indicates that the NFW model is preferred. This does not imply any bias on the NFW since any two

Tab. C.2: Bayes Factor $\ln B$ for the two-parameter models, relative to the NFW profile

Cluster	z	D&M	Hernq.	Moore
A262	0.015	-2.0	0.9	-3.0
NGC533	0.018	-1.7	1.2	-3.0
A496	0.032	-1.4	0.6	-1.2
2A0335+096	0.034	0.5	-0.1	13.2
A2052	0.036	1.9	-0.3	5.8
MKW9	0.040	0.5	-0.1	1.4
MKW3s	0.046	1.8	-0.3	6.2
A4059	0.047	1.5	-0.4	9.5
Sérsic 159–3	0.057	-0.5	1.6	2.7
A1795	0.064	2.5	-0.5	17.9
A1837	0.071	0.5	-0.2	1.2
Total	-	3.6	2.4	51

NOTE. — A positive value of $\ln B$ indicates that the NFW profile is preferred over the considered model. Note that this does not imply any bias towards the NFW as the Bayes factor of any two other models is just the difference between the respective Bayes factors given here.

models can be compared by subtracting the Bayes factors we give for them from one another. We find that, individually, the clusters yield strong constraints only against the Moore model, while the evidences for or against the D&M and Hernquist models are either weak or inconclusive on Jeffrey's scale. If instead we consider the cumulative Bayes factor summed over the full sample, the NFW is found to be the preferred model overall, i.e., as a universal two-parameter profile our sample favors the NFW model. The Hernquist profile and the D&M profile are weakly and moderately disfavored, respectively, with cumulative Bayes factors of 2.4 and 3.6 while the Moore profile is convincingly ruled out with a factor of 51. The weak constraint on the Hernquist profile is not surprising as data extending out to the virial radius would likely be needed to properly distinguish this model from the NFW.

In table C.3 we present the effects of varying the priors. The evidence against the D&M profile increases to the level of strong when we limit the range of the prior in $\log r_{-2}$ to the smaller interval $(-0.75, 0.25)$, while the Bayes factor is reduced slightly on the larger range $(-3, 3)$. The evidence also becomes strong if we choose top-hat priors in (r_{-2}, ρ_{-2}) instead of the logarithmic priors. Finally, the D&M model is disfavored slightly more if we apply a 'soft' Gaussian prior in $\log r_{-2}$. The Bayes factor for the Hernquist model is robust under the same variations, while the Moore
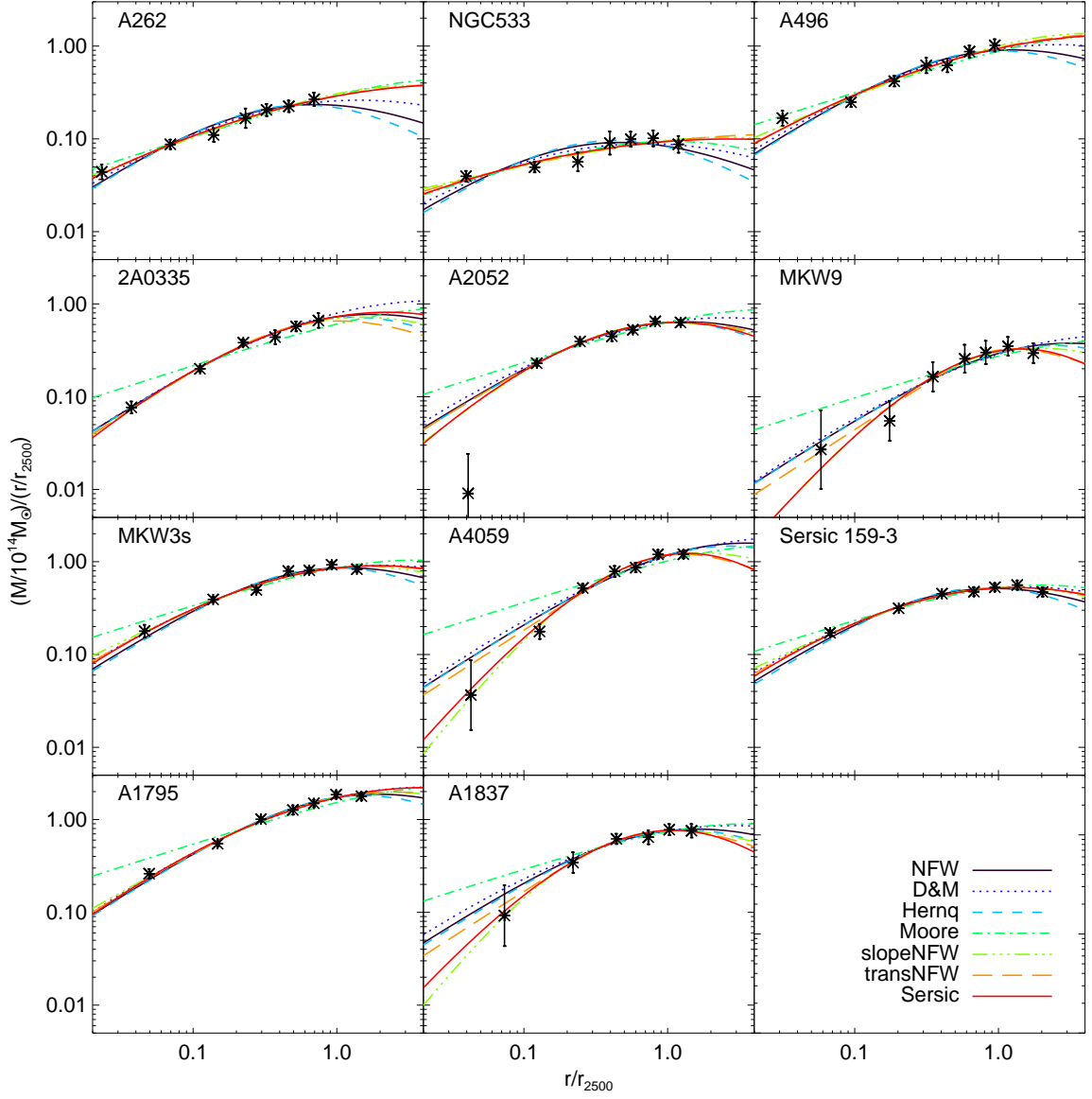
Fig. C.1: Mass profile of each cluster with 68% uncertainties and best-fit models. The radial axis has been scaled to the best estimate of r_{2500} from the MC analysis, and the mass axis has been scaled by r^{-1} so that the fitted models are approximately horizontal at r_{-2}.

profile is very strongly ruled out in all cases. We conclude that our two-parameter model selection results are stable against variation amongst reasonable choices of priors, which means that the data are of sufficient quality to make robust conclusions.

A more interesting issue to consider than the priors is that the preference for the NFW profile over the Hernquist and D&M profiles is somewhat susceptible to 'jackknife' resampling: if we recompute the cumulative Bayes factor eleven times systematically leaving a single cluster out each time, there are a few cases where the strength of the evidence is reduced to inconclusive but also cases where it is increased to strong (against the D&M). This is largely due to the fact that our data sample is somewhat inhomogeneous in terms of the relative statistical uncertainty on the mass profile. For example, a comparison of the error bars of MKW9 with those of A1795 or Sérsic 159-3 (see figure C.1) immediately shows that the former is much less constraining than the latter two. This means that our sample is a mixture of strongly and weakly constraining clusters and this is reflected in figure C.2 where the contributions from individual clusters clearly varies. There appears to be a trend that the clusters A262, NGC533, and A496, which are the lowest redshift and some of the least massive in our sample, stand out by preferring the D&M and the Moore profile. However, such trends are just as likely spurious selection effects caused by the relatively small sample but could be investigated with a larger sample. The D&M profile can easily be preferred by clusters that also prefer the Moore profile since, by extending the transition region, the D&M profile can push the inner asymptotic power law well inside the radial range of the data.

Finally we compare with a standard goodness–of–fit test: the minimum χ^2 values for the models support our more detailed analysis: for a total of 53 degrees of freedom we get minimum χ^2's of 81 for the NFW, 93 for the D&M, 82 for the Hernquist, and 190 for the Moore profile. Major contributions to these χ^2 values come from the two clusters MKW3s with $\chi^2 = 14.2$ and A4059 with $\chi^2 = 13.2$ for the NFW model and similar or larger values for the other models. The corresponding p-values imply that the D&M χ^2 is about 20 times less likely to have occurred by chance (if the D&M model is correct) than the NFW model is (if the NFW model is correct). Compare this with the Bayesian odds that the NFW is ~ 40 times more probable than the D&M. Note that the actual best-fits are slightly smaller since we evaluate the χ^2 on a grid instead of minimizing it with a dedicated search. The χ^2 values show that, also in terms of goodness–o-f-fit, our sample is rather inhomogeneous. The rather poor total fit should not be judged too harshly since the halos in numerical sim-

ulations also show halo–to–halo scatter, which is not accounted for by the fitting profiles.

Three-parameter model results

For the three-parameter models we again want to test whether the models represent the data better than the NFW. In this case the comparison is slightly more involved since there is the freedom of an additional parameter to take into account. This naturally yields a lower value of the evidence if the extra parameter does not provide a better description of the data, or, more specifically, the third parameter must improve the fit over a significant volume of parameter space in order to be preferred over the NFW. It is important to stress that there is no assumption about the third parameter being universal. On the contrary, we ask whether the data require the additional freedom of an extra parameter which is determined individually for each cluster.

The model comparison proceeds as before: we calculate the evidence for each of the three-parameter models with the same priors in $\log r_{-2}$ and $\log \rho_{-2}$ as in the fiducial two-parameter analysis for all models. For the slopeNFW we choose a top-hat prior for α which ranges from 0 to 1.75, i.e. from a cored profile to a profile slightly steeper than the Moore profile. We do not want to go all the way to -2 since r_{-2} tends to zero and eventually becomes undefined as α approaches -2. For the transNFW, we choose a logarithmic prior with γ in the range $(0.1, 4)$ which allows this profile to mimic a steeper inner profile by pushing the asymptotic inner power law inside the radial range of the data. Finally, we take a logarithmic prior for n in the range $(2,15)$ for the Sérsic model, motivated by numerical simulations which have best fits Sérsic profiles with n=5–9. The logarithmic prior has the advantage that it is invariant whether one prefers n or $\alpha_s = 1/n$ as the parameterization.

The resulting Bayes factors relative to the NFW are given in table C.4 and summarized in the chart in figure C.2. The individual clusters provide only weak evidence for or against any of the models. Based on the whole sample, the model selection is inconclusive for the transNFW and Sérsic models but there is 'moderate' evidence for the slopeNFW model over the NFW with a Bayes factor of -2.6. This corresponds to odds of 13 to 1 in favor of the slopeNFW model and shows that, overall, the slopeNFW has the highest evidence E of all models considered. Hence the data show a moderate need for a free inner slope despite the penalty against the extra freedom built into the Bayesian analysis. It must be mentioned that most of the discriminatory power is carried by a few clusters such as NGC533, A4059, and A1795 and removal of any of these clusters

Tab. C.3: Total Bayes factor $\ln B$ for the two-parameter models assuming various priors, relative to the NFW profile

Prior	Range $\log \rho_{-2}$	D&M	Hernq.	Moore
Top-hat in $\log r_{-2}$	(-1.5,0.5)	3.6	2.4	51
Top-hat in $\log r_{-2}$	(-3,3)	2.8	2.5	36
Top-hat in $\log r_{-2}$	(-0.75,0.25)	6.8	2.3	63
Top-hat in (r_{-2}, ρ_{-2})	(-1.5,0.5)	8.8	1.3	60
Gaussian in $\log r_{-2}$	-	4.8	2.3	50

NOTE. — The top line is the fiducial prior used in table C.2. In the next two cases the range of the prior in $\log r_{-2}$ (in units of r_{2500}, see text) is varied, and in the following two cases a top-hat prior in r_{-2} and both r_{-2} and ρ_{-2} is applied. The final case assumes a Gaussian prior in $\log r_{-2}$ with mean -0.25 and width 0.5.
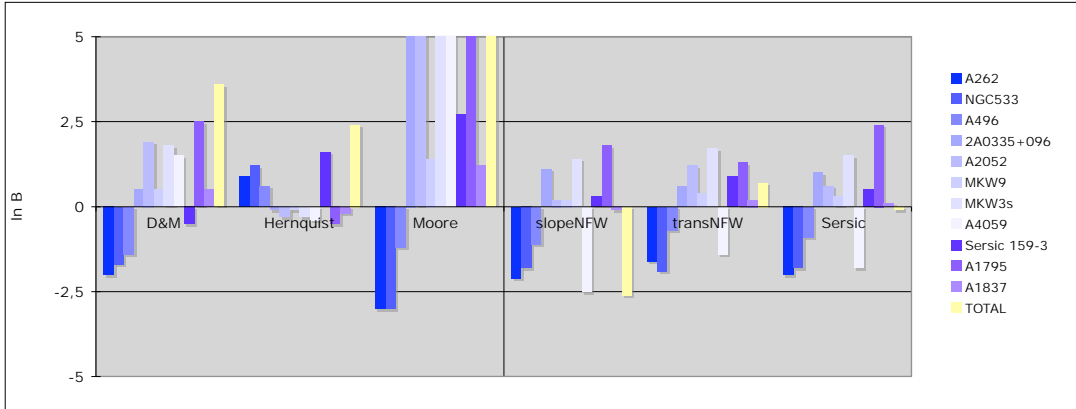

Fig. C.2: Bar chart of the Bayes factors $\ln B$ for the various models considered, relative to the NFW, as given in table C.2 and C.4. The Bayes factors are additive so the contribution of individual clusters to the total Bayes factor is easily assessed. The values shown are based on the fiducial priors discussed in the text.

from the sample would change the Bayes factor significantly. Therefore we caution that the moderate preference for the slopeNFW model is somewhat susceptible to selection effects since, as noted above, the constraints from individual clusters vary in quality. We also find some sensitivity to the choice of prior: if the upper bound of α is extended from 1.75 up to 1.9, the Bayes factor for the slopeNFW model changes to -1.9, while if it is set to the Moore profile at 1.5 the Bayes factor becomes -3.1. If the lower bound of α is increased to 0.5, the Bayes factor remains relatively unchanged at -2.9. While we believe that the fiducial priors used above are reasonable descriptions of the 'state of knowledge' based on numerical simulations, the sensitivity to the choice of prior indicates that the data do not necessarily confine the posterior to a sufficiently small region of

the prior volume to provide unambiguous conclusions.

Constraints on the third parameters

Finally, for the three-parameter models we also want to constrain the preferred value of the third parameter. Unlike above, this analysis assumes that there is a universal value for the third parameter and attempts to identify that value. We use the same priors as in the previous analysis for each model, but now we marginalize over the nuisance parameters $(\log r_{-2}, \log \rho_{-2})$ to find the one-dimensional posterior probability distribution for the third parameter for each cluster. Then we combine the results from the individual clusters into a joint posterior which is simply the product of the the individual ones. We calculate 95% credible intervals for
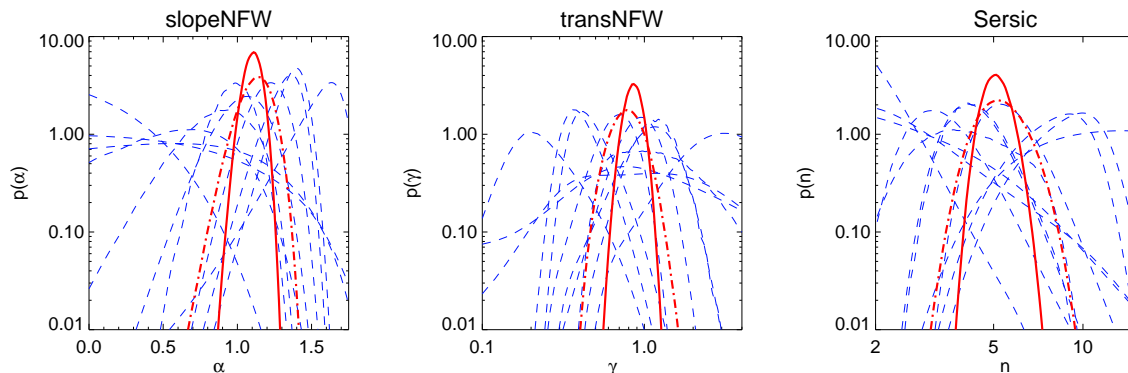
Fig. C.3: Probability distributions for the third parameter in each of the three-parameter models: slopeNFW α (left), transNFW γ (middle), and Sérsic n (right). In each panel, the full line shows the joint posterior for all clusters combined while the dot–dashed line shows the joint posterior obtained using the method of hyper-parameters (see text). The dashed lines are the pdf's of individual clusters. Note that each posterior is normalized to unity so it is not possible to draw conclusions about the quality of fit of the individual clusters from this plot. The standard 95% credible intervals are $(1.00, 1.21)$ for α, $(0.68, 1.06)$ for γ, and $(4.3, 6.2)$ for n. With the hyper-parameters, the intervals are instead $(0.85, 1.31)$ for α, $(0.50, 1.28)$ for γ, and $(3.5, 7.4)$ for n. We assume top-hat priors in α, $\ln\gamma$, and $\ln n$.

Tab. C.4: Bayes Factor $\ln B$ for the three-parameter models, relative to the NFW profile.

Cluster	slopeNFW	transNFW	Sérsic
A262	-2.1	-1.6	-2.0
NGC533	-1.8	-1.9	-1.8
A496	-1.1	-0.7	-0.9
2A0335+096	1.1	0.6	1.0
A2052	0.2	1.2	0.6
MKW9	0.2	0.4	0.3
MKW3s	1.4	1.7	1.5
A4059	-2.5	-1.4	-1.8
Sérsic 159–3	0.3	0.9	0.5
A1795	1.8	1.3	2.4
A1837	-0.1	0.2	0.1
Total	-2.6	0.7	-0.1

NOTE. — A positive value of $\ln B$ indicates that the NFW profile is preferred over the considered model. A top-hat prior in $\log r_{-2}$ of $(-1.5, 0.5)$ around the best estimate of r_{2500} for each cluster is assumed.

both the individual and the joint posterior. However, we know from the previous analysis that each three-parameter model is preferred by some clusters but not by others. Therefore we also use the method of hyper-parameters (Lahav et al., 2000) which allows the contribution from individual data-sets to the joint posterior to be weighted. These weights are marginalized over assuming logarithmic priors with the result that in the joint likelihood one replaces

$$\sum_i \chi_i^2 \to \sum_i N_i \ln \chi_i^2, \qquad (C.7)$$

where N_i is the number of data points in data-set i. The upshot of all this is that clusters that are not described well by the model do not constrain the parameters as strongly as clusters that are well described. The price to pay is that the effective sample size is reduced which, all other things being equal, will lead to wider and more conservative credible intervals.

The results are shown in figure C.3, where in each panel the fully drawn line is the joint posterior, the dotted line is the hyper-parameters posterior, and the dashed lines are the posteriors of the individual clusters. The generalized NFW models are drawn slightly away from, but not in disagreement with, the NFW with 95% credible intervals of $(1.00, 1.21)$ for α and $(0.68, 1.06)$ for γ. The interval for the Sérsic n parameter is $(4.3, 6.2)$,

in good agreement with the values reported by the Aquarius numerical simulations for Milky Way-sized halos (Navarro et al., 2008). The intervals derived using the method of hyper-parameters are wider as expected: $(0.85, 1.31)$ for α, $(0.50, 1.28)$ for γ, and $(3.5, 7.4)$ for n. The difference between the hyper-parameters method and the conventional calculation illustrates the need for a cautious approach to in-homogeneous data-sets. We believe the hyper-parameters yields the more trustworthy results in the case at hand, while on the other hand we acknowledge that they are not very constraining.

An inspection of the contribution from individual clusters reveals some issues: It is clear that for each model a number of clusters provide very little information about the third parameter, i.e. the model describes the mass profile almost equally well regardless of the third parameter value. This is actually expected, given the varying size of the Bayes factors in table C.4. There are also a few cases, particularly for the transNFW model, where the posterior peaks very close to or on the bounds of the prior. In such cases the results, e.g. the individual credible intervals, are of course very prior-dependent which again indicates that the data are not very discriminatory with respect to the prior. On the other hand, rather drastic priors or small sub-samples must be used in order to significantly affect the credible intervals of the joint posterior, especially for the hyper-parameters method.

Figure C.4 shows the individual clusters' constraints on α, γ, and n. As could be expected given the varying nature of our results, there is perhaps the slightest of hints of a redshift–dependence in the constraints but our sample size does not allow us to probe such an issue in detail. It should again be noted that any hint of a redshift–dependence could actually be caused by a mass–dependence instead, since the two lowest redshift clusters in our sample are also the least massive.

A different picture emerges when we consider the overlap of the individual clusters' credible intervals for the slopeNFW model. For example, no value of α is contained in all 11 95% credible intervals, and only the very short range $(1.08, 1.10)$ is contained in all but two intervals. Likewise the NFW $\alpha = 1$ case is excluded from four of the eleven intervals. These results, as well as a visual inspection of figure C.3, puts strong doubts about the concept of a universal shape parameter. The situation is not quite as compelling for the transNFW and Sérsic models which is likely the reason that they do not stand out from the NFW in the model selection. In fact, we believe it is a reasonable statement that the success of the slopeNFW model is precisely due to the very different preferred values of α from cluster to cluster. This puts a strong question mark against the idea of universal third parameter.
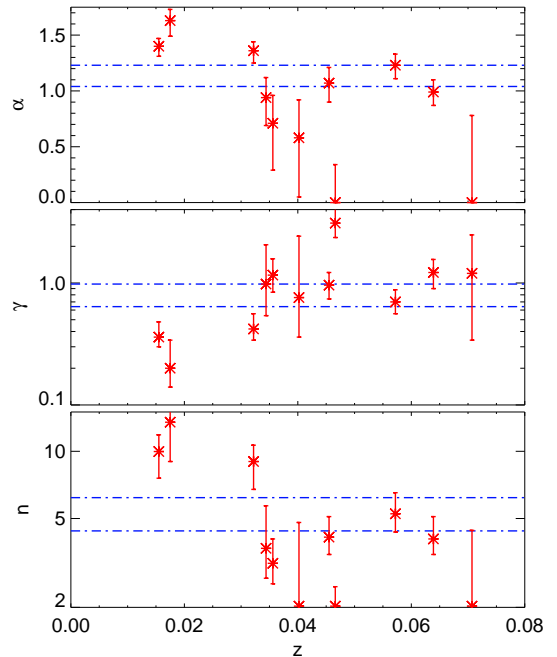

Fig. C.4: The individual clusters' constraints on the third parameter in each of the three-parameter models. In this case we show the 68% credible intervals, and the horizontal lines indicate the 68% range of the joint posterior calculated using the method of hyper-parameters. Refer to table C.2 for the redshifts of each cluster.

We conclude that there is moderate evidence for the slopeNFW model to be preferred over the simple NFW, while the transNFW and Sérsic models do not stand out against the two-parameter NFW profile. If the inner slope of the slopeNFW model is universal, we constrain it to be close to -1 but preferably slightly steeper. However, the spread of the individual clusters' preferred ranges suggests that the inner slope is not universal.

We also comment that the method of hyper-parameters method could in principle be extended to the model selection analysis. As a matter of fact, since the slopeNFW 'contains' both the NFW and the Moore models as subsets, we can derive the corresponding Bayes factor for the Moore profile which is only 10. This is of course a drastic reduction numerically but it does not alter the conclusion and anyway corresponds to rather convincing odds of about $20\,000 : 1$.

C.5 Biases

So far we have discussed the interpretation of our results with respect to the statistical evidence. However, a number of biases, or systematic uncertainties, can be thought of that may affect our results. Loosely, these can be grouped into biases that affect both the individual cluster mass modeling and the combined analysis, and selection effects that only influence the latter.

The analysis rests on the ability to produce deprojected temperature and density profiles with uncertainties that correctly mirror the uncertainties in the spectral analysis of the x-ray data. This has been discussed extensively in Kaastra et al. (2004). The basic assumption in determining the mass distribution of a galaxy cluster is that the cluster is relaxed, and obeys the equation of hydrostatic equilibrium. Numerical simulations indicate that the additional pressure associated with turbulence and bulk motion in the ICM yields an underestimate of the mass in the region of $5 - 20\%$ with the larger values corresponding to large radii, r_{500} and greater (Nagai et al., 2007; Piffaretti & Valdarnini, 2008; Lau et al., 2009). We do not expect this bias to exceed 10% in the present case since we do not model further out than to $\sim r_{2500}$. On the other hand, the same numerical simulations indicate that if the turbulent pressure is accounted for, an accurate mass reconstruction is possible. This point demonstrates that deviations from spherical symmetry are not a major concern in the error budget.

A related question is whether the parameterized profiles should be tested against the total mass distribution or the dark matter mass profile only. While the predictions of numerical simulations are founded in dark matter-only simulations, it is not clear how much a simulated dark matter-only mass profile is modified by the presence of baryons. Observationally, the ICM contributes about $5 - 15\%$ of the total density in a cluster, again increasing with radius in the range of interest here, so formally there is a difference between the total and the dark matter profile's radial dependence. To test the impact of this, we have rerun the statistical analyses described above without subtracting the ICM mass from the mass estimate of eq. (C.3). We find only minor differences: For the two-parameter models, the total Bayes factors relative to the NFW profile, assuming the fiducial prior as in table C.2, are 2.8 (D&M), 2.7 (Hernquist), and 54 (Moore), i.e. there is no significant change in the interpretation of the results. For the three-parameter models, the total Bayes factors become -3.1 (slopeNFW), 0.6 (transNFW), and -0.2 (Sérsic), which are in good agreement with the results in table C.4. Finally, the constraints on the third parameters for the three-parameter models are unchanged.

The fact that our results are stable whether we test the mass models against the total or dark matter-only mass profiles allows us to gauge how important the mass bias caused by turbulent pressure is. The point is that the turbulent pressure is expected to contribute the same amount (or less) to the total mass estimate as the ICM mass: both contributions are at the $5 - 15\%$ level and radially increasing, and at the maximum radius we consider $\sim r_{2500}$ the gas fraction ($\sim 10\%$) is likely larger than the pressure bias. Since our results are the same whether we account for the ICM mass or not, we conclude that the systematic uncertainty is likely much smaller than the statistical uncertainty.

C.6 Mass–concentration relation

An important consequence of the 'bottom-up' scenario of structure formation is that smaller halos are denser in the center, since they formed earlier when the density of the Universe was higher. This effect is seen in numerical simulations and it can be expressed as a relation between the halo mass and the concentration parameter. The concentration parameter is defined for a given overdensity as $c_\Delta = r_\Delta/r_{-2}$ (often r_s is used instead of r_{-2} but for the NFW this is unimportant). Simulations usually consider the mass–concentration relation at the virial radius r_{200}, but we can only reach that radius by model-dependent extrapolation. Therefore, in figure C.5, we show the mass–concentration relation of our sample calculated within the NFW model at both r_{2500} and extrapolated to r_{200}. We suggest that authors provide relations at both of these Δ's as they complement each other in physical significance and observational accessibility.

As can be seen in figure C.5, our sample is not ideally suited to derive a relation from given that six sample members cluster at almost identical values of M_Δ. Instead we compare with the mass–concentration relation of the simulations presented in Macciò et al. (2008), which are in reasonable agreement with our sample except for the low mass NGC533. We emphasize that the orientation of the uncertainty ellipses is related only to the parameter degeneracies present in the combination of model and mass profile data and has nothing to do with the slope of the mass–concentration relation. The agreement between our observed mass–concentration relation and the predictions of numerical simulations resembles the recent x-ray analysis of Buote et al. (2007), but stands out from the significant discrepancy of the lensing study in Broadhurst et al. (2008).
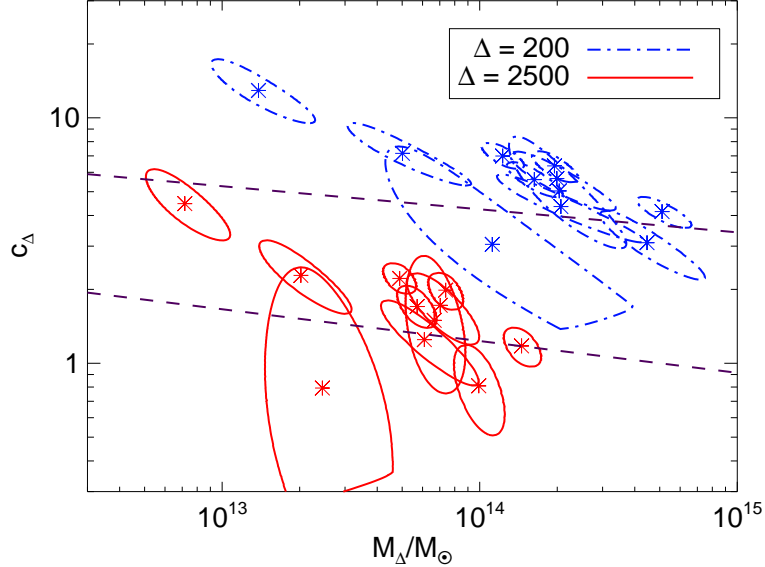
Fig. C.5: The mass–concentration relation of our sample, calculated within the NFW model. The contours contain 95% of the posterior PDF and are based on the fiducial prior. We show two contours for each cluster: (M_{2500}, c_{2500}) (red, full lines) which are derived within the radial range of the data, and (M_{200}, c_{200}) (blue, dot-dashed) which is based on an NFW model-dependent extrapolation to r_{200}. The dashed lines show the mean relations for the two values of Δ from the N-body simulations of Macciò et al. (2008), based on the WMAP5 cosmology. The relations are $\log c_{200} = 0.83 - 0.094 \log(M_{200}/10^{12} M_\odot)$ and $\log c_{2500} = 0.35 - 0.130 \log(M_{2500}/10^{12} M_\odot)$. Given the low redshift of our sample, we have not made any correction for a redshift evolution of c_Δ.

C.7   Summary & discussion

We have conducted a careful statistical analysis of the constraints on mass distribution models of galaxy clusters which can be derived from x-ray observations. We find that the NFW model is the preferred two-parameter model and that the Moore model is decisively ruled out. There is moderate evidence that the data require an additional free parameter that alters the shape of the mass profile, and the best choice is a model similar to the NFW but with a freely varying inner slope. If we assume this slope to be universal, we can constrain it to be close to or slightly steeper than the NFW, but our data suggest that the shape parameter must be determined individually.

Significantly, the clusters in our sample prefer very different values for the inner slope, some prefer flat cores while others prefer steep cusps. The shape-parameters of the other two three-parameter models

we consider, the Sérsic and transNFW, also show considerable scatter across our sample. We conclude that there is a strong indication in our data that the mass profile is not universal but suffers considerable halo-to-halo scatter. The limited size of our sample means that we cannot assess whether this is in disagreement with the results of numerical simulations. Of course, we can force universality of the inner slope, in which case we find that it is preferred to be slightly steeper than the NFW value of -1. However, when the goodness–of–fit of each cluster is taken into account using the method of Bayesian hyper-parameters, the credible interval becomes significantly larger, partly because of the smaller effective sample size, but also because of the lack of universality.

This analysis stands out from the numerous observational results that claim significant discrepancies from simulations based on only one or a few observed clusters. We acknowledge that our sample size is still lim-

ited, but it allows us to discuss the issue of universality. Given that halos in numerical simulations which include baryons are still not readily mass produced with sufficient resolution, which makes the question of halo to halo scatter difficult to assess, it is not possible to decide if the strong indication of a non-universal model that we see is at odds with the numerical predictions.

Our results are largely insensitive to whether we compare the models with the dark matter mass profile or the total mass profile, and so we cannot judge whether one type of model is more appropriate for the dark matter halo or the total gravitational potential of a halo. There are two reasons for this: firstly, the uncertainties of primarily the ICM temperature profiles are too large, and secondly, the angular resolution in the center is not good enough. Of course the ICM is rather smoothly distributed and very good statistics would be needed for a model to fit either the total or dark matter distribution significantly better. For nine of the 11 clusters of our sample we readily found 2MASS (Skrutskie et al., 2006) cD or BCG galaxies very close to the x-ray center but including these in the mass budget does not make a difference, unless we assumed extreme mass-to-light ratios. This is again due to the limited angular resolution of the observations which implies that a large amount of dark matter is contained even within the radial center of the innermost bin.

The robustness of our results whether we use the dark matter or total mass profile gives us reasonable confidence that deviations from hydrostatic equilibrium in the ICM are not a major problem. Such a systematic uncertainty would yield a bias of at most 10–15% according to numerical simulations, which is similar to the difference between the total and dark matter mass profiles.

Declaration of co-authorship

Name: Ole Høst	
Civ. Reg. No. (CPR. No.): 080980-****	E-mail: olehost@dark-cosmology.dk
Department: Dark Cosmology Centre, Niels Bohr Institute	
Principal supervisor: Steen H. Hansen	E-mail: hansen@dark-cosmology.dk
Title of PhD thesis: Observational probes of dark matter halos	

This co-authorship declaration applies to the following paper:

Host & Hansen (2007): What it takes to measure a fundamental difference between dark matter and baryons: the halo velocity anisotropy
(Paper I)

The student's contribution to the paper

Development of the method used and the numerical implementation, analysis and characterization of results, writing the paper.

Signatures of co-authors

Date (dd/mm/yy)	Name	Signature
25.08.2009	**Steen H. Hansen**	

PhD student: _____ **Date:_____**
                  Signature   (dd/mm/yy)

A copy must be sent to the department.

When completed, the form with signatures must be forwarded by e-mail, preferably in PDF format, to:

E-mail: PhD@science.ku.dk

Graduate School at the Faculty of Science, University of Copenhagen, Tagensvej 16, DK-2200 Copenhagen N.

Declaration of co-authorship   1/1   Revised 26th of May 2009

Declaration of co-authorship

Name: Ole Høst	
Civ. Reg. No. (CPR. No.): 080980-****	E-mail: olehost@dark-cosmology.dk
Department: Dark Cosmology Centre, Niels Bohr Institute	
Principal supervisor: Steen H. Hansen	E-mail: hansen@dark-cosmology.dk
Title of PhD thesis: Observational probes of dark matter halos	

This co-authorship declaration applies to the following paper:

Host et al., (2009): Measurement of the dark matter velocity anisotropy in galaxy clusters (Paper II)

The student's contribution to the paper

Development of the method used and the numerical implementation, analysis of deprojected observational data, characterization of the simulation data, writing the paper.

Signatures of co-authors

Date (dd/mm/yy)	Name	Signature
25.08.2009	**Steen H. Hansen**	*Steen Hansen*

PhD student: _____ **Date:**_____
            Signature   (dd/mm/yy)

A copy must be sent to the department.

When completed, the form with signatures must be forwarded by e-mail, preferably in PDF format, to:

E-mail: PhD@science.ku.dk

Graduate School at the Faculty of Science, University of Copenhagen, Tagensvej 16, DK-2200 Copenhagen N.

Declaration of co-authorship

Name: Ole Høst	
Civ. Reg. No. (CPR. No.): 080980-****	E-mail: olehost@dark-cosmology.dk
Department: Dark Cosmology Centre, Niels Bohr Institute	
Principal supervisor: Steen H. Hansen	E-mail: hansen@dark-cosmology.dk
Title of PhD thesis: Observational probes of dark matter halos	

This co-authorship declaration applies to the following paper:

Host & Hansen (2009): A detailed statistical analysis of the dark matter mass profiles of galaxy clusters (Paper III)

The student's contribution to the paper

Development of the method used and the numerical implementation, analysis of deprojected observational data, writing the paper.

Signatures of co-authors

Date (dd/mm/yy)	Name	Signature
25.08.2009	**Steen H. Hansen**	

PhD student: _____ **Date:**_____
       Signature   (dd/mm/yy)

A copy must be sent to the department.

When completed, the form with signatures must be forwarded by e-mail, preferably in PDF format, to:

E-mail: PhD@science.ku.dk

Graduate School at the Faculty of Science, University of Copenhagen, Tagensvej 16, DK-2200 Copenhagen N.

BIBLIOGRAPHY

Abdo, A. A. et al. 2009, Phys. Rev. Lett., 102, 181101, arXiv:0905.0025

Adelman-McCarthy, J. K. et al. 2008, Astrophys. J. S., 175, 297, arXiv:0707.3413

Adriani, O. et al. 2009a, Nature, 458, 607, arXiv:0810.4995

——. 2009b, Phys. Rev. Lett., 102, 051101, arXiv:0810.4994

Aharonian, F. et al. 2008, Phys. Rev. D, 78, 072008, arXiv:0806.2981

——. 2009a, Astrophys. J., 691, 175, arXiv:0809.3894

Aharonian, F., et al. 2009b, arXiv:0905.0105

Ahmed, Z. et al. 2009, Phys. Rev. Lett., 102, 011301, arXiv:0802.3530

Ahmed, Z., et al. 2009, arXiv:0902.4693

Akerib, D. S. et al. 2006, Phys. Rev. D, 73, 011102, arXiv:astro-ph/0509269

Akerib, D. S., et al. 2006, Phys. Rev. Lett., 96, 011302, arXiv:astro-ph/0509259

Allen, S. W., Rapetti, D. A., Schmidt, R. W., Ebeling, H., Morris, R. G., & Fabian, A. C. 2008, Mon. Not. Roy. Astron. Soc., 383, 879, arXiv:0706.0033

Alner, G. J. et al. 2007, Astropart. Phys., 28, 287, arXiv:astro-ph/0701858

Alner, G. J., et al. 2005, Nucl. Instrum. Meth., A555, 173

Angle, J. et al. 2008a, Phys. Rev. Lett., 100, 021303, arXiv:0706.0039

——. 2008b, Phys. Rev. Lett., 101, 091301, arXiv:0805.2939

Aprile, E., & Baudis, L. 2009, arXiv:0902.4253

Aprile, E. et al. 2009, Phys. Rev. C, 79, 045807, arXiv:0810.0274

Arkani-Hamed, N., Finkbeiner, D. P., Slatyer, T. R., & Weiner, N. 2009, Phys. Rev. D, 79, 015014, arXiv:0810.0713

Arnaud, M., Pointecouteau, E., & Pratt, G. W. 2005, Astron. & Astrop., 441, 893, arXiv:astro-ph/0502210

Ascasibar, Y. 2003, PhD thesis, Universidad Autonoma de Madrid, arXiv:astro-ph/0305250

Ascasibar, Y., Yepes, G., Gottlöber, S., & Müller, V. 2004, Mon. Not. Roy. Astron. Soc., 352, 1109, arXiv:astro-ph/0312221

Austin, C. G., Williams, L. L. R., Barnes, E. I., Babul, A., & Dalcanton, J. J. 2005, Astrophys. J., 634, 756, arXiv:astro-ph/0506571

Baudis, L. 2007a, arXiv:0711.3788

——. 2007b, Journal of Physics Conference Series, 65, 012015, arXiv:astro-ph/0703183

Behnke, E. et al. 2008, Science, 319, 933, arXiv:0804.2886

Belikov, A. V., & Hooper, D. 2009, Phys. Rev. D, 80, 035007, arXiv:0904.1210

Bergstrom, L. 2009, New Journal of Physics (submitted), arXiv:0903.4849

Bergström, L., Edsjö, J., & Zaharijas, G. 2009, Phys. Rev. Lett., 103, 031103, arXiv:0905.0333

Bernabei, R. et al. 2008, European Physical Journal C, 167, arXiv:0804.2741

Bernabei, R., et al. 1999, Phys. Lett., B450, 448

——. 2000, Phys. Lett., B480, 23

Bertone, G., Hooper, D., & Silk, J. 2005, Physics Reports., 405, 279, arXiv:hep-ph/0404175

Bertschinger, E. 1985, Astrophys. J. S., 58, 39

Biermann, P. L., Becker, J. K., Meli, A., Rhode, W., Seo, E. S., & Stanev, T. 2009, Phys. Rev. Lett., 103, 061101, arXiv:0903.4048

Binney, J. 1980, Mon. Not. Roy. Astron. Soc., 190, 873

Binney, J., & Tremaine, S. 1987, Galactic Dynamics (Princeton, NJ, Princeton University Press, 1987, 747 p.)

——. 2008, Galactic Dynamics: Second Edition (Princeton University Press)

Blumenthal, G. R., Faber, S. M., Flores, R., & Primack, J. R. 1986, Astrophys. J., 301, 27

Bolte, W. J. et al. 2007, Nuclear Instruments and Methods in Physics Research A, 577, 569, arXiv:astro-ph/0503398

Bouwens, R. J., Illingworth, G. D., Franx, M., & Ford, H. 2008, Astrophys. J., 686, 230, arXiv:0803.0548

Bradač, M., Allen, S. W., Treu, T., Ebeling, H., Massey, R., Morris, R. G., von der Linden, A., & Applegate, D. 2008, Astrophys. J., 687, 959, arXiv:0806.2320

Bravin, M., et al. 1999, Astropart. Phys., 12, 107, arxiv:hep-ex/9904005

Broadhurst, T., Takada, M., Umetsu, K., Kong, X., Arimoto, N., Chiba, M., & Futamase, T. 2005, Astrophys. J., 619, L143, arXiv:astro-ph/0412192

Broadhurst, T., Umetsu, K., Medezinski, E., Oguri, M., & Rephaeli, Y. 2008, Astrophys. J. L., 685, L9, arXiv:0805.2617

Bryan, G. L., & Norman, M. L. 1998, Astrophys. J., 495, 80, arXiv:astro-ph/9710107

Bullock, J. S., Dekel, A., Kolatt, T. S., Kravtsov, A. V., Klypin, A. A., Porciani, C., & Primack, J. R. 2001a, Astrophys. J., 555, 240, arXiv:astro-ph/0011001

Bullock, J. S., Kolatt, T. S., Sigad, Y., Somerville, R. S., Kravtsov, A. V., Klypin, A. A., Primack, J. R., & Dekel, A. 2001b, Mon. Not. Roy. Astron. Soc., 321, 559, arXiv:astro-ph/9908159

Buote, D. A., Gastaldello, F., Humphrey, P. J., Zappacosta, L., Bullock, J. S., Brighenti, F., & Mathews, W. G. 2007, Astrophys. J., 664, 123, arXiv:astro-ph/0610135

Buote, D. A., & Lewis, A. D. 2004, Astrophys. J., 604, 116, arXiv:astro-ph/0312109

Burgos, S. et al. 2009, Astropart. Phys., 31, 261, arXiv:0809.1831

Carlberg, R. G. et al. 1997, Astrophys. J., 485, L13+, arXiv:astro-ph/9703107

Cavaliere, A., & Fusco-Femiano, R. 1978, Astron. & Astrop., 70, 677

Chang, J. et al. 2008, Nature, 456, 362

Cheng, H.-C., Feng, J. L., & Matchev, K. T. 2002, Phys. Rev. Lett., 89, 211301, arXiv:hep-ph/0207125

Churazov, E., Sunyaev, R., Sazonov, S., Revnivtsev, M., & Varshalovich, D. 2005, Mon. Not. Roy. Astron. Soc., 357, 1377, arXiv:astro-ph/0411351

Cirelli, M., Iocco, F., & Panci, P. 2009a, arXiv:0907.0719

Cirelli, M., Kadastik, M., Raidal, M., & Strumia, A. 2009b, Nuclear Physics B, 813, 1, arXiv:0809.2409

Cole, S., & Lacey, C. 1996, Mon. Not. Roy. Astron. Soc., 281, 716+, arXiv:astro-ph/9510147

Cole, S. et al. 2005, Mon. Not. Roy. Astron. Soc., 362, 505, arXiv:astro-ph/0501174

Colín, P., Klypin, A. A., & Kravtsov, A. V. 2000, Astrophys. J., 539, 561, arXiv:astro-ph/9907337

Comerford, J. M., Meneghetti, M., Bartelmann, M., & Schirmer, M. 2006, Astrophys. J., 642, 39, arXiv:astro-ph/0511330

Conroy, C., & Wechsler, R. H. 2009, Astrophys. J., 696, 620, arXiv:0805.3346

Copi, C. J., Heo, J., & Krauss, L. M. 1999, Phys. Lett., B461, 43, arxiv:hep-ph/9904499

Copi, C. J., & Krauss, L. M. 2001, Phys. Rev., D63, 043507, arXiv:astro-ph/0009467

Croton, D. J. et al. 2006, Mon. Not. Roy. Astron. Soc., 365, 11, arXiv:astro-ph/0508046

D'Amico, G., Kamionkowski, M., & Sigurdson, K. 2009, arXiv:0907.1912

de Vaucouleurs, G. 1948, Annales d'Astrophysique, 11, 247

Dehnen, W., & Binney, J. 1998, Mon. Not. Roy. Astron. Soc., 298, 387, arXiv:astro-ph/9710077

Dehnen, W., & McLaughlin, D. E. 2005, Mon. Not. Roy. Astron. Soc., 363, 1057, arXiv:astro-ph/0506528

Dehnen, W., McLaughlin, D. E., & Sachania, J. 2006, Mon. Not. Roy. Astron. Soc., 369, 1688, arXiv:astro-ph/0603825

Del Popolo, A. 2009, Astrophys. J., 698, 2093, arXiv:0906.4447

Desai, S. et al. 2004, Phys. Rev. D, 70, 083523, arXiv:hep-ex/0404025

Deyoung, T. 2009, Modern Physics Letters A, 24, 1543, arXiv:0906.4530

Diemand, J., Kuhlen, M., Madau, P., Zemp, M., Moore, B., Potter, D., & Stadel, J. 2008, Nature, 454, 735, arXiv:0805.1244

Diemand, J., & Moore, B. 2009, Advanced Science Letters (to appear), arXiv:0906.4340

Diemand, J., Moore, B., & Stadel, J. 2004, Mon. Not. Roy. Astron. Soc., 353, 624, arXiv:astro-ph/0402267

Dobler, G., & Finkbeiner, D. P. 2008, Astrophys. J., 680, 1222, arXiv:0712.1038

Dodelson, S. 2003, Modern cosmology (Academic Press)

Dodelson, S., & Widrow, L. M. 1994, Phys. Rev. Lett., 72, 17, arXiv:hep-ph/9303287

Drees, M., & Shan, C.-L. 2007, Journal of Cosmology and Astro-Particle Physics, 6, 11, arXiv:astro-ph/0703651

——. 2008, Journal of Cosmology and Astro-Particle Physics, 6, 12, arXiv:0803.4477

Drukier, A. K., Freese, K., & Spergel, D. N. 1986, Phys. Rev. D, 33, 3495

Dubinski, J., & Carlberg, R. G. 1991, Astrophys. J., 378, 496

Dujmic, D. et al. 2008a, Astropart. Phys., 30, 58, arXiv:0804.4827

——. 2008b, Nuclear Instruments and Methods in Physics Research A, 584, 327, arXiv:0708.2370

EDELWEISS Collaboration. 2007, Nuclear Physics B Proceedings Supplements, 173, 99, arXiv:astro-ph/0612207

Einasto, Y. I. 1969, Astrophysics, 5, 67

El-Zant, A., Shlosman, I., & Hoffman, Y. 2001, Astrophys. J., 560, 636, arXiv:astro-ph/0103386

Ettori, S., Fabian, A. C., Allen, S. W., & Johnstone, R. M. 2002, Mon. Not. Roy. Astron. Soc., 331, 635, arXiv:astro-ph/0111586

Evans, N. W., Carollo, C. M., & de Zeeuw, P. T. 2000, Mon. Not. Roy. Astron. Soc., 318, 1131, arXiv:astro-ph/0008156

Evrard, A. E. et al. 2008, Astrophys. J., 672, 122, arXiv:astro-ph/0702241

Fabricant, D., Lecar, M., & Gorenstein, P. 1980, Astrophys. J., 241, 552

Fairbairn, M., & Schwetz, T. 2009, Journal of Cosmology and Astro-Particle Physics, 1, 37, arXiv:0808.0704

Finkbeiner, D. P., & Weiner, N. 2007, Phys. Rev. D, 76, 083519, arXiv:astro-ph/0702587

Fisher, R. 1953, Proceedings of the Royal Society of London. Series A, Mathematical and Physical Sciences, 217, 295

Freedman, W. L. et al. 2001, Astrophys. J., 553, 47, arXiv:astro-ph/0012376

Freese, K., Frieman, J., & Gould, A. 1988, Phys. Rev. D, 37, 3388

Fukushige, T., Kawai, A., & Makino, J. 2004, Astrophys. J., 606, 625, arXiv:astro-ph/0306203

Fukushige, T., & Makino, J. 1997, Astrophys. J., 477, L9, arXiv:astro-ph/9610005

Gaitskell, R. J. 2004, Annual Review of Nuclear and Particle Science, 54, 315

Gao, L., Navarro, J. F., Cole, S., Frenk, C. S., White, S. D. M., Springel, V., Jenkins, A., & Neto, A. F. 2008, Mon. Not. Roy. Astron. Soc., 387, 536, arXiv:0711.0746

Gastaldello, F., Buote, D. A., Humphrey, P. J., Zappacosta, L., Bullock, J. S., Brighenti, F., & Mathews, W. G. 2007, Astrophys. J., 669, 158, arXiv:astro-ph/0610134

Gilmore, G. 2009, Lecture given at the 13th Paris Cosmology Colloquium

Gilmore, G., Wilkinson, M. I., Wyse, R. F. G., Kleyna, J. T., Koch, A., Evans, N. W., & Grebel, E. K. 2007, Astrophys. J., 663, 948, arXiv:astro-ph/0703308

Gnedin, O. Y., Kravtsov, A. V., Klypin, A. A., & Nagai, D. 2004, Astrophys. J., 616, 16, arXiv:astro-ph/0406247

Goerdt, T., Moore, B., Read, J. I., Stadel, J., & Zemp, M. 2006, Mon. Not. Roy. Astron. Soc., 368, 1073, arXiv:astro-ph/0601404

Gonzalez-Garcia, M. C., & Maltoni, M. 2008, Physics Reports., 460, 1, arXiv:0704.1800

Graham, A. W., Merritt, D., Moore, B., Diemand, J., & Terzić, B. 2006, Astronom. J., 132, 2701, arXiv:astro-ph/0608613

Grasso, D. et al. 2009, Astropart. Phys. (accepted), arXiv:0905.0636

Green, A. M. 2002, Phys. Rev., D66, 083003, arXiv:astro-ph/0207366

Green, A. M., & Morgan, B. 2007, Astropart. Phys., 27, 142, arXiv:astro-ph/0609115

Green, A. M., & Morgan, B. 2008, Phys. Rev. D, 77, 027303, arXiv:0711.2234

Gunn, J. E., & Gott, J. R. I. 1972, Astrophys. J., 176, 1

Hannestad, S., Mirizzi, A., Raffelt, G. G., & Wong, Y. Y. Y. 2008, Journal of Cosmology and Astro-Particle Physics, 4, 19, arXiv:0803.1585

Hansen, S. H. 2004, Mon. Not. Roy. Astron. Soc., 352, L41, arXiv:astro-ph/0405371

Hansen, S. H., & Moore, B. 2006, New Astronomy, 11, 333

Hansen, S. H., Moore, B., Zemp, M., & Stadel, J. 2006, Journal of Cosmology and Astro-Particle Physics, 0601, 014, arXiv:astro-ph/0505420

Hansen, S. H., & Piffaretti, R. 2007, Astron. & Astrop., 476, L37, arXiv:0705.4680

Hansen, S. H., & Stadel, J. 2006, Journal of Cosmology and Astro-Particle Physics, 5, 14, arXiv:astro-ph/0510656

Helm, R. H. 1956, Phys. Rev., 104, 1466

Hernquist, L. 1990, Astrophys. J., 356, 359

Hooper, D. 2009, arXiv:0901.4090

Hooper, D., Zaharijas, G., Finkbeiner, D. P., & Dobler, G. 2008, Phys. Rev. D, 77, 043511, arXiv:0709.3114

Host, O., & Hansen, S. H. 2007, Journal of Cosmology and Astro-Particle Physics, 6, 16, arXiv:0704.2909

——. 2009, Astrophys. J. (submitted), arXiv:0907.1097

Host, O., Hansen, S. H., Piffaretti, R., Morandi, A., Ettori, S., Kay, S. T., & Valdarnini, R. 2009, Astrophys. J., 690, 358, arXiv:0808.2049

Hu, W., Fukugita, M., Zaldarriaga, M., & Tegmark, M. 2001, Astrophys. J., 549, 669, arXiv:astro-ph/0006436

Hu, W., Sugiyama, N., & Silk, J. 1997, Nature, 386, 37, arXiv:astro-ph/9504057

Ikebe, Y., Böhringer, H., & Kitayama, T. 2004, Astrophys. J., 611, 175, arXiv:astro-ph/0402634

Iocco, F., Mangano, G., Miele, G., Pisanti, O., & Serpico, P. D. 2009, Physics Reports., 472, 1, arXiv:0809.0631

Jungman, G., Kamionkowski, M., & Griest, K. 1996, Phys. Rept., 267, 195, arxiv:hep-ph/9506380

Kaastra, J. S. et al. 2004, Astron. & Astrop., 413, 415, arXiv:astro-ph/0309763

Kay, S. T., et al. 2007, Mon. Not. Roy. Astron. Soc., 377, 317, arXiv:astro-ph/0611017

Kirillov, A. A., & Turaev, D. 2006, Mon. Not. Roy. Astron. Soc., 371, L31, arXiv:astro-ph/0604496

Kleyna, J. T., Wilkinson, M. I., Gilmore, G., & Evans, N. W. 2003, Astrophys. J. L., 588, L21, arXiv:astro-ph/0304093

Klypin, A., Kravtsov, A. V., Bullock, J. S., & Primack, J. R. 2001, Astrophys. J., 554, 903, arXiv:astro-ph/0006343

Kolb, E. W., & Turner, M. S. 1990, The early universe (Addison-Wesley)

Komatsu, E. et al. 2009, Astrophys. J. S., 180, 330, arXiv:0803.0547

Koposov, S. et al. 2008, Astrophys. J., 686, 279, arXiv:0706.2687

Kravtsov, A. V., Gnedin, O. Y., & Klypin, A. A. 2004, Astrophys. J., 609, 482, arXiv:astro-ph/0401088

Kuhlen, M., Diemand, J., & Madau, P. 2008, Astrophys. J., 686, 262, arXiv:0805.4416

Kuhlen, M., Madau, P., & Silk, J. 2009, Science (accepted), arXiv:0907.0005

Kusenko, A. 2009, Physics Reports., in press, arXiv:0906.2968

Laffranchi, M., & Rubbia, A. 2007, Journal of Physics Conference Series, 65, 012014, arXiv:hep-ph/0702080

Lahav, O., Bridle, S. L., Hobson, M. P., Lasenby, A. N., & Sodré, L. 2000, Mon. Not. Roy. Astron. Soc., 315, L45, arXiv:astro-ph/9912105

Landau, L. D., & Lifshitz, E. M. 1987, Fluid Mechanics (Course of Theoretical Physics Volume 6), 2nd edn. (Butterworth-Heinemann)

Lattanzi, M., & Silk, J. 2009, Phys. Rev. D, 79, 083523, arXiv:0812.0360

Lau, E. T., Kravtsov, A. V., & Nagai, D. 2009, Astrophys. J. (submitted), arXiv:0903.4895

Lee, H. S. et al. 2007, Phys. Rev. Lett., 99, 091301, arXiv:0704.0423

Lee, H. S., et al. 2007, Nucl. Instrum. Meth., A571, 644

Lemze, D., Broadhurst, T., Rephaeli, Y., Barkana, R., & Umetsu, K. 2009, Astrophys. J., 701, 1336, arXiv:0810.3129

Lewin, J. D., & Smith, P. F. 1996, Astropart. Phys., 6, 87

Lewis, A. D., Buote, D. A., & Stocke, J. T. 2003, Astrophys. J., 586, 135, arXiv:astro-ph/0209205

Limousin, M. et al. 2008, Astron. & Astrop., 489, 23, arXiv:0802.4292

Loeb, A., & Mao, S. 1994, Astrophys. J. L., 435, L109, arXiv:astro-ph/9406030

Łokas, E. L., & Mamon, G. A. 2003, Mon. Not. Roy. Astron. Soc., 343, 401, arXiv:astro-ph/0302461

Lombardi, S. et al. 2009, arXiv:0907.0738

Lynden-Bell, D. 1967, Mon. Not. Roy. Astron. Soc., 136, 101

Macciò, A. V., Dutton, A. A., & van den Bosch, F. C. 2008, Mon. Not. Roy. Astron. Soc., 391, 1940, arXiv:0805.1926

Maccio', A. V., Kang, X., Fontanot, F., Somerville, R. S., Koposov, S. E., & Monaco, P. 2009, Mon. Not. Roy. Astron. Soc. (submitted), arXiv:0903.4681

Mahdavi, A., Hoekstra, H., Babul, A., Sievers, J., Myers, S. T., & Henry, J. P. 2007, Astrophys. J., 664, 162, arXiv:astro-ph/0703372

Manrique, A., Raig, A., Salvador-Solé, E., Sanchis, T., & Solanes, J. M. 2003, Astrophys. J., 593, 26, arXiv:astro-ph/0304378

Markevitch, M., Gonzalez, A. H., Clowe, D., Vikhlinin, A., Forman, W., Jones, C., Murray, S., & Tucker, W. 2004, Astrophys. J., 606, 819, arXiv:astro-ph/0309303

Merritt, D., Graham, A. W., Moore, B., Diemand, J., & Terzić, B. 2006, Astronom. J., 132, 2685, arXiv:astro-ph/0509417

Merritt, D., Milosavljević, M., Verde, L., & Jimenez, R. 2002, Phys. Rev. Lett., 88, 191301, arXiv:astro-ph/0201376

Miralda-Escude, J., & Babul, A. 1995, Astrophys. J., 449, 18, arXiv:astro-ph/9405063

Miuchi, K. et al. 2007, Physics Letters B, 654, 58, arXiv:0708.2579

Miuchi, K., et al. 2007, arxiv:physics/0701118

Monaghan, J. J. 1992, Annu. Rev. Astron. Astrop., 30, 543

Moore, B., Governato, F., Quinn, T., Stadel, J., & Lake, G. 1998, Astrophys. J., 499, L5+, arXiv:astro-ph/9709051

Morandi, A., & Ettori, S. 2007, Mon. Not. Roy. Astron. Soc., 380, 1521, arXiv:0706.2971

Morandi, A., Ettori, S., & Moscardini, L. 2007, Mon. Not. Roy. Astron. Soc., 379, 518, arXiv:0704.2678

Morgan, B., & Green, A. M. 2005, Phys. Rev., D72, 123501, arXiv:astro-ph/0508134

Morgan, B., Green, A. M., & Spooner, N. J. C. 2005, Phys. Rev., D71, 103507, arXiv:astro-ph/0408047

Morselli, A., Lionetto, A., Cesarini, A., Fucito, F., & Ullio, P. 2002, Nuclear Physics B Proceedings Supplements, 113, 213, arXiv:astro-ph/0211327

Nagai, D. 2006, Astrophys. J., 650, 538, arXiv:astro-ph/0512208

Nagai, D., Vikhlinin, A., & Kravtsov, A. V. 2007, Astrophys. J., 655, 98, arXiv:astro-ph/0609247

Natarajan, P., & Kneib, J.-P. 1996, Mon. Not. Roy. Astron. Soc., 283, 1031, arXiv:astro-ph/9602035

Navarro, J. F., Frenk, C. S., & White, S. D. M. 1996, Astrophys. J., 462, 563+, arXiv:astro-ph/9508025

——. 1997, Astrophys. J., 490, 493, arXiv:astro-ph/9611107

Navarro, J. F. et al. 2004, Mon. Not. Roy. Astron. Soc., 349, 1039, arXiv:astro-ph/0311231

——. 2008, Mon. Not. Roy. Astron. Soc. (submitted), arXiv:0810.1522

Neto, A. F. et al. 2007, Mon. Not. Roy. Astron. Soc., 381, 1450, arXiv:0706.2919

Nolta, M. R. et al. 2009, Astrophys. J. S., 180, 296, arXiv:0803.0593

Novak, G. S., Cox, T. J., Primack, J. R., Jonsson, P., & Dekel, A. 2006, Astrophys. J. L., 646, L9, arXiv:astro-ph/0604121

Padmanabhan, T. 1990, Physics Reports., 188, 285

——. 2008, arXiv:0812.2610

Peccei, R. D., & Quinn, H. R. 1977, Phys. Rev. Lett., 38, 1440

Peebles, P. J. E. 1980, The large-scale structure of the universe (Princeton University Press)

Perlmutter, S. et al. 1999, Astrophys. J., 517, 565, arXiv:astro-ph/9812133

Piffaretti, R., Jetzer, P., Kaastra, J. S., & Tamura, T. 2005, Astron. & Astrop., 433, 101, arXiv:astro-ph/0412233

Piffaretti, R., & Valdarnini, R. 2008, Astron. & Astrop., 491, 71, arXiv:0808.1111

Pointecouteau, E., Arnaud, M., & Pratt, G. W. 2005, Astron. & Astrop., 435, 1, arXiv:astro-ph/0501635

Pratt, G. W., Arnaud, M., & Pointecouteau, E. 2006, Astron. & Astrop., 446, 429, arXiv:astro-ph/0508234

Pratt, G. W., Croston, J. H., Arnaud, M., & Böhringer, H. 2009, Astron. & Astrop., 498, 361, arXiv:0809.3784

Press, W. H., & Schechter, P. 1974, Astrophys. J., 187, 425

Profumo, S. 2008, Phys. Rev. D (submitted), arXiv:0812.4457

Profumo, S., & Jeltema, T. E. 2009, Journal of Cosmology and Astro-Particle Physics, 7, 20, arXiv:0906.0001

Rasia, E., Tormen, G., & Moscardini, L. 2004, Mon. Not. Roy. Astron. Soc., 351, 237, arXiv:astro-ph/0309405

Richard, J., Pei, L., Limousin, M., Jullo, E., & Kneib, J. P. 2009, Astron. & Astrop., 498, 37, arXiv:0901.0427

Riemer-Sørensen, S., & Hansen, S. H. 2009, Astron. & Astrop., 500, L37

Riemer-Sørensen, S., Paraficz, D., Ferreira, D. D. M., Pedersen, K., Limousin, M., & Dahle, H. 2009, Astrophys. J., 693, 1570, arXiv:0811.2793

Riemer-Sorensen, S., Pedersen, K., Hansen, S. H., & Dahle, H. 2007, Phys. Rev. D, 76, 043524, arXiv:astro-ph/0610034

Riess, A. G. et al. 1998, Astronom. J., 116, 1009, arXiv:astro-ph/9805201

Rines, K., Diaferio, A., & Natarajan, P. 2008, Astrophys. J., 679, L1, arXiv:0803.1843

Ryden, B. 2003, Introduction to cosmology (Addison-Wesley)

Ryden, B. S., & Gunn, J. E. 1987, Astrophys. J., 318, 15

Saha, P., & Read, J. I. 2009, Astrophys. J., 690, 154, arXiv:0807.4737

Salucci, P., Lapi, A., Tonini, C., Gentile, G., Yegorova, I., & Klein, U. 2007, Mon. Not. Roy. Astron. Soc., 378, 41, arXiv:astro-ph/0703115

Salucci, P., Walter, F., & Borriello, A. 2003, Astron. & Astrop., 409, 53, arXiv:astro-ph/0206304

Salvador-Solé, E., Manrique, A., González-Casado, G., & Hansen, S. H. 2007, Astrophys. J., 666, 181, arXiv:astro-ph/0701134

Sand, D. J., Treu, T., Ellis, R. S., Smith, G. P., & Kneib, J.-P. 2008, Astrophys. J., 674, 711, arXiv:0710.1069

Sand, D. J., Treu, T., Smith, G. P., & Ellis, R. S. 2004, Astrophys. J., 604, 88, arXiv:astro-ph/0310703

Sanglard, V. et al. 2005, Phys. Rev. D, 71, 122002, arXiv:astro-ph/0503265

Sarazin, C. L. 1986, Reviews of Modern Physics, 58, 1

Savage, C., Freese, K., Gondolo, P., & Spolyar, D. 2009a, arXiv:0901.2713

Savage, C., Gelmini, G., Gondolo, P., & Freese, K. 2009b, Journal of Cosmology and Astro-Particle Physics, 4, 10, arXiv:0808.3607

Schneider, P. 2006, in Saas-Fee Advanced Course 33: Gravitational Lensing: Strong, Weak and Micro, ed. G. Meylan, P. Jetzer, P. North, P. Schneider, C. S. Kochanek, & J. Wambsganss, 1–89

Sciolla, G. 2008, Modern Physics Letters A (submitted), arXiv:0811.2764

Sciolla, G., & Martoff, C. J. 2009, New Journal of Physics (submitted), arXiv:0905.3675

Sérsic, J. L. 1963, Boletin de la Asociacion Argentina de Astronomia La Plata Argentina, 6, 41

Sgrò, C. 2008, talk at GGI Conference on Dark Matter

Sheth, R. K., & Tormen, G. 1999, Mon. Not. Roy. Astron. Soc., 308, 119, arXiv:astro-ph/9901122

Skrutskie, M. F. et al. 2006, Astronom. J., 131, 1163

Smith, P. F., & Lewin, J. D. 1990, Physics Reports., 187, 203

Sommer-Larsen, J., & Limousin, M. 2009, Mon. Not. Roy. Astron. Soc. (submitted), arXiv:0906.0573

Spekkens, K., Giovanelli, R., & Haynes, M. P. 2005, Astronom. J., 129, 2119, arXiv:astro-ph/0502166

Spergel, D. N. 1988, Phys. Rev., D37, 1353

Spergel, D. N. et al. 2007, Astrophys. J. S., 170, 377, arXiv:astro-ph/0603449

Spergel, D. N., & Steinhardt, P. J. 2000, Phys. Rev. Lett., 84, 3760, arXiv:astro-ph/9909386

Spooner, N. 2007, Private communication

Springel, V. 2005, Mon. Not. Roy. Astron. Soc., 364, 1105, arXiv:astro-ph/0505010

Springel, V., & Hernquist, L. 2002, Mon. Not. Roy. Astron. Soc., 333, 649, arXiv:astro-ph/0111016

Springel, V. et al. 2008a, Mon. Not. Roy. Astron. Soc., 391, 1685, arXiv:0809.0898

——. 2008b, Nature, 456, 73, arXiv:0809.0894

——. 2005, Nature, 435, 629, arXiv:astro-ph/0504097

Stadel, J., Potter, D., Moore, B., Diemand, J., Madau, P., Zemp, M., Kuhlen, M., & Quilis, V. 2009, Mon. Not. Roy. Astron. Soc., 398, L21, arXiv:0808.2981

Strigari, L. E., Koushiappas, S. M., Bullock, J. S., Kaplinghat, M., Simon, J. D., Geha, M., & Willman, B. 2008, Astrophys. J., 678, 614, arXiv:0709.1510

Taylor, J. E., & Navarro, J. F. 2001, Astrophys. J., 563, 483, arXiv:astro-ph/0104002

Tegmark, M., et al. 2004, Astrophys. J., 606, 702, arXiv:astro-ph/0310725

Thomas, P. A. et al. 1998, Mon. Not. Roy. Astron. Soc., 296, 1061

Tollerud, E. J., Bullock, J. S., Strigari, L. E., & Willman, B. 2008, Astrophys. J., 688, 277, arXiv:0806.4381

Trotta, R. 2008, Contemporary Physics, 49, 71, arXiv:0803.4089

Trotta, R., de Austri, R. R., & Roszkowski, L. 2007, New Astron. Rev., 51, 316, arXiv:astro-ph/0609126

Trotta, R., Feroz, F., Hobson, M. P., Roszkowski, L., & Ruiz de Austri, R. 2008, JHEP, 12, 024, arXiv:0809.3792

Tsallis, C. 1988, J. Stat. Phys., 52, 479

Tucker-Smith, D., & Weiner, N. 2001, Phys. Rev. D, 64, 043502, arXiv:hep-ph/0101138

Valdarnini, R. 2003, Mon. Not. Roy. Astron. Soc., 339, 1117, arXiv:astro-ph/0210263

——. 2006, New Astronomy, 12, 71, arXiv:astro-ph/0606481

van Albada, T. S., Bahcall, J. N., Begeman, K., & Sancisi, R. 1985, Astrophys. J., 295, 305

van Eymeren, J., Trachternach, C., Koribalski, B. S., & Dettmar, R. . 2009, Astron. & Astrop. (accepted), arXiv:0906.4654

Vergados, J. D. 1999, Phys. Rev. Lett., 83, 3597

Vergados, J. D., Hansen, S. H., & Host, O. 2008, Phys. Rev. D, 77, 023509, arXiv:0711.4895

Vikhlinin, A., Kravtsov, A., Forman, W., Jones, C., Markevitch, M., Murray, S. S., & Van Speybroeck, L. 2006, Astrophys. J., 640, 691, arXiv:astro-ph/0507092

Vogelsberger, M. et al. 2009, Mon. Not. Roy. Astron. Soc., 395, 797, arXiv:0812.0362

Walker, M. G., Mateo, M., Olszewski, E. W., Peñarrubia, J., Wyn Evans, N., & Gilmore, G. 2009, Astrophys. J. (accepted), arXiv:0906.0341

Wang, J., & White, S. D. M. 2009, Mon. Not. Roy. Astron. Soc., 396, 709, arXiv:0809.1322

Wojtak, R., Łokas, E. L., Mamon, G. A., Gottlöber, S., Klypin, A., & Hoffman, Y. 2008a, Mon. Not. Roy. Astron. Soc., 388, 815, arXiv:0802.0429

——. 2008b, Mon. Not. Roy. Astron. Soc., 719, arXiv:0802.0429

Wood, M. et al. 2008, Astrophys. J., 678, 594, arXiv:0801.1708

Zait, A., Hoffman, Y., & Shlosman, I. 2008, Astrophys. J., 682, 835, arXiv:0711.3791

Zappacosta, L., Buote, D. A., Gastaldello, F., Humphrey, P. J., Bullock, J., Brighenti, F., & Mathews, W. 2006, Astrophys. J., 650, 777, arXiv:astro-ph/0602613

Zentner, A. R. 2007, International Journal of Modern Physics D, 16, 763, arXiv:astro-ph/0611454

Zhang, Y.-Y., Finoguenov, A., Böhringer, H., Kneib, J.-P., Smith, G. P., Kneissl, R., Okabe, N., & Dahle, H. 2008, Astron. & Astrop., 482, 451, arXiv:0802.0770

Zhao, H. 1996, Mon. Not. Roy. Astron. Soc., 278, 488, arXiv:astro-ph/9509122

Zwicky, F. 1933, Helvetica Physica Acta, 6, 110